Towards high resolution estimates of East Antarctic pack ice thickness

Adam Daniel Steer
BSc, BAntStud(Hons)

UNIVERSITY *of*
TASMANIA
AUSTRALIA

Submitted in fulfilment of the requirements for the Degree of Doctor of Philosophy

---

School of Land and Food,
May 2016

Declaration of originality

I declare that this thesis contains no material which has been accepted for a degree or diploma by the University or any other institution, except by way of background information and duly acknowledged in the thesis, and to the best of my knowledge and belief no material previously published or written by another person except where due acknowledgement is made in the text of the thesis, nor does the thesis contain any material that infringes copyright.

Adam Daniel Steer

30 October 2016

Authority of access

Supporting publication and statement of authorship

Chapter 2 of this thesis is reproduced from the publication: Steer, A., Heil, P., Watson, C., Lieser, J. L., Massom, R. A. and Ozsoy-Cicek, B. Estimating small-scale snow depth and ice thickness from total freeboard for East Antarctic sea ice. *Deep Sea Research Vol. II*, 2016. http://dx.doi.org/10.1016/j.dsr2.2016.04.025

Statement of authorship

Contributing author	**Roles**	%
Adam Steer[1]:	Data collation, analysis, production of plots, tables and drafting the manuscript	75%
Dr. Petra Heil[3,4]	Source of in situ ice thickness data collections, field data collection and editorial assistance	8%
Dr. Christopher Watson[1]	Scientific guidance and editorial assistance	8%
Dr. Jan L. Lieser[2]	Scientific guidance, editorial assistance and field data collection	5%
Dr. Robert Massom[3,4]	Source of snow depth and density observations and editorial assistance	3%
Dr. Burcu Oszoy-Cicek[5]	Scientific guidance and editorial assistance	3%

Affiliations: 1.University of Tasmania, School of Land and Food; 2. University of Tasmania; 3. Australian Antarctic Division, Department of the Environment, Hobart, Tasmania; 4. Antarctic Climate and Ecosystems Co-operative Research Centre, University of Tasmania, Hobart, Tasmania, Australia; 5. Maritime Faculty, Istanbul Technical University, Istanbul, Turkey.

Dr. Christopher Watson
Supervisor
School of Land and Food
University of Tasmania
4 October 2016

Dr. Jan L. Lieser
Supervisor
University of Tasmania
4 October 2016

Acknowledgements

Thankyou to an incredibly patient family, and a supportive supervisory team.

The support of the Australian Antarctic Division sea ice research group was critical to this project, providing financial support and access to data, software and hardware without which this project would have been impossible. Peter Jansen and Kym Newbery provided invaluable support for testing instruments developing code associated with LiDAR georeferencing used in this thesis.

Raw airborne LiDAR measurements, aircraft trajectories and aerial imagery, along with software to perform preliminary data processing were provided by Dr Jan L. Lieser, Antarctic Climate and Ecosystems CRC. In situ observations of sea ice thickness and ice floe surveying data were released for this study by Dr Petra Heil, Australian Antarctic Division, along with software for processing GPS observations. Ice draft observations by upward looking sonar were provided by Dr Guy Williams, University of Tasmania.

Abstract

The area of the Southern Ocean covered by sea ice is relatively well described by a long-term time series of satellite observations spanning over 35 years. Throughout the seasonal cycle, Antarctic sea-ice cover varies between approximately $3 \times 10^6\,\mathrm{km}^2$ at the end of summer to approximately $20 \times 10^6\,\mathrm{km}^2$ during winter. This has profound implications for ocean-atmosphere heat and momentum exchange and also for global oceanic circulation induced by sea-ice production and melt. However, the thickness distribution of Antarctic sea-ice is poorly described. Without detailed knowledge of the distribution of sea-ice thickness (and hence volume) it is difficult to assess the magnitude of its influence, and its feedback within the ocean-ice-atmosphere system. Current estimates of the sea-ice thickness distribution derived from satellite-based altimetry rely on empirical models describing the relationship between sea-ice topography, snow depth and sea-ice draft. The input to these empirical models include approximations for the density of snow, sea ice and seawater, and relationships between snow depth and the total freeboard (ice + snow) of sea ice derived from sparse in-situ observations. Further, observations from comparatively lower resolution satellite altimetry remain insensitive to small scale features that often characterise sea ice.

This research estimates high-resolution sea-ice thickness from airborne nadir-looking photography and Light Detection and Ranging (LiDAR), deployed over East Antarctic pack ice between 2007 and 2012. It presents a detailed analysis of empirical models for snow depth estimation derived from in-situ observations. For altimetry without coincident methods to remotely sense the snow/ice interface, using an empirical relationship between snow depth and measured elevation is the only available means to estimate snow depth. This represents a novel direct comparison between empirical snow depth models and in situ observations at scales of less than hundreds of metres. Examination of sources of uncertainty in altimetry observations follow, with the development of a method for deriving the uncertainty of each point position in a LiDAR swath. This allows the rigorous propagation of uncertainties from the airborne instruments through to snow depth and ice thickness estimates. A unique comparison of draft estimates from airborne LiDAR with sea-ice draft mapped by upward looking SONAR from an underwater robot forms a key component of this research. SONAR-based ice drafts are used to empirically derive parameters for the ice thickness model applied to airborne LiDAR observations. Using the same small patch of sea ice, relationships between surface and under-ice features are explored, providing a unique insight into how well ice drafts derived from surface topography characterise the under-ice environment. The empirically derived model parameters from this exercise are then applied to a larger-scale dataset, which is compared to near-coincident ship-based visual sea-ice observations (using the ASPeCt protocol).

Using in situ and sonar observations collected by an Autonomous Underwater Vehicle (AUV) to inform parameter choices for modelling sea ice thickness from LiDAR altimetry, a close match between sub-floe scale ice draft from AUV and LiDAR-derived estimates was obtained. The ice density parameter used in the model was artificially high, at 915.6 $\mathrm{kg\,m^3}$ compared to observed values which ranged from 800 $\mathrm{kg\,m^3}$ to 870 $\mathrm{kg\,m^3}$ on SIPEX-II. The distribution of ice keels associated with surface ridges was broadly similar in both AUV observations and LiDAR-derived estimates, although keels modelled using surface topography are narrower and deeper than keels present in the AUV observations. Small-scale topography was also added at the ice-ocean interface for draft estimates from airborne LiDAR, reflecting the influence of snow dunes at the surface. Importantly, co registration of in situ, AUV and airborne observations shows clearly that in situ observations captured only the thinnest and least deformed region of the surveyed ice floe.

At a broader scale, the knowledge gained from validating sea ice thickness estimates over a single floe was applied to a 120 km flight leg with a near-coincident ASPeCt ship-based ice thickness observations. The distribution of ice thickness estimates from airborne LiDAR exhibited a shallow peak in the 3 m to 4 m range, where ship-based observations were predominantly showing ice thicknesses between 1 m to 2 m. This pattern is also seen for the smaller floe-scale study, suggesting that in situ observations for regions of deformed ice off East Antarctica may only represent one tail of the sea-ice thickness distribution. The implications for the use of in situ observations in tuning algorithms for satellite-based estimates of sea-ice thickness are clear, suggesting a bias toward thin ice especially in regions of heavy deformation.

This work advocates for the combination of multiple observation types and techniques given their ability to offer insight into biases that affect a particular method at a particular spatial scale. Technologies spanning in situ, airborne and satellite platforms have a strong and integrated future in sea-ice observation.

Contents

List of Figures

List of Tables

List of Equations

Chapter 1 Introduction

1.1 Overview

The thickness distribution and total volume of Antarctic pack ice are largely unknown. Approximately 19 million square kilometres of the Southern Ocean around Antarctica freeze over every winter, and at the height of the summer only a few million square kilometres of ice remain, mostly in the Weddell Sea (Zwally et al., 2002; Cavalieri and Parkinson, 2008). The formation of this vast icy cap on the Southern Ocean drives thermohaline overturning circulation (Allison, 1981; Williams et al., 2008) and once thick enough, prevents the loss of heat from the warm ocean to the cold polar atmosphere (Worby and Allison, 1991; Jeffries et al., 2001). As sea ice melts, vast amounts of fresh water are released into the ocean, often far from where the ice formed. This provides a relatively fresh, relatively warm surface layer in which phytoplankton bloom during spring, providing the driving force behind the Antarctic marine ecosystem (e.g. Nicol et al., 2008; Massom and Stammerjohn, 2010).

The area covered by sea ice is described in a 30-year satellite record (Gloersen et al., 1993; Zwally et al., 2002; Cavalieri and Parkinson, 2008). This dataset provides a starting point for inferring the effects of sea ice on the Earth's oceans and climate system. Without estimates of the ice thickness and its variability, however, questions about how much ice is formed and melted each year, how much driving force for thermohaline circulation exists, and how much fresh water is available to provide spring bloom conditions each year cannot be reliably answered. Since ice volume is unknown, there is no way of directly estimating the influence of Antarctic sea-ice formation and melt on the Earth system, or how it responds to anthropogenic or other disturbance.

Spatially and temporally limited field campaigns (e.g. Adolphs, 1998; Massom et al., 2006; Xie et al., 2011; Worby et al., 2011) provide the only means of directly measuring sea-ice thickness in the vast pack ice region. A broader picture is given by the Antarctic Sea ice Processes and Climate (ASPeCt) ship-based observation program, which has been used to produce a circumpolar sea-ice thickness distribution based on integrated observations from some 20 years of voyages (Worby et al., 2008b). Given the ship-dependent nature of the sampling regime, ASPeCt observations are biased by a preference for navigable ice - and still represent only a tiny fraction of the Antarctic ice pack. Recent observations of ice draft by Autonomous Underwater Vehicle (AUV) suggest that the in situ record for Antarctic sea-ice is biased toward thinner ice (Williams et al., 2014b). Larger-scale

ice draft observations from submarines, used to investigate the state of Arctic sea ice, are effectively prevented by the Antarctic Treaty System (Meade et al., 2001).

Satellite altimetry offers a promising method for routine circumpolar estimation of Antarctic sea-ice volume. Using empirical estimates of snow density, ice and water density and the assumption of hydrostatic equilibrium, sea-ice thickness can be inferred from surface elevation measurements (e.g. Laxon et al., 2003; Forsberg and Skourup, 2005; Kwok et al., 2007; Zwally et al., 2008; Giles et al., 2008; Connor et al., 2009; Kwok, 2010; Yi et al., 2011; Laxon et al., 2013; Wang et al., 2013). In the Arctic, the European Space Administration (ESA) CRYOSAT-2 Radio Detection And Ranging (RADAR) altimeter has recently been used to infer the thickness of sea ice across the Arctic basin for the first time (Laxon et al., 2013).

This approach comes with some significant challenges. Sea-ice is a highly heterogeneous material. Its spatial distribution, thickness, material composition, dielectric properties, snow cover, and topography vary on scales from centimetres to hundreds of metres. This presents a problem for satellite altimeters with a minimum resolution of several tens to hundreds of metres. How is the highly variable sea-ice topography integrated into an altimeter measurement? And what are the dominant sources of bias in an integrated measurement? And finally, how can field measurements be scaled up to adequately represent satellite-based measurements?

Airborne remote sensing systems offer a potential link - measurements from scanning Light Detection and Ranging (LiDAR) instruments can be collected over wide areas at spatial resolutions which overlap direct sampling. Airborne remote sensing platforms are widely recognised as satellite validation tools (e.g. Dalå et al., 2005; Forsberg and Skourup, 2005; Hvidegaard and Forsberg, 2002; Kurtz et al., 2012; Wang et al., 2013). In 2007 the Australian Antarctic Division (AAD) first deployed the Aerial Photography, Pyrometer and Laser Scanner (APPLS) system, a helicopter-borne remote sensing platform aimed at answering these questions. The motivation for this thesis is provided by a need to validate the airborne system over sea ice and provide rigorous calibration parameters. The APPLS system is one of few high-resolution airborne remote sensing platforms operated over Antarctic pack ice, and the only platform focusing on East Antarctic pack ice. Therefore, optimising results from the APPLS system is a key contribution to the sparse body of knowledge on Antarctic sea ice.

1.1.1 Sea ice in the climate system

Antarctic sea ice begins expand at the onset of autumn and as winter proceeds, a vast region of ocean becomes insulated from the cold polar atmosphere by a layer of ice. The formation processes and the presence of ice on the polar oceans influence oceanic circulation and the exchange of heat, gases and momentum between the ocean and atmosphere. Figure 1.1 outlines basic interactions between sea ice, the ocean and atmosphere.

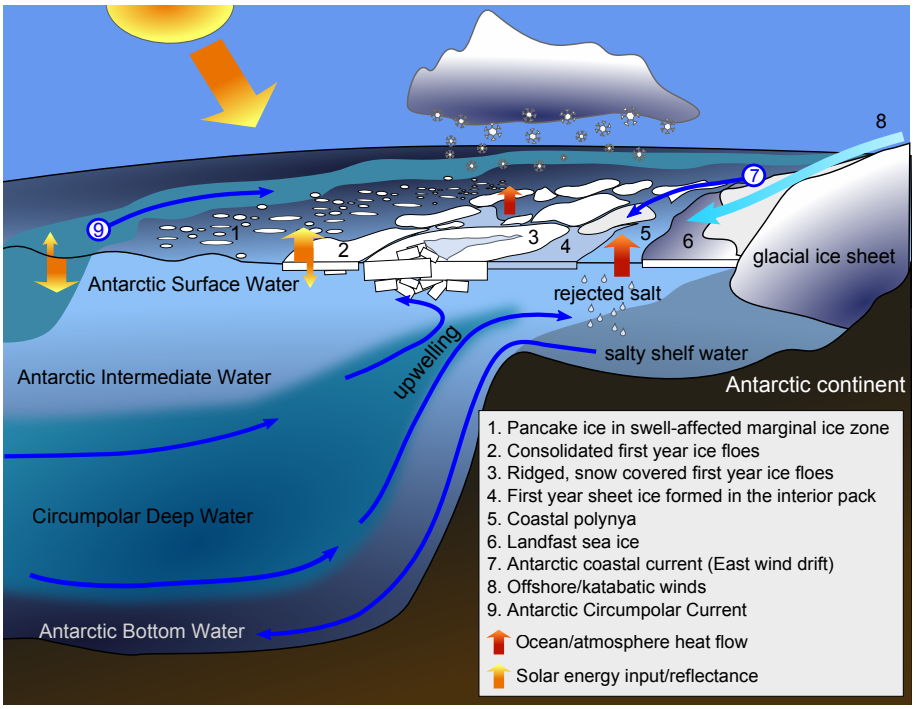

Figure 1.1: Sea-ice components in the climate system

In winter, wherever open water is exposed to the atmosphere, new sea ice is able to form. Near the Antarctic continent, pack ice drifts westward following the 'east wind drift', and where oceanic gyres exist, sea ice is advected to the north and begins a drift eastward with the Antarctic Circumpolar Current (Heil and Allison, 1999). In the lee of iceberg tongues or peninsulas along the coast some regions are kept ice free almost year-round (Massom et al., 1998). These 'polynyas' are sea-ice factories, where new ice is constantly formed and pushed away by persistent winds (Tamura and Ohshima, 2008). As sea water freezes, brine is expelled out of forming sea-ice crystal structure producing cold, dense water just below the ice surface. In the 'ice factories', the cold, salty water generated by ice formation sinks to the ocean floor, eventually driving the overturning circulation of the world's oceans (Allison, 1981; Haine et al., 1998; Goosse and Fichefet, 1999; Tamura and Ohshima, 2008; Ohshima et al., 2013). The sinking water also delivers oxygen to the sea floor, and eventually distributes nutrients from the ocean depths to the surface in upwelling regions across the globe.

Figure 1.2 provides an illustration of sea ice in different developmental stages. As heat is transferred from the ocean to the intensely cold polar atmosphere, small ice crystals (frazil) begin to form in the well-mixed surface layers and as they grow, they begin to float to the surface. In calm conditions they form a layer of unconsolidated 'grease ice', which freezes to form a solid, thin sheet of 'nilas' (Figure 1.2a). If these conditions prevail (for example in sheltered bays) ice thickens by crystal growth up to a thermodynamic limit of 1-2m (Heil et al., 1996). This scenario is typical of landfast sea ice, attached to the coast of the Antarctic continent and islands and forming vast, relatively stable platforms extending out to sea.

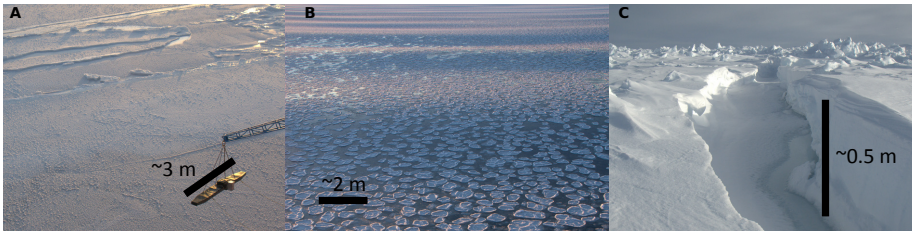

Figure 1.2: Sea-ice formed in different sea states. A: thin nilas ice and 'finger rafting', occuring in calm waters deep in the sea ice pack; B: a pancake ice field, where frazil ice is herded into pancakes by swell; and C: heavily ridged, snow-loaded thick ice with a refrozen and snow-filled crack. This type of ice commonly has a complex composite structure of snow, ice and interstitial seawater

Where winds and currents keep the ice in constant motion the primary mechanisms for increasing ice thickness are the dynamic processes of rafting and ridging (Worby et al., 2008b). Rafting and ridging occur in convergent conditions, where winds and currents act to compress the ice pack. Rafting describes the process of nilas sheets or thinner floes sliding over one another, creating thicker ice with complex layering. Ridging occurs when floes that are too thick to raft over one another are pushed together. Their edges shatter and generate piles of rubble and tilted slabs both above and below the ice surface. In a divergent state, the ice pack relaxes and cracks open within, and between floes (Steer et al., 2008; Hutchings et al., 2012). When open water is formed by these processes in winter, it is quickly frozen over - adding to the total volume of ice on the sea surface (Figure 1.2c).

In swell-affected seas, newly-formed sea ice is herded into small clumps or 'pancakes' which grow by accretion of frazil ice to the edges (Figure 1.2b). These can be consolidated by the same dynamic processes (rafting and ridging) forming larger, thicker ice floes. Given the right conditions dynamically formed ridges re-freeze, fill with snow, and consolidate. Such ridges generally contain the thickest sea ice, and the most interesting problems for sea-ice thickness estimation given their complex composite nature (Kovacs et al., 1973; Lepparanta et al., 1995; Lytle et al., 1998).

The presence of sea ice not only alters the radiometric and oceanographic properties of the sea surface, but also interferes with energy transfer. Sea-ice dampens ocean swell to the point that near the continent, only tidal motion of the sea surface is present. The attenuation of wave energy is dependent on the size and thickness of ice floes, along with the overall area covered by ice (Squire et al., 1995; Bennetts et al., 2010). A smooth ice cover effectively prevents the generation of swell by wind - and wind-driven mixing of upper ocean layers. Heavily ridged and deeply-keeled ice floes, however, alter the kinetic connection between wind and ocean currents (e.g. Steiner et al., 1999).

Sea-ice plays a key role in shaping Southern Ocean ecosystems. Ice-dependent biological communities and linkages between Southern Ocean ice cover are well described (Atkinson et al., 2004; Smetacek and Nicol, 2005; Massom and Stammerjohn, 2010). Along with the

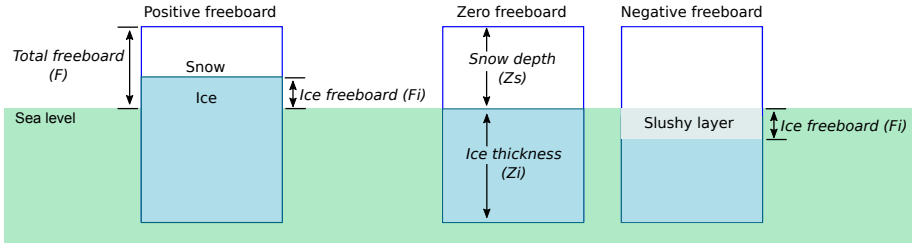

Figure 1.3: Sea ice surfaces and measurements relevant to altimetry.

area covered by sea ice, the thickness distribution is a critical element in determining how the souther ocean ecosystem functions. The availability of light is a key control on in- and under-ice biota, with the productivity of communities essentially controlled by the ice thickness distribution (Meiners et al., 2012). This links the sea-ice thickness distribution to the Southern Ocean ecosystem, since the productivity of sea-ice biota effectively controls how much food is available when the ice melts each spring.

Pack ice on the Southern Ocean is linked to global climate and ecosystems as both a driver and a feedback mechanism. Variability in the total volume and thickness distribution impacts on energy and freshwater fluxes, ocean currents and a vast ecosystem. At present, the questions: 'How much driving force does Antarctic sea ice exert on the climate system?', 'How is Antarctic sea ice responding to climate forcing?' and 'How are Southern Ocean ecosystems going to cope in the future?' cannot be reliably answered - because there is no baseline measurement of the Antarctic sea-ice thickness distribution.

1.1.2 Estimating Antarctic sea ice thickness using altimetry

Given the vast region of the ocean covered with sea ice, estimating a circumpolar sea-ice thickness distribution is only practically possible using satellite-based instruments. At the time of writing, no spaceborne instrument package capable of directly estimating sea-ice thickness exists. The best compromise is the use of satellite-based altimeters, which estimate the range between the satellite and uppermost surface of the sea ice based on the observation of travel time of an electromagnetic waveform. This range allows the determination of the height of the sea-ice surface relative to a reference ellipsoid. Correction for ocean tides and the removal of a mean sea surface (or otherwise a geoid and mean dynamic ocean topography) then yields an estimate of the sea-ice total freeboard - or the height of the uppermost surface of the sea-ice above sea level. 'Sea level', for satellite altimetry, is a reference surface defined from the satellite's reference ellipsoid, using a relevant geoid model, ocean tides and dynamic ocean topography. Figure 1.3 gives an overview of sea ice terminology required for estimation of sea ice properties using altimetry.

Using empirical knowledge of sea ice physical parameters, and principles of buoyancy, the following relationship was derived for the estimation of sea-ice thickness from observations of total freeboard (Wadhams et al., 1992):

$$Z_i = \frac{\rho_w}{\rho_w - \rho_i} F - \frac{\rho_w - \rho_s}{\rho_w - \rho_i} Z_s \tag{1.1}$$

Where Z_i is the ice thickness, ρ_w, ρ_i, and ρ_s are the densities of water, sea ice and snow respectively, F is total freeboard, or elevation above sea surface of the sea ice plus any snow cover above the ocean surface (reference level), and Z_s is the snow thickness, as illustrated in Figure 1.3.

Another approach is to derive a relationship directly from total freeboard to ice draft, using the ratio of total freeboard to draft (referred to as R) (e.g. Alexandrov et al., 2010; Doble et al., 2011; Geiger et al., 2015; Ozsoy-Cicek et al., 2013). While this removes a requirement to estimate snow depth, it treats sea ice as a homogeneous material and relies heavily on adequate characterisation of sea ice types from in situ observations which are used to derive R. In the absence of in situ characterisation, Equation 1.1 is the basis the majority of estimates of sea-ice thickness derived from altimetry. For laser altimeters terms for snow depth must be included, since the snow surface is detected. For RADAR altimetry, only the first term on the right of Equation 1.1 is needed since the ice freeboard (without snow) is presumed to be detected. In this thesis, dealing with airborne LiDAR, 'altimetry' generally refers to laser altimetry unless otherwise specified.

For satellite-based altimetry, the RADAR altimeter aboard ESA's European Remote Sensing satellite (ERS-2) was employed to estimate sea-ice thickness in the Arctic basin (Laxon et al., 2003), followed by a study of ice thickness in the western Weddell Sea (Giles et al., 2008). For both studies, agreement between in situ and satellite-derived ice thickness and was good, but hampered by uncertainty about whether the elevations returned by the altimeter represented total freeboard (snow and ice), ice freeboard only, or some surface within the snow.

Almost concurrently the National Aeronautic and Space Administration (NASA) Ice, Climate and surface Elevation Satellite (ICESat) satellite's Geoscience Laser Altimeter System (GLAS) instrument was used to investigate ice thickness in the Arctic basin (Forsberg and Skourup, 2005) and in the Western Weddell Sea (Kwok and Cunningham, 2008; Wang et al., 2013). ICESat uses a laser altimeter, with a measurement - or laser shot - every 140 m along track. Each laser shot integrates a circle of 65 m to 70 m diameter at sea level into a single elevation measurement. Small sections of East Antarctic pack ice were been investigated using ICESat data in conjunction with field programs (Worby et al., 2011; Lieser et al., 2013), but these efforts have been limited by difficulty in obtaining coincident airborne, ground and satellite measurements.

Since ICESat was decommissioned in 2010 the NASA Icebridge airborne remote sensing program has continued its role, surveying sea ice in the Arctic basin and off the Antarctic Peninsula using airborne LiDAR and imagery (Kurtz et al., 2013; Wang et al., 2013). ESA's next generation RADAR altimetry satellite, CryoSat-2 was launched in 2010, and

has provided the first basin-wide sea ice thickness maps of the Arctic (Laxon et al., 2013). A key improvement for CryoSat-2 is the implementation of a synthetic aperture radar (SAR) mode, allowing CryoSat-2 to resolve features as small as 250 m along-track, allowing multiple observations along single, large ice floes and detecting larger individual leads (Drinkwater et al., 2004).

The Cyrosat-2 and IceBridge programs have, to date, largely ignored East Antarctica. The Antarctic equivalent of the ESA's operational sea-ice thickness service for the Arctic (http://www.cpom.ucl.ac.uk/csopr/index.html, accessed 10 May 2016) is yet to be produced. The regionally heterogeneous nature of sea ice around Antarctica (Worby et al., 2008b) may hinder the development of a circumpolar map of ice thickness.

In a broad sense there is good agreement between in situ and modelled sea ice thickness, but careful attention to model inputs is required. Key parameters in the model must be estimated or modelled from in situ observations - snow depth, snow density, ice freeboard, ice density, and seawater density. The impact of parameter and error estimation on sea ice thickness modelling in the Arctic basin has been briefly examined (Kern et al., 2015; Kwok and Cunningham, 2008), and followed by a recent examination of how different ice regimes affect ice thickness estimates (Alexandrov et al., 2010). In East Antarctica, Worby et al. (2011) provide estimates of in situ water and snow density but defers to the review of Timco and Frederking (1996) for an estimate of sea-ice density. All studies make the point that in situ observations are too sparse to reliably characterise an Antarctic- (or Arctic) wide set of values for use in the modelling of sea ice thickness from altimetry.

1.1.3 Estimating snow depth on Antarctic sea ice

Snow depth is a most difficult quantity to estimate over Antarctic sea ice. Field campaigns give a highly accurate but spatially and temporally disparate dataset (e.g. Massom et al., 2006; Worby et al., 2011; Xie et al., 2011). On a regional scale, microwave brightness temperatures detected by the spaceborne Advanced Microwave Scanning Radiometer (AMSR-E) instrument have been used to estimate snow thickness (Comiso et al., 2003; Markus et al., 2011). While AMSR-E snow thickness agrees generally with ship-based observations (Worby et al., 2008a), the low spatial resolution and complications around ridged ice degrade the utility of the dataset for developing ice thickness estimates from surface elevation measurements.

Using radar-derived snow depth is another approach to including a spatially-variable snow depth distribution in altimetry-derived estimates of sea-ice thickness (e.g. Kwok and Maksym, 2014), but the radar-derived snow depths are essentially one dimension. For a swath-based altimeter which observes sea ice in two dimensions, this method ignores the variability in snow depth outside of the radar footprint. Another simpler method is to apply the mean snow depth from in situ observations in a given region to all altimetry observations (e.g. Doble et al., 2011).

Analysis of in situ snow depth and total freeboard observations in the Bellingshausen sea suggested that Antarctic sea ice has an effective ice freeboard equal to sea level, implying that elevations determined by altimetry were due to snow thickness alone (Xie et al., 2011). In this case, the authors deduced that snow depth could be predicted by the total freeboard. This idea was also explored for East Antarctic sea ice (Worby et al., 2011), who found a strongly bimodal relationship between total freeboard and snow depth. A single 'one size fits all' regression model was relatively weak ($r^2 = 0.6$), but stronger models ($r^2 > 0.9$) were found for ice freeboard >0.12 m and ice freeboard <0.12 m. To address these issues, a set of regionally-based linear regression models for snow depth were derived by Ozsoy-Cicek et al. (2013). While these models match in situ observaions well on ocean basin scales, there is no attempt to investigate smaller-scale effects of snow modelling - leaving an important gap in efforts to understand Antarctic sea-ice thickness distributions at sub-basin scales.

1.1.4 Creating a reference surface for 'elevation' measurements

To measure total freeboard accurately another key problem for altimetry over sea ice must be solved - the determination of the sea surface from which sea-ice freeboard is measured. One approach is to use models which approximate the sea surface topography (e.g. a geoid model, models of dynamic ocean topography and tides). Hvidegaard and Forsberg (2002) used this method, but with a gravimeter flown aboard the same aircraft as a LiDAR instrument. Kurtz et al. (2012) employ geoid and tide models to determine the sea surface for developing a circumpolar map of sea-ice thickness. These must be validated using leads to act as reference points (e.g. Kwok et al., 2007), and may bias sea-ice freeboard estimates by an amount close to claimed vertical resolutions of satellite-based instruments (Ricker et al., 2016).

Another approach is to identify leads in the ice pack, and use points identified as 'open water' to model an instantaneous sea surface. For radar altimeters analysis of return echoes can determine which reflections belong to open water, and which belong to snow and ice (Laxon et al., 2003; Giles et al., 2008). Using the GLAS instrument, sea level is found by filtering the lowest points in the data, meaning 'furthest from the satellite'. The entire dataset is leveled using these 'sea level' tie points, and freeboard determined using the new reference surface (Kwok and Cunningham, 2008; Zwally et al., 2008). A similar method is used for airborne altimetry. Initial approaches to sea surface determination picked the lowest points in chunks of LiDAR and interpolated a sea surface by fitting a polynomial curve to the identified 'low points'. This polynomial function was used to level the elevation dataset to a relative sea surface (Hvidegaard and Forsberg, 2002; Forsberg et al., 2002). The NASA Icebridge program extended the method by first identifying LiDAR points over open water or very thin ice in leads using coregistered aerial imagery. Using a kriging method, a 'sea surface' is interpolated for the LiDAR swath based on the set of points found in leads (Kurtz et al., 2012; Wang et al., 2013). The advantage of localised tie points and a relative sea surface as a reference point is that uncertainties associated with mean sea surface (geoid + dynamic topography) and tide models are removed.

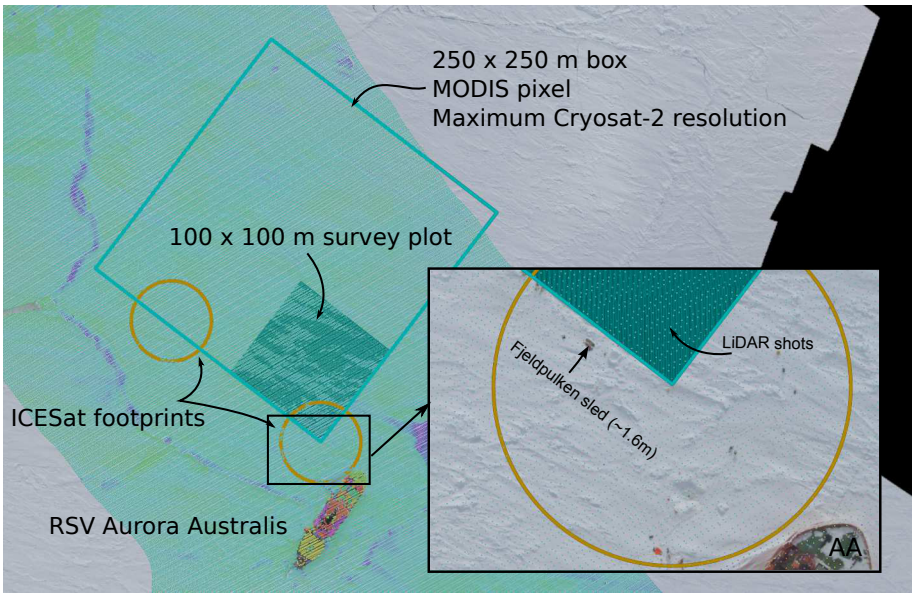

Figure 1.4: Scales at which sea ice characteristics are determined by direct measurement (along one side of the 100 x 100m block), satellite-based altimeters (Cryosat-2 and ICESat), and airborne instruments (blue/green airborne LiDAR strip, georeferenced image in the background). The inset clearly depicts the resolution of the airborne LiDAR, and the small-scale variability in sea-ice topography

1.1.5 From drill holes to ships to satellites and back - observation scales.

From an observer's point of view it is obvious that sea ice topography varies on scales from sub-metre to many hundreds of metres. Figure 1.4 provides an overview of a typical sea ice field site, and gives some indications of feature scales. The figure also depicts the spatial scales at which LiDAR points are collected, at which satellite altimetry operates, and at which the ASPeCt observation program operates.

Drill hole measurements are the current preferred technique for observing metre-scale variability in sea-ice thickness. However, each drill hole may not be perpendicular to the ice surface; the measuring device may not penetrate the entire ice pack; and each observer may choose to record measurements with a different precision. Sailing an icebreaker to the Antarctic pack ice and setting up field observation sites (generally referred to as 'ice stations') is logistically intensive and expensive. Longer holes may take hours to drill depending on equipment, ice conditions and the available human power. For these reasons, the drill hole record in Antarctic pack ice is relatively small.

Ship-based ASPeCt observations are intended to estimate the ice thickness in an area roughly a kilometre in diameter around the observation point, with up to three ice thickness categories in each observation. Ice and snow thickness is estimated by comparing ice the vessel is passing through with an object of known size, hung over the side of the ship (see Worby et al., 2008b). While these observations are relatively imprecise and spatially coarse, the ASPeCt observation protocol provides a useful 'snapshot' over the region the

ship is passing through. Unfortunately, the use of ships for ice observation tends to produce ice thickness data for regions navigable by ships, and neglecting regions of difficult ice or regions of little logistical importance to Antarctic operators.

A satellite altimeter's elevation measurement is essentially the integral of sea ice features contained within the altimeter's footprint - which may contain leads, ridges, and level ice in quantities that may not be reliably determined from the satellite data. The ICESat laser integrates an area 70 m in diameter over sea ice (Kwok and Cunningham, 2008; Zwally et al., 2008), and the recently-launched Cryosat-II SIRAL radar integrates some 250m-per-pixel along-track at its highest resolution (Laxon et al., 2013; Kwok, 2010).

Using a modelling study, Weissling et al. (2011) showed that large-scale variability in modelled sea-ice topography is adequately captured by satellite altimetry. However, field measurements show that sea-ice thickness can be highly variable on a spatial scale in the order of metres to tens of metres - an order of magnitude smaller than the highest resolution satellite altimeters are able to capture. Reducing uncertainty in sea-ice volume estimates requires an ability to zoom in on the metre-scale variability. This is the domain of airborne remote sensing - offering spatial resolution that is comparable to field drill-hole measurements, with coverage similar to the scales of satellite altimetry (Massom et al., 2006; Worby et al., 2011).

Advances in compute power and mathematical modelling make the prospect of floe-scale modelling of Antarctic pack ice a realistic outcome. Using Discrete Element Models, which have their roots in graph theory, it is possible to model interactions between individual floes in an ice pack (Herman, 2013, 2015). For sea ice this is an emerging field, which requires an ability to describe ice properties and the thickness distribution at the scale of tens to hundreds of metres. This level of detail in observation is only achievable with airborne sensors.

However, the East Antarctic is not represented in any airborne remote sensing programs to date. To address this data gap the Australian Antarctic Division (AAD) sea ice research group developed the Aerial Photography, Pyrometer and Laser Scanner (APPLS) instrument package, a helicopter-based remote sensing platform aimed at providing an intermediate scale between ground measurements and satellite altimeters. This package offers the best attempt to date at linking small- and large scale sea ice thickness observations in East Antarctica.

1.2 APPLS: Aerial photography, pyrometer, laser scanner

The APPLS platform is driven by the constraints of needing to launch and land on an icebreaker, and operate in Antarctic conditions over drifting pack ice. The instrument details are given in Lieser (2008), and expanded in Chapter 2. The core platform consists of a Riegl LMS-q240i near-infrared 2D scanning laser altimeter; a Hasselblad H3D-II 50

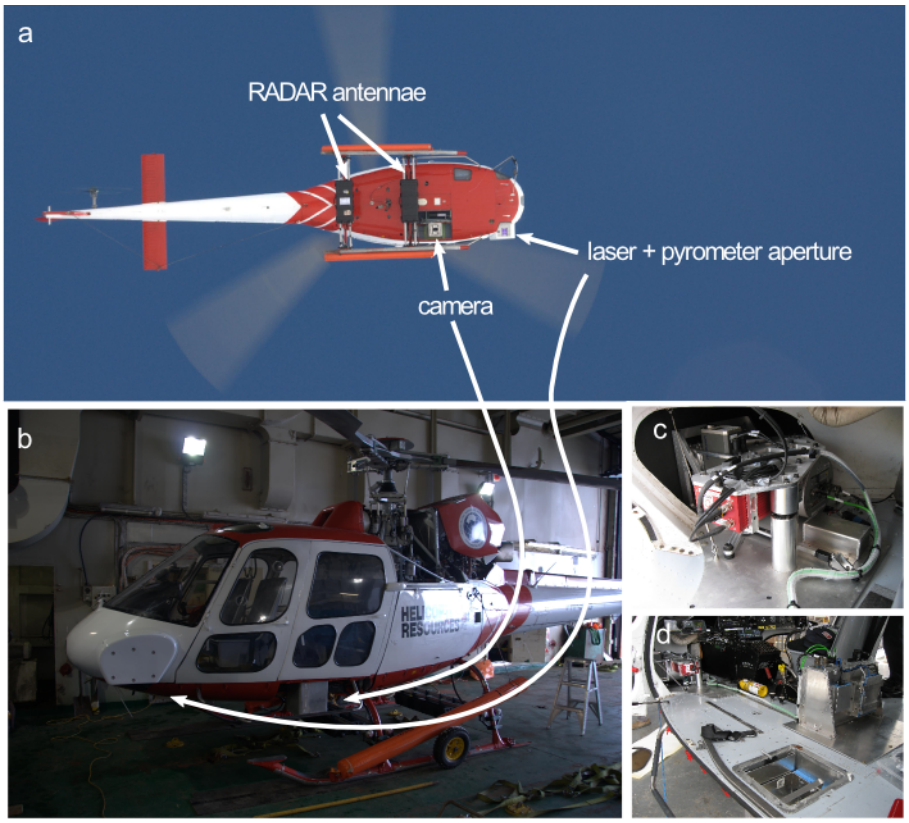

Figure 1.5: *The APPLS-equipped AS-350b squirrel. A: the underbelly of the aircraft showing skid-mounted RADAR antennae, laser scanner and camera. B: side view showing protective cowling over LiDAR and pyrometer, camera bucket and window mounted primary GPS antenna. C: LiDAR (silver cylinder), INS (red) and pyrometer (dark grey, top left) mount inside the helicopter nose. D: Camera bucket (foreground) and controlling electronics rack.*

digital camera; an Heitronics KT-19 infrared pyrometer; and a Java-based logging and timing synchronisation system developed at the AAD to capture navigational and laser scan data, imagery, and pyrometer observations. The main power and control system is flexible enough to allow mounting of additional instruments, for example a broadband snow radar (deployed in 2007 and 2008) or a passive microwave imaging system (deployed in 2012). An Aerospatiale AS-350 'squirrel' was the airborne platform from 2007 to 2012. Figure 1.5 shows the aircraft and instrument configuration.

1.2.1 Airborne LiDAR

LiDAR is a technique which allows measurement of the range from an aircraft to the ground, or some surface below the aircraft using a laser rangefinder mounted in the vehicle. The concept is simple - using a pulsed laser, the primary observable is the time difference between a pulsed transmission and detection of a return echo (time of flight). Multiplied by the speed of light, this gives a range estimate between the laser emitter and the target reflecting surface. For mapping purposes, the laser beam is reflected across the flight path by a rotating mirror. Each range estimate is stored with its scan angle in the laser's

internal coordinate system, forming the basis for a swath of range estimates following the airborne platform's flight path. The basic relationships for scanning LiDAR mapping are described by Baltsavias (1999). In the last ten years the technique has become widespread as a tool for collecting geophysical observations among a multitude of other applications. A recent review of LiDAR as a geodetic imaging tool by Glennie et al. (2013) summarises the uses, potential and pitfalls of airborne LiDAR Mapping.

As a brief summary, collected range measurements are aggregated in a three-dimensional 'point cloud' located in some mapping reference frame. Precise information about instrument orientation is required to account for aircraft attitude (heading, pitch and roll) variation in flight. This is generally achieved by a close coupling between the LiDAR instrument, an Inertial Measurement Unit (IMU) and a Global Positioning System (GPS) receiver. Aircraft orientation is logged by the IMU, and used in post-processing to transform laser points from ranges and angles in an instrument-specific reference frame into the reference frame used by the IMU. The GPS location data are used to transform the point cloud to a terrestrial reference frame (For example ITRF08, Altamimi et al., 2011). IMU data are captured at a very high rate so that dynamic motion and airframe vibration can be fully characterised. GPS data are generally acquired at a lower sampling rate, typically in the 2-10Hz range. The two datasets are typically combined with a Kalman filter (e.g. Kalman, 1960; Mostafa et al., 2001; OXTS, 2008), which uses GPS positions in combination with IMU and GPS velocities, accelerations and orientations to derive an aircraft trajectory. LiDAR geolocation is then performed using the output of the Kalman filter, laser range and scan angle measurements, and parameters describing the orientation of the laser scanner and navigation instruments with respect to each other. Figure 1.6 shows the basic principle of swath mapping with LiDAR.

Each of the instruments used to generate a LiDAR point carries an inherent error that propagates through the system and contributes to an overall point positioning uncertainty. Aircraft positioning is a clear influence, since this uncertainty maps directly into the LiDAR point cloud. As such, development of aircraft positions and interpretation of any biases is critical to a successful surveying campaign (King, 2004; Skaloud, 2007; Shrestha et al., 2007). The determination of relationships between instruments is another significant error component, since small perturbations affect the 3D position of a given point in proportion to its distance from the instrument package. The distances and angles which describe the relationship between instruments in an airborne surveying system are determined by instrument mount engineering and are measured at installation, but these inevitably contain small misalignments (known as 'boresight misalignments') which must be parameterised and corrected in post-processing. For this reason, an Integrated Sensor Orientation (ISO) process is used to account for mounting misalignment and intensity-based range errors. In the APPLS system, the LiDAR instrument is one element in a suite of instruments, all of which work together to produce geophysical estimates from the APPLS platform. The airborne camera, discussed next, and the aircraft positioning system are essential to understanding the data derived from the airborne LiDAR.

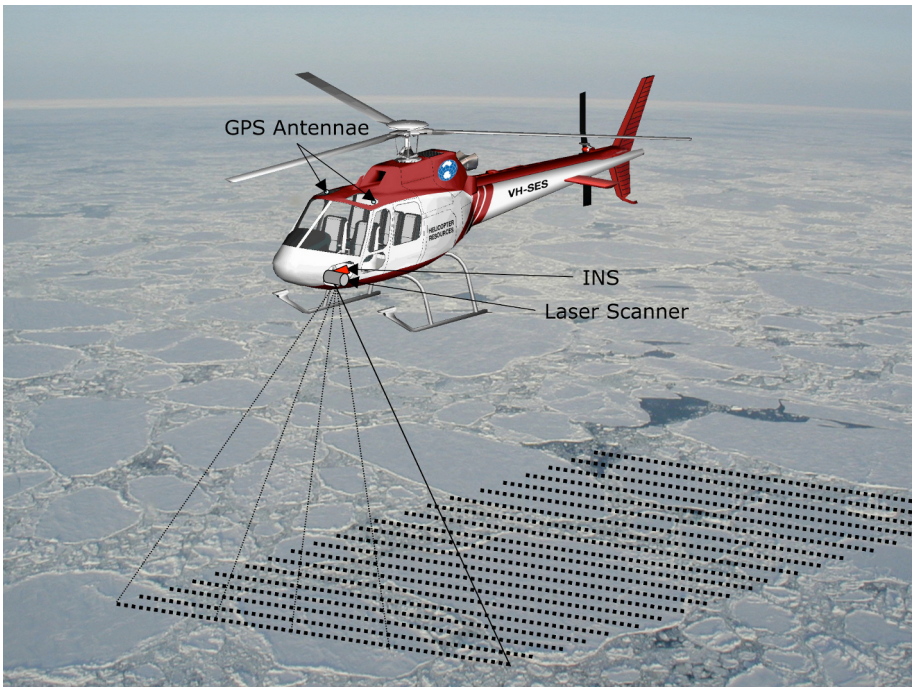

Figure 1.6: *LiDAR principle, figure courtesy of Dr. Jan L. Lieser.*

1.2.2 Digital aerial photography and photogrammetry

The digital camera aboard the APPLS instrument package was included for sampling surface features of sea ice and subsequent analysis for floe size distributions, surface roughness and ice type distributions (Massom et al., 2006; Worby et al., 2008a; Steer et al., 2008; Hutchings et al., 2012). In conjunction with airborne LiDAR, classified aerial imagery can also be used to determine 'sea level' reference points over sea ice (Section 1.1.4, Wang et al. (2013)).

To allow for accurate image mosaic generation, much greater image overlap is required - over 40% along-track and 30% between-track (e.g. Wolf, 1983). With advances in digital image storage technology, the APPLS package was developed to collecting as many images as possible. While survey flights are not designed with a rigorous photogrammetric mission in mind, imagery is collected as quickly as the camera can fire, resulting in imagery often overlapping the preceding two frames. Figure 1.7 shows a typical image overlap from the SIPEX-II campaign.

Where sufficient image overlap exists, the possibility of modelling sea ice using photogrammetric reconstruction techniques, and gaining an independent estimate of camera position is raised. To reproduce an accurate model of the world from photographs, the 'interior orientation' and 'exterior orientation' of the camera system must be well known. The interior orientation describes the camera model - its focal length, frame size, and any lens distortion parameters that must be applied. Exterior orientation described the position and attitude of the camera in a mapping frame - the 3D position, pitch, roll,

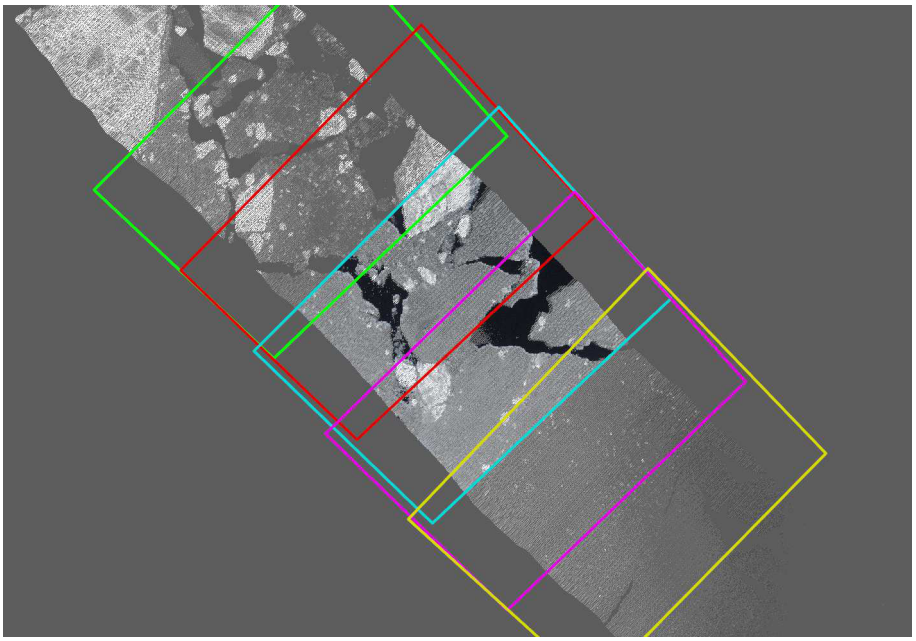

Figure 1.7: *Overlapping image frames collected on SIPEX-II.*

heading, boresight misalignment and any lever arm offset between the camera and the positioning device (e.g. Wolf, 1983; Skaloud, 2002; Mostafa, 2005).

In an approach called 'Structure from Motion' (SfM), features in overlapping images from unstructured image collections are identified, and 3D positions are computed by a bundle adjustment and estimation of the camera interior orientation (Snavely et al., 2006). The idea originated from generating 3D models of city features from unordered image sets (eg internet photo albums), but can apply to any set of overlapping photographs. Offering a potentially low-cost alternative to LiDAR or photogrammetry using large, expensive metric cameras, the method's application to geophysical problems was quickly realised and is becoming an intensely studied topic. Applications for this technique have been found in snowpack and avalanche monitoring (e.g. Cimoli, 2015; Eckerstorfer et al., 2015; Nolan et al., 2015; Vander Jagt et al., 2015), and glacier dynamics (Immerzeel et al., 2014). With evidence that the method works on relatively uniform snow covered surfaces, this presents an opportunity to extend the usage of the APPLS aerial imagery to deriving very high resolution elevation models where conditions permit. Where achievable, the ability to derive elevation models from imagery would complement the slightly coarser airborne LiDAR, and the other functions of airborne photography: identifying regions of open water in the ice pack, and determining the relative contribution of different ice types to the sampled ice pack.

1.2.3 Positioning airborne instruments over Antarctic pack ice

Using well-described surveying strategies and post-processing techniques (e.g. Castleden, 2004; Novatel, 2005; Shrestha et al., 2007) it is possible under the right conditions to

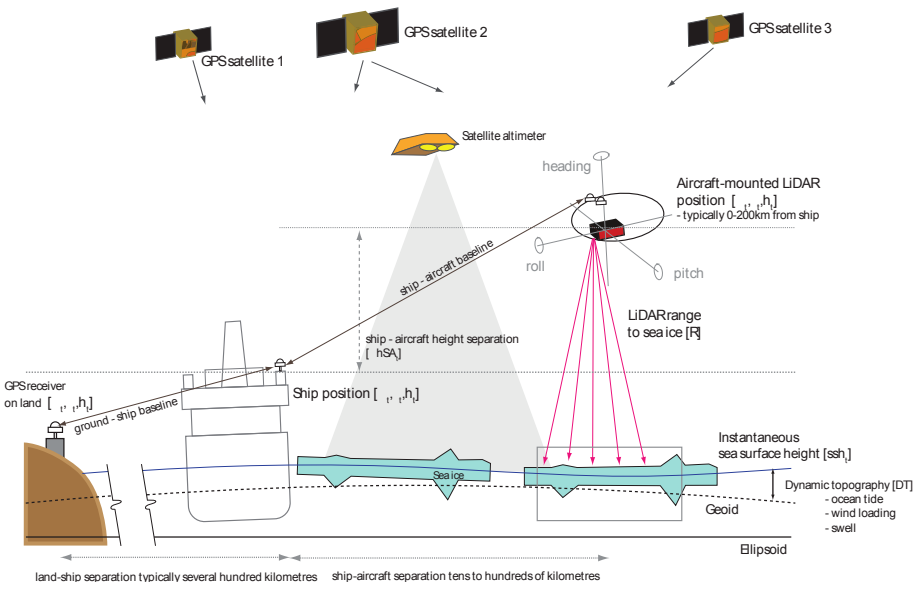

Figure 1.8: *General geometry for an airborne survey over sea ice using APPLS.*

observe sub-centimetre motion of points on or near Earth relative to some reference frame (e.g. ITRF2008, Altamimi et al. (2011)). With this potential accuracy and very lightweight infrastructure, satellite-based positioning is highly attractive for airborne surveying. For airborne remote sensing GPS is used to position a highly dynamic, fast moving platform. In this case positioning accuracies are limited by a need to solve ambiguities at individual epochs, and a relatively quickly changing satellite constellation (e.g. King, 2004).

In the Antarctic pack ice the situation is complicated by a lack of nearby fixed reference points (required for differential carrier phase based processing techniques) and a dynamic surveying target which occupies a dynamic reference surface. Figure 1.8 depicts the basic geometry of an airborne survey over Antarctic pack ice. The 'ground-ship' baseline is typically several hundred kilometres, as is the 'ground-aircraft' baseline. The baseline 'ship-aircraft' is typically tens to hundreds of kilometres. Depending on the location of the survey, dynamic sea surface topography may include tides, synoptic-scale water mass dynamics, and damped ocean swell - which may penetrate hundreds of kilometres through the ice pack (Worby et al., 2011). For receiver separations in the ranges given here, position accuracy using GPS may approach the level of decimetres at best (e.g. Dalå et al., 2005; King, 2009)

Aircraft equipped with geophyscial sensors such as LiDAR are often positioned relative to a land based reference station in order to take advantage of differencing of common mode errors in the GPS measurements (e.g. Mostafa, 2005; Shrestha et al., 2007), since the reference and aircraft receivers are able to track identical satellites under near-identical environmental conditions. A fundamental consideration for relative GPS positioning in airborne surveying is that as the baseline - or distance between the reference point and the aircraft increases, positioning accuracy is degraded as errors (for example ionospheric

delay) experienced at each receiver decorrelates (e.g. Novatel, 2005; Colombo et al., 2010; King, 2009). An additional challenge for aircraft is that atmospheric conditions between the aircraft and a given reference GPS station may differ markedly due to altitude separation (King, 2004).

Over baseline lengths of up to 1000 km, decimetre level positioning of dynamic platforms has been achieved for ocean buoys (Colombo et al., 1981) and long-range airborne surveys (Forsberg and Skourup, 2005; Kurtz et al., 2012). Forsberg and Skourup (2005) compared GPS-positioned LiDAR and ICESat sea ice elevations and obtained decimeter-level aircraft positioning over baselines of several hundred kilometres, concluding that an improvement in accuracy for relative positioning over similar baselines may be optimistic at best. This is supported by a detailed study of the GPS error budget using an 'aircraft-like' scenario, which determined that the 'noise floor' for long-baseline kinematic positioning is in the order of decimetres, and increasing with baseline length (King, 2009).

Kinematic Precise Point Positioning (kPPP) is a positioning method which requires no reference receiver. The location of a single, dual-frequency carrier-phase receiver is estimated using precise knowledge of satellite orbits (Kouba and Héroux, 2000). Considering a long baseline kinematic processing environment, kPPP offers similar accuracies to relative positioning (Gao and Chen, 2004; Geng et al., 2010; King, 2009). However, fewer data per epoch are available for resolution of biases, potentially making the method more sensitive to GPS signal perturbations (Castleden et al., 2004).

A final option for airborne surveying over sea ice is relative moving-baseline positioning (e.g. Lachapelle et al., 1994). In this method both the reference and roving receivers are mobile. On sea ice, a reference receiver is stationed on moving pack ice or onboard a ship which is used as abase for airborne survey operations. This technique is most commonly used for ship to ship or aircraft to aircraft positioning, where the relative position vector between each vehicle is more important than the absolute position of each (e.g. Doutt et al., 1998)

The choice of airborne platform also plays a role in determining the potential accuracy of positioning. A helicopter offers few options for mounting GPS antennae outside of the rotor disc, which may interfere with GPS signals (Brodin et al., 2005). Depending on the configuration of GPS antennae and the surveying environment, loss-of-lock events may occur as the aircraft manoeuvres (Hardesty et al., 2004). In the event of satellite signal loss, there are few data-per-epoch which can be used to solve bias parameters and resolve ambiguities, leading to degraded accuracy and potentially spurious jumps in the final trajectory.

1.2.4 Using inertial observations to aid positioning

Alongside a 3D position in geographic space, knowledge of aircraft attitude is also required for production of LiDAR point clouds, georeferenced imagery and pyrometer

measurements. For the APPLS platform a strapdown inertial+GPS navigation system is used, a common option for aerial surveyors (e.g. Hvidegaard and Forsberg, 2002; Mostafa, 2005; Skaloud, 2007). These employ a set of accelerometers and gyroscopes - or IMU - to determine angular accelerations in flight. These are integrated to form epoch-to-epoch displacements along with heading, pitch and roll angles. Since IMU based position measurements are subject to time-dependent drift (e.g. Burman, 2000), a Kalman filter (Kalman, 1960) is generally used to combine IMU with GPS data to produce a final trajectory (OXTS, 2008; Stebler, 2008; Yi, 2007). Depending on the filter attributes, there is potential to fix short GPS outages or spurious events - a highly attractive feature of integrated GPS +IMU trajectory determination for helicopter-based operation.

The navigation system ties the LiDAR, camera and pyrometer to a real-world reference system, and to each other. Importantly, GPS provides time synchronisation for data collected by each instrument. Using integrated sensor orientation (ISO) principles, the data collected by each instrument plays an important role in refining the end products from the APPLS system. This thesis aims to use the instruments and methods here to optimise the estimation of sea ice thickness in east Antarctica from the APPLS package, attempting to fill a critical data gap.

1.3 Thesis aims and outline

The primary aim of this thesis is to develop a robust, high resolution estimate of sea-ice thickness using the APPLS airborne remote sensing platform. A final sea ice product from the APPLS system relies on detailed knowledge of the error budget, and effective combination of the multisensor data collected. This thesis aims to achieve the following objectives:

- Provide an understanding of sea ice physical processes in the Earth system and the need for in situ and high resolution remotely sensed observations (Chapter 1)
- Understand processes for snow depth and sea-ice thickness estimation from altimetry, and effects of scale on analytical outcomes (Chapter 2)
- Understand the uncertainties associated with the airborne APPLS system (Chapter 3)
- Convert raw observed data into meaningful, validated geophysical parameters; and interpret these novel data appropriately (Chapter 4)

The introductory chapter has detailed the importance of Antarctic sea ice in the Earth system, in particular the overall volume of ice made and melted each year. It has laid out the logistical and technical issues in the determination of a robust ice thickness distribution, highlighted the dependency of satellite observations on detailed in situ

measurements, and pointed out that satellite estimates of ice volume must be carefully validated to assess the effects of smaller-scale features on an elevation estimates. The chapter also sets out the surveying challenges for airborne instrument packages over sea ice: remoteness, lack of control points, and uncertain reference surfaces for elevation measurements. Finally, the APPLS airborne remote sensing package is introduced, with a brief review of the development of airborne LiDAR and imaging technologies and how they apply to the APPLS system.

Chapter 2 examines the fundamental mathematical model for estimating sea ice thickness from altimetry and shows it's sensitivity to, in particular, 'total freeboard' and snow depth estimation. Snow depth models for East Antarctic sea ice are derived from three research voyages: ARISE (2003), SIPEX (2007), and SIPEX-II (2012). Snow depth from these models is compared to in situ snow depth measurements, and to other snow depth models published for East Antarctica. It shows how well empirical models derived from *in situ* observations perform for estimating snow at length scales smaller than a few hundred metres. It also shows how the choice of snow model, and the choice of input parameters to the ice thickness model impact the thickness derived using this method. The chapter concludes with a realistic description of uncertainties in ice thickness estimates from altimetry, leading directly into an analysis of uncertainties in the APPLS package.

Chapter 3 details the instruments used in the APPLS package, their specifications and configuration. Drawing on these details the chapter sets out to determine an a priorierror budget based on a rigorous propagation of instrument errors through to LiDAR point clouds. Two additional sources of uncertainty are defined, namely the influence of rotor blade interference with GPS signal transmission; and the effect of airframe vibration on instrument positioning. The effects of airframe vibration are characterised, and strategies for mitigation are explored. Boresight misalignment values for the LiDAR and camera are estimated, and the possibility of 'in field' calibration is also investigated. Data gathered from engineering specifications and the analyses undertaken here are employed to determine an a priorierror budget for the APPLS system, and detail the sensitivities of the system to each of its components. From there, methods for optimising the error budget of the APPLS platform are presented.

Chapter 4 applies methods developed in chapters 2 and 3 to APPLS surveys over Antarctic sea ice, in order to develop and interpret an APPLS-based ice thickness estimate. It also introduces a new method for determining a reference surface using the LiDAR observations as a starting point. Using coincident under-ice sonar collected by Autonomous Underwater Vehicle (AUV), the chapter investigates the choice of model parameters used to derive sea-ice thickness. It also uses this rare opportunity to investigate relationships between surface and under-ice topography derived from independent, co-registered datasets (e.g. Doble et al., 2011). Using the knowledge gained from assessment against AUV and drill hole observations, it extends the concepts from floe-scale to synoptic-scale, using a 100 km flight leg to derive ice thickness from airborne LIDAR. These estimates are compared with ASPeCt protocol ship based sea ice thickness estimates in the region. The chapter

concludes with a discussion on the reliability of sea ice thickness estimates from the APPLS package, and methods for deriving sea ice thickness estimates from the entire APPLS data store.

Chapter 5 concludes the thesis with a discussion of APPLS products with relation to, for example, NASA's Icebridge program and upcoming satellite altimetry missions. Looking at smaller scales, the contribution of floe-scale thickness distribution data to modern, graph based modelling approaches to sea ice are discussed. Finally, the chapter makes recommendations for the processing of already-collected APPLS data, and deployment strategies for future airborne remote sensing missions.

Chapter 2 Estimating small-scale snow depth and ice thickness from total freeboard for East Antarctic sea ice

2.1 Introduction

The Antarctic sea-ice thickness distribution is poorly understood, but has wide-ranging effects on the Southern Ocean. Due to the remoteness and size of the Antarctic pack-ice zone, estimating the circumpolar Antarctic sea-ice thickness distribution is only feasible with satellite-based instruments. Satellite altimetry offers a feasible solution for this task, since the conversion of ice freeboards to thickness is a simple computation based on an assumption of hydrostatic equilibrium between sea ice, it's snow cover and the underlying seawater, and some empirical knowledge of the densities of these three materials (e.g. Alexandrov et al., 2010; Giles et al., 2008; Markus et al., 2011; Wadhams et al., 1992; Yi et al., 2011; Zwally et al., 2008).

For satellite-borne laser altimeters the only data available for estimating thickness are total freeboard estimates - meaning the elevation of ice and snow above local sea level, based on ranging between the altimeter and the sea-ice surface. RADAR altimeters observe the elevation of the sea ice (without snow) above the sea surface where the snowpack is dry and homogeneous, meaning that ice thickness can be estimated without accounting for snow depth. However, interpretation is difficult where icy or wet layers exist in the snowpack (e.g. Laxon et al., 2013; Willatt et al., 2010).

Over Antarctic sea ice, the historical ICESat dataset and the ongoing NASA Operation IceBridge campaign (IceBridge, e.g. Studinger et al., 2010) use laser altimetry to estimate sea-ice parameters (e.g. Kurtz et al., 2012, 2013; Kwok and Maksym, 2014; Xie et al., 2011, 2013). In East Antarctica, high resolution airborne laser altimetry has been flown over a small portion of the pack-ice zone, with the aim of investigating sea-ice parameters on the metre- to tens-of-metres scale (Lieser et al., 2013). These airborne remote sensing data approach the resolution of in situ ice measurements, and offer a potential link from drill holes at the scale of metres to satellite observations at the scale of hundreds or thousands of metres. This is critical for understanding how small-scale variability is contained in larger-scale satellite-based estimates of sea-ice parameters.

A key problem for laser altimeters is the conversion of an elevation - or total freeboard - observation to an ice thickness. A functional model for estimating sea-ice thickness using

only total freeboard and sparse in situ observations is given by assuming that sea ice and its snow cover exist in hydrostatic equilibrium with surface seawater (Equation 1.1). Using the model there is reasonable agreement between in situ observation and sea-ice thickness estimated from altimetry (Xie et al., 2013; Yi et al., 2011; Zwally et al., 2008), but careful attention to the inputs for Equation 1.1 is critical. Key parameters in the model must be estimated from in situ observations - snow density, ice freeboard, ice density, and seawater density, each of which vary on different spatial and temporal scales. In East Antarctica, Worby et al. (2011) provide estimates of in situ water and snow density but defers to the review of Timco and Frederking (1996) for an estimate of sea-ice density. Hutchings et al. (2015) provide a rare glimpse of East Antarctic pack-ice density from in situ observations. All studies make the point that in situ data are too sparse to reliably characterise an Antarctic- or Arctic wide set of values for use in the estimation of sea-ice thickness from satellite and airborne altimetry.

For application to altimetry observations and Eq. 1.1, snow depth can be estimated from in situ observations or remote sensing methods. Field campaigns aimed at collecting in situ observations of snow depth give a highly accurate but spatially and temporally disparate dataset (e.g. Massom et al., 2006; Worby et al., 2011; Xie et al., 2011). On a regional scale, microwave brightness temperatures detected by the spaceborne Advanced Microwave Scanning Radiometer-Earth Observing System (AMSR-E) instrument have been used to estimate snow depth (Comiso et al., 2003; Worby et al., 2008a). AMSR-E snow depth agrees generally with ship-based observations following the ASPeCt protocol (Worby et al., 2008b), and has been used to estimate Antarctic sea-ice thickness from ICESat observations (Yi et al., 2011; Zwally et al., 2008). However, the low spatial resolution (25 km / pixel) and tendency to understimate snow depth around ridged ice (Stroeve et al., 2006; Worby et al., 2008a) limit the utility of this dataset for estimating ice thickness using altimeter observations and Equation 1.1. Markus et al. (2011) made improvements in passive microwave estimates of snow depth to account for surface roughness, but the coarse resolution remains an issue that effectively prevents use of this dataset as a snow depth parameter for high resolution altimeters.

One approach taken for laser altimetry from ICESat missions has been to group laser shots into 25 km grid cells, matching to AMSR-E resolution (e.g. Kern et al., 2015; Kurtz et al., 2012; Zwally et al., 2008). For oceanic basins and circumpolar estimates of ice thickness this is a reasonable approach. However, the topography of Antarctic sea ice is highly variable on much smaller scales (Hutchings et al., 2012; Massom et al., 2006; Worby et al., 2011; Xie et al., 2013). Airborne instruments may capture topography on the scale of metres- to tens-of-metres, but without coincident laser and RADAR altimetry (e.g. Kurtz et al., 2013; Kwok and Maksym, 2014) snow depth at these scales must be estimated from empirical knowledge of in situ snow depth and total freeboard.

Wadhams et al. (1992) worked on the principle that a relationship existed between the snow/ice/air and ice/ocean interfaces of sea ice, based on airborne laser profiling and under-ice sonar observations from submarines in the Arctic. Alexandrov et al.

(2010) derived a linear regression model from in situ total freeboard and ice thickness observations, applied it to satellite altimetry observations, and found that modelled ice thickness was comparable with in situ observations. Doble et al. (2011) investigated the relationship between surface topography and ice draft using airborne LiDAR and under-ice draft measurements from upward looking sonar, finding was that the relationship improved with increasing scales of observation. They also deduced a length scale for the assumption of isostacy in Arctic sea ice of roughly 70 m for level ice. Xie et al. (2011) deduced that snow depth on sea ice in the Bellingshausen Sea could be predicted by a simple linear regression model based on in situ total freeboard and snow depth measurements. This relationship was also explored for East Antarctic sea ice (Worby et al., 2011), who found that the relationship between total freeboard and snow depth is heavily skewed by measurements where the underlying ice freeboard makes up a substantial component of the total freeboard. Ozsoy-Cicek et al. (2013) derived a set of snow depth models for broad sectors around the Antarctic continent, examining snow depth at a spatial scale of hundreds of metres or more. This extended previous work at smaller scales, providing a set of snow depth estimation models for circumpolar sea-ice thickness estimates from satellite altimetry.

Efforts to understand snow depth have largely focussed on satellite-scale observation of Antarctic sea ice, on the scale of hundreds of metres to kilometres. With few exceptions, altimetry data are used to populate much coarser grid cells. For smaller-scale missions, e.g. airborne laser altimetry focussed on a specific region and season, or proposed satellite-based instruments (e.g. ICESat-2, Abdalati et al., 2010), using AMSR-E snow depth estimates over 25 km grid cells is not representative of reality. Xie et al. (2013) provide an example of how the inference of snow depth at different scales affects the derived ice thickness using ICESat altimetry (60 - 70 m diameter spots), AMSR-E snow depth (12.5 km/pixel) and snow depth derived by empirical models using in situ snow depth and total freeboard measurements. They provide compelling evidence that for higher resolution altimetry, linear regression models for estimating snow depth derived from total freeboard are an attractive method. However, no analysis of the performance of linear regression modelling to estimate snow depth at scales smaller than ICESat footprints exists.

In this chapter, the focus is on two questions: how well do snow depths from linear regression models match reality for sea ice off the coast of East Antarctica? And how do these snow depth estimates influence derived ice thicknesses? In situ datasets obtained from voyages into the East Antarctic pack-ice zone in the late winter/early spring of 2003, 2007 and 2012 are used to derive snow depth models, then compare derived snow depths and ice thicknesses with observed values. Data sources are described in Section 2. In Section 3 linear regression models are derived for snow depth from each voyage. In Section 4 a comparison between linear regression models for snow depth and in situ observations is given using three different ice scenarios (variable thickness with heavy snow, mostly uniform, and highly deformed with heavy snow). In Section 5, the effect of choices of snow depth and densities on ice thickness derived using Equation 1.1 is shown. In section 6 ice thickness is derived from total freeboard and modelled snow depth, then compared with in situ observations.

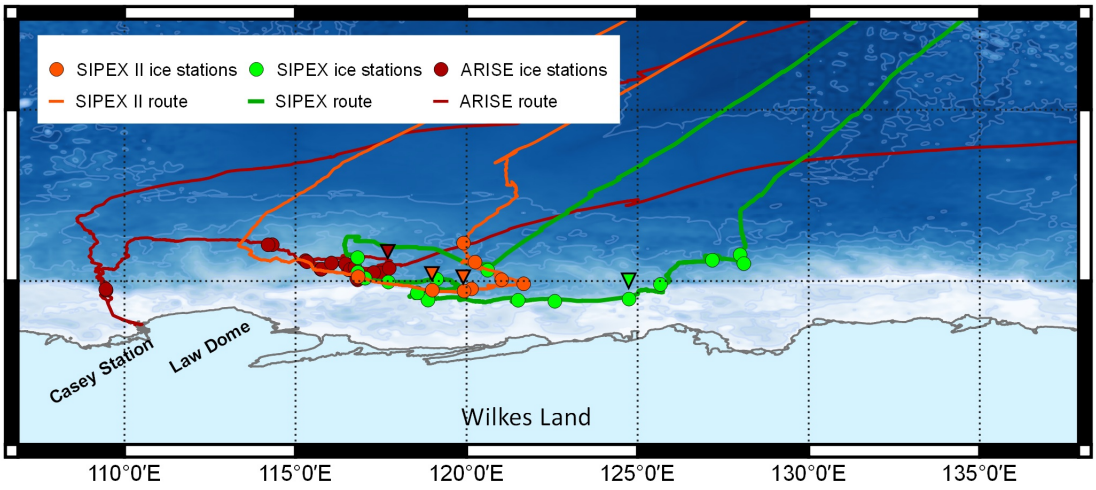

Figure 2.1: In situ sea-ice sampling sites and ship tracks for SIPEX-II (orange, $n = 8$ with 5 usable transects), SIPEX (green, $n = 14$ with 12 usable transects) and ARISE (red, $n = 9$ with 12 useable transects). Sites used for analysis in this paper are marked with inverted triangles. On each voyage site numbering increased from west (right) to east (left). Bathymetry and contours from the GEBCO digital atlas, Antarctic coastline from the SCAR Antarctic Digital Database v6.

2.2 Data description

In situ data from three research voyages aboard *RSV Aurora Australis* to the East Antarctic pack-ice zone in spring are used for the following analyses: ARISE 2003 (Massom et al., 2006), SIPEX 2007 (Worby et al., 2011) and SIPEX-II 2012 (Heil et al., 2014) all in the region 110° - 130° E. Figure 2.1 shows the relative location of voyage tracks and field sampling sites. The general strategy for data collection is to measure snow depth, ice thickness and ice freeboard in holes drilled through the sea ice at 1 m intervals along 100 to 200 m 'transects'. The ideal scenario does not always occur, and in this study profiles vary from 50 to 500 m in length with sample spacing up to 5 m between drill holes. Such floe-scale measurements usually coincide with a multi-disciplinary observation program on the same ice floe, and the overall measurement site is referred to as an 'ice station'. These sites are inherently biased toward sea ice which is both ship-navigable and thick enough to work on, meaning that the extremes of the sea-ice thickness distribution are generally not represented. However, some randomness is introduced to the sampling strategy by logistical constraints, with sampling lines being determined in an uncontrolled fashion by the direction of surface wind relative to the orientation of the ship once parked at the ice floe.

Measurements of snow depth were collected by forcing graduated probes into undisturbed snow until the end of the probe contact an unbreakable hard layer. In general this layer was the ice/snow interface. Snow depth was also measured when snow was cleared for drilling through ice. If a disparity existed between probed and snow pit measurements, the latter was recorded. Ice thickness and freeboard measurements were collected by

voyage	μZ_i	$\tilde{x}$	Mo	σZ_i	μF_i	$\tilde{x}$	Mo	σF_i	μZ_s	$\tilde{x}$	Mo	σZ_s	N valid (N total)
ARISE	1.21	0.65	0.5	1.08	0.04	0.03	0.02	0.12	0.21	0.13	0.05	0.2	1132 (2148)
SIPEX	0.93	0.79	0.66	0.51	0.06	0.035	0	0.10	0.15	0.12	0.01	0.13	1558 (2415)
SIPEX-II	2.33	1.75	0.97	1.63	0.12	0.06	0.05	0.19	0.41	0.4	0.5	0.23	439 (1135)
Combined	1.23	0.87	0.5	1.07	0.06	0.03	0.02	0.13	0.21	0.14	0.05	0.19	3129 (5698)

Table 2.1: Summary statistics for in situ sea-ice observations from ARISE, SIPEX and SIPEX-II. Measurements in metres, Z_i = ice thickness, F_i = ice freeboard, Z_s = snow depth. The symbol $\tilde{x}$ denotes the population median, Mo the mode.

weighted tape measures or rulers with expanding hooks which were designed to lodge at the undersurface of the ice. Ice thickness was measured at the ice surface, freeboard where the measuring device passed through the water surface. In the case of negative ice freeboard, measurements of the difference between the ice surface and water level were taken after flooding through the drilled hole had ceased. Where ice freeboard exceeds 0.15 - 0.2 m, the sea surface is not directly visible in the drill hole. Measurements rely on observers identifying the moment a weighted tape measure or ruler contacts the sea surface as it is lowered. For all measurements, a realistic maximum precision in field conditions was 5 mm. For ice thickness, a further assumption is made that devices designed to measure ice thickness are catching on the underside of the ice and not in some interstitial space between blocks of ice.

From these three voyages there were 5698 sampling sites, of which 3129 were suitable for use in this study - the requirement for usage being that coincident measurements of ice thickness, freeboard and snow depth occurred at the site. All three measurements are required to develop empirical models for snow depth, so any drill sites where fewer than these three measurements were recorded are excluded from this analysis.

Table 2.2 gives a transect-by-transect overview of the in situ data used in this study. Observations are often irregularly spaced, and at some sites external factors (time, safety) constrain sampling to larger intervals with points 2 or 5 m apart. Considering the differences between sampling sites in similar locations (e.g., ARISE site 6, SIPEX site 12, SIPEX-II site 8), it is attractive to treat each of the three voyages as independent datasets which tell a story about inter-season variability. However, given uncertainty about the forcing during ice formation and distribution prior to each voyage, sampling goals, and sampling strategies, a rigorous inter-voyage comparison is not possible. For the purposes of this paper - deriving and assessing an empirical model of snow depth from total freeboard, the dataset is treated as 3129 independent observations, and ask the reader to re-imagine the data presented here as a contiguous set of observations with roughly metre spacing. While not strictly accurate, there are no specific georeferencing data for each observation - and selection of sampling sites is a pseudo-random process. Given these factors, the data used here are treated as a contiguous set.

Of relevance to this study are the freeboard-related values presented in columns 12, 13 and 14 of Table 2.2. The ratio of ice freeboard to total freeboard F_i/F for each observation is derived to show the contribution of ice to the total freeboard signal, giving mean values in

column 12. The summary for each voyage shows that ice makes up a substantial portion of total freeboard (17.9 - 27.2 %). The standard deviation of the ratio F_i/F gives an indication of variability in total freeboard composition between transects within a given voyage.

In addition to the standard deviation of total freeboard per-transect (μF), a windowed standard deviation over 10 or 20 observations (given in the 'window' column) for each transect is derived as a proxy for surface roughness. This was used to investigate correlations between deformed ice and snow depth ($r^2\sigma\tilde{F}$ to Z_s) at approximately the tens-of-metres scale. Only one transect (SIPEX-II ice station 6) shows a reasonable correlation between roughness and snow depth at this scale. Using whole-of-voyage datasets the window size is expanded the window size to 100 observations to approximate a scale of roughly 100 m, and found no relationship. However, using the standard deviation of total freeboard and the mean snow depth for entire transects there was a moderate correlation between snow depth and total freeboard variability for ARISE ($r^2 = 0.45$) and SIPEX ($r^2 = 0.67$), but no relationship existed for SIPEX-II ($r^2 = 0.006$).

The value of seeking out observations on diverse ice types is shown by the contribution of the SIPEX-II dataset. Direct sampling on heavily deformed thick ice is rare in the historical dataset, leading to the generalisation that mean ice thickness on the Southern Ocean is roughly a metre. Observations described here, alongside Williams et al. (2014b) and Toyota et al. (2016) show that much thicker sea ice with deep snow loading exists, and is potentially undersampled.

2.3 Snow depth modelling using linear regression

Following Xie et al. (2011), Worby et al. (2011) and Ozsoy-Cicek et al. (2013), a linear fit is computed with total freeboard as the independent variable and snow depth as the predicted value, or dependent variable. Worby et al. (2011) pointed out that there were two distinct relationships between snow depth and total freeboard , separated by an ice-freeboard threshold of 0.12 m. Of the three voyages investigated here, only the SIPEX data show this pattern. For ARISE and SIPEX-II data there is a strong linear relationship between total freeboard and snow depth where ice freeboard is below some threshold. Where ice freeboard is high, the linear relationship between total freeboard and snow depth breaks down (See Figure 2.2). No physical explanation for these thresholds has been determined at the time of writing. However - the SIPEX dataset contains nearly as many observations as both the ARISE and SIPEX-II datasets combined, leaving open the suggestion that a similar pattern may emerge for any field sampling exercise given a sufficient number of drill holes over a wide range of ice types. A unity line is plotted (e.g. Kwok and Maksym, 2014) to demonstrate that the majority of samples taken on all voyages had positive ice freeboard. Figure 2.2 shows the relationship between snow depth and total freeboard for each of the three research voyages used here, and for all observations combined.

Voyage specific regression models were derived from in situ data following the same approach (Table 2.3). With respect to the numbered regression relationships shown in

Table 2.2: Statistics for in situ sea-ice observations from ARISE, SIPEX and SIPEX-II by voyage and transect. Measurements are given in metres. The term $\mu F_i/F$ gives the mean ratio of ice freeboard to total freeboard, or the amount of the freeboard signal made up of ice for each transect. $r^2\sigma\tilde{F}$ to Z_s gives the correlation of standard deviation of total freeboard after windowing (window length given in the final column) to snow depth, aiming to investigate tens-of-metre to hundreds-of-metre scale relationships between surface roughness and snow depth.

	μF_i	σF_i	μZ_s	σZ_s	μF	σF	μZ_i	σZ_i	$\mu draft$	$\sigma draft$	$\mu F_i/F$	$\sigma F_i/F$	$r^2\sigma\tilde{F}$ to Z_s	length (m)	N	window
ARISE																
1	0.064	0.041	0.045	0.048	0.109	0.067	0.893	0.547	-0.829	0.515	0.604	0.192	0.119	100	101	20
2	0.052	0.067	0.395	0.184	0.446	0.202	1.509	0.855	-1.458	0.829	0.126	0.130	0.005	99	50	20
3	0.036	0.033	0.341	0.180	0.377	0.166	1.464	0.658	-1.428	0.648	0.164	0.199	0.033	100	51	20
4A	0.034	0.075	0.160	0.154	0.194	0.173	0.811	0.561	-0.778	0.552	0.248	0.206	0.334	500	322	20
4B	0.053	0.179	0.191	0.207	0.245	0.297	1.158	1.135	-1.105	1.124	0.270	0.200	0.314	500	330	20
4C	0.031	0.101	0.284	0.232	0.315	0.244	1.732	1.304	-1.701	1.307	0.210	0.226	0.297	500	330	20
5	0.081	0.097	0.297	0.142	0.378	0.144	1.387	0.869	-1.306	0.817	0.222	0.216	0.098	100	51	20
8	-0.025	0.012	0.077	0.026	0.052	0.023	0.220	0.020	-0.245	0.019	0.003	0.015	0.008	50	26	10
9	0.019	0.052	0.289	0.090	0.308	0.111	0.931	0.427	-0.912	0.414	0.067	0.104	0.058	100	76	20
10	0.041	0.069	0.328	0.171	0.369	0.197	1.168	0.883	-1.127	0.848	0.099	0.124	0.005	100	56	20
11	0.032	0.022	0.022	0.040	0.053	0.044	0.663	0.256	-0.631	0.256	0.770	0.373	0.007	125	24	10
13	0.025	0.015	0.049	0.019	0.074	0.024	0.466	0.078	-0.441	0.071	0.329	0.165	0.029	50	51	20
total	0.040	0.109	0.212	0.200	0.252	0.232	1.163	1.009	-1.123	1.000	0.179	0.139	0.066	2325	1468	100
SIPEX																
1	0.040	0.047	0.176	0.102	0.216	0.107	0.815	0.535	-0.774	0.524	0.214	0.211	0.014	100	101	20
2	0.032	0.069	0.198	0.127	0.231	0.141	1.026	0.373	-0.994	0.345	0.167	0.200	0.011	200	200	20
3	0.04	0.050	0.171	0.139	0.220	0.145	0.987	0.435	-0.938	0.414	0.286	0.251	0.066	100	100	20
5	0.037	0.033	0.091	0.056	0.129	0.050	0.713	0.128	-0.676	0.116	0.332	0.251	0.011	200	201	20
6	0.085	0.059	0.020	0.025	0.105	0.051	1.151	0.675	-1.066	0.664	0.712	0.334	0.020	200	124	20
8A	0.021	0.043	0.090	0.057	0.111	0.051	0.560	0.383	-0.540	0.356	0.233	0.266	0.237	252	63	20
8B	0.008	0.009	0.087	0.040	0.095	0.036	0.359	0.021	-0.352	0.018	0.112	0.126	0.000	194	40	10
9	0.135	0.174	0.438	0.222	0.573	0.237	2.223	0.821	-2.089	0.742	0.241	0.252	0.041	50	51	20
10	0.025	0.056	0.093	0.066	0.118	0.058	0.694	0.459	-0.669	0.417	0.256	0.276	0.051	200	201	20
11	0.288	0.142	0.216	0.135	0.504	0.265	1.058	0.324	-0.770	0.322	0.591	0.092	0.165	100	101	20
13	0.073	0.093	0.152	0.106	0.225	0.133	1.040	0.447	-0.967	0.425	0.321	0.251	0.042	200	201	20
14	0.040	0.080	0.215	0.127	0.255	0.123	1.142	0.765	-1.102	0.771	0.181	0.243	0.203	200	201	20
total	0.062	0.100	0.152	0.132	0.215	0.172	0.959	0.582	-0.897	0.557	0.272	0.360	0.063	1996	1584	100
SIPEX-II																
2	0.091	0.131	0.348	0.207	0.440	0.247	1.642	1.067	-1.551	1.007	0.188	0.190	0.137	100	95	20
3	0.124	0.132	0.436	0.277	0.560	0.270	1.791	0.460	-1.667	0.464	0.280	0.282	0.010	100	55	20
4	-0.017	0.047	0.474	0.124	0.456	0.119	1.374	0.597	-1.392	0.596	0.027	0.058	0.050	100	101	20
6	0.098	0.105	0.270	0.212	0.367	0.192	1.731	0.780	-1.633	0.728	0.334	0.291	0.628	100	97	20
7	0.281	0.261	0.514	0.251	0.795	0.266	4.873	1.247	-4.591	1.174	0.352	0.253	0.085	99	99	20
total	0.114	0.184	0.407	0.232	0.521	0.269	2.335	1.635	-2.221	1.532	0.210	0.283	0.012	499	447	100

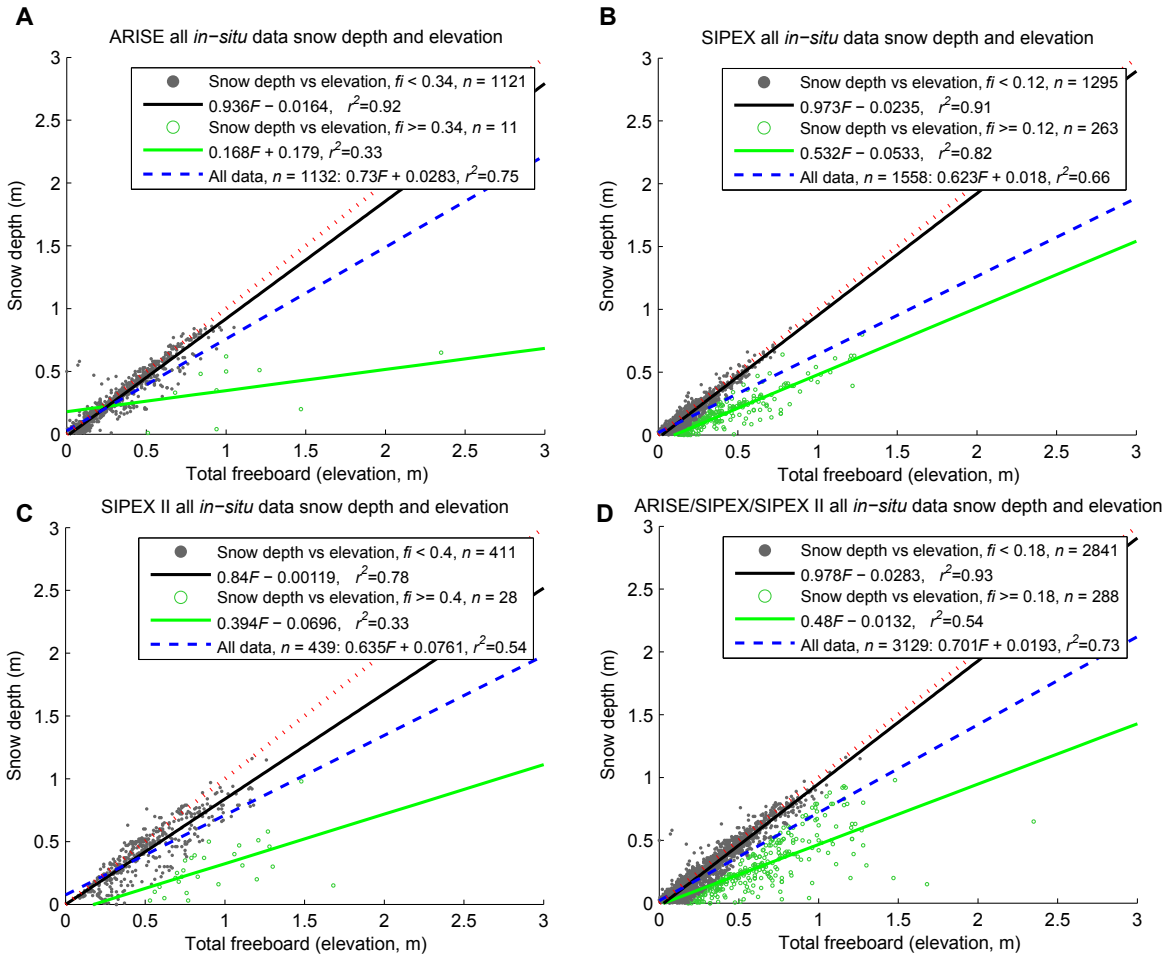

Figure 2.2: Regression models for predicting snow depth from total freeboard. Datasets were split by ice freeboard at points which optimised the linear relationship between total freeboard and snow depth for one or both of the models derived from observations with high or low ice freeboard. The red dashed line shows the relationship $x = y$, above which snow depth makes up all of the total freeboard signal and below which snow depth accounts for only part of the total freeboard signal.

Table 2.3, Relationship 2.1 was derived in early spring, at the western edge of the area surveyed by the three voyages examined. Relationship 2.4 was developed from highly variable sea ice with a relatively thin snow cover in early to mid spring, at the eastern limit of the region studied. Relationship 2.7 was derived from heavily deformed, very thick ice floes. The sampling season was slightly later, and the experimental region overlapped both ARISE and SIPEX substantially. Finally, observations from all three voyages were combined to derive Relationship 2.10, as a potential candidate for an empirical East Antarctic snow depth model.

Following (Worby et al., 2011) an ice-freeboard threshold was estimated below which the apparent clusters of observations around $F_i = Z_s$ were described very well by a linear regression model (grey points, Figure 2.2, relationships 2.2, 2.5, 2.8, and 2.11). These thresholds are 0.34 m for ARISE, 0.12 m for SIPEX, 0.4 m for SIPEX-II, and 0.18 m

Source	Ice type	Relationship (number)		r^2
ARISE	all samples	$Z_s = 0.73F + 0.028$	(2.1)	0.75
ARISE	fi <0.34	$Z_s = 0.94F - 0.016$	(2.2)	0.92
ARISE	fi >0.34	$Z_s = 0.17F + 0.18$	(2.3)	0.33
SIPEX	all samples	$Z_s = 0.62F + 0.018$	(2.4)	0.66
SIPEX	fi <0.12	$Z_s = 0.97F - 0.024$	(2.5)	0.91
SIPEX	fi >0.12	$Z_s = 0.53F - 0.053$	(2.6)	0.82
SIPEX-II	all samples	$Z_s = 0.64F + 0.076$	(2.7)	0.54
SIPEX-II	fi <0.4	$Z_s = 0.84F - 0.0012$	(2.8)	0.78
SIPEX-II	fi >0.4	$Z_s = 0.39F - 0.069$	(2.9)	0.33
All observations	all samples	$Z_s = 0.701F + 0.019$	(2.10)	0.73
All observations	fi <0.18	$Z_s = 0.978F - 0.028$	(2.11)	0.93
All observations	fi >0.18	$Z_s = 0.48F - 0.013$	(2.12)	0.54

Table 2.3: Regression models for snow depth from total freeboard derived using East Antarctic in situ observations

when combining all three voyages. Above these ice freeboard thresholds, for all except SIPEX observations, a linear model performed poorly as a predictor of snow depth from total freeboard (green points, Figure 2.2, relationships 2.3, 2.6, 2.9, and 2.12).

Observations where ice freeboard exceeded these thresholds accounted for 12% of all data, sufficient to skew the regression models substantially when included. This is somewhat reflective of observations from Kwok and Maksym (2014), where scatter in the relationship between total freeboard and snow depth increased in regions of higher total freeboard. For most Antarctic regions, coincident remote sensing of total freeboard and snow depth is not carried out. Therefore it is impossible to distinguish relationships for high- and low ice freeboard regions. For the current study, models derived from all samples (e.g. relationships 2.1, 2.4, 2.7, 2.10) must be used for modelling snow depth on sea ice.

Table 2.4 shows mean snow depth for all in situ observations, compared with mean snow depths derived by relationships 2.1, 2.4, 2.7, and 2.10. While differences between in situ and modelled mean snow-depth are in the order of a few centimetres, these figures give no indication of how applying regression models for snow depth will impact ice thickness estimates which rely on them.

Model	μZ_s	σZ_s
in situ	0.21	0.19
2.1	0.23	0.18
2.4	0.18	0.14
2.7	0.25	0.15
2.10	0.21	0.16

Table 2.4: Comparing mean snow-depth from in situ observations and empirical models 2.1, 2.4, 2.7, and 2.10 for all voyages ($N = 3129$)

2.4 Comparison of modelled snow depth with in situ snow measurements.

A reasonably accurate estimate of snow depth is crucial for sea-ice thickness estimation from altimeters which see only the uppermost surface of sea ice (Alexandrov et al., 2010; Kern et al., 2015; Kurtz et al., 2012; Kwok and Cunningham, 2008; Kwok and Maksym, 2014). Here, modelled snow depths are compared with those obtained from in situ observations using a set of drill-hole transects - one sampled during the ARISE (2003) voyage, one from SIPEX (2007) and two from SIPEX-II (2012). These transects were selected on the basis that they are representative of the ice types encountered off East Antarctica from all three voyages, and should not be taken as typical of one voyage or another. Figure 2.3 shows a snow and ice freeboard profile from 100 m of each transect line. The models used to estimate snow depth from total freeboard are based on relationships 2.1, 2.4, 2.7 and 2.10. The regression model for snow on East Antarctic pack ice using both positive and negative ice freeboard observations derived by Ozsoy-Cicek et al. (2013) is included to determine whether the relationship between total freeboard and snow depth at longer (hundreds of metres) length scales provides a reasonable estimate of snow depth for higher-resolution observations.

As expected, snow depths modelled by linear regression from total freeboard match in situ observations well when ice freeboard is a small proportion of the total freeboard signal (Figure 2.3b). Where there is a substantial ice freeboard component in the total freeboard signal (Figure 2.3a, c and d), snow depth is overestimated. When the underlying ice is highly deformed, the models perform poorly (e.g. Figure 2.3c, 80-100 m). In a heavy snow cover on thick ice, snow depth is underestimated (Figure 2.3c and d). SIPEX-II transect 7 (Figure 2.3d) is included to demonstrate how the modelled snow depth responds over very thick, highly deformed sea ice. In this case the ice freeboard threshold (0.4 m) above which the relationship between total freeboard and snow depth breaks down is exceeded often, and total freeboard is a poor predictor of snow depth ($r^2 = 0.24$).

The model of Ozsoy-Cicek et al. (2013) gives a reasonable approximation of snow depth at the scale of a single transect, if snow depth closely tracks total freeboard. For the SIPEX and SIPEX-II transects, the snow depth was best estimated using only in situ observations from the relevant voyage. For ARISE, however, the best snow model was derived from all available observations from all voyages. In all cases the mean modelled snow depth

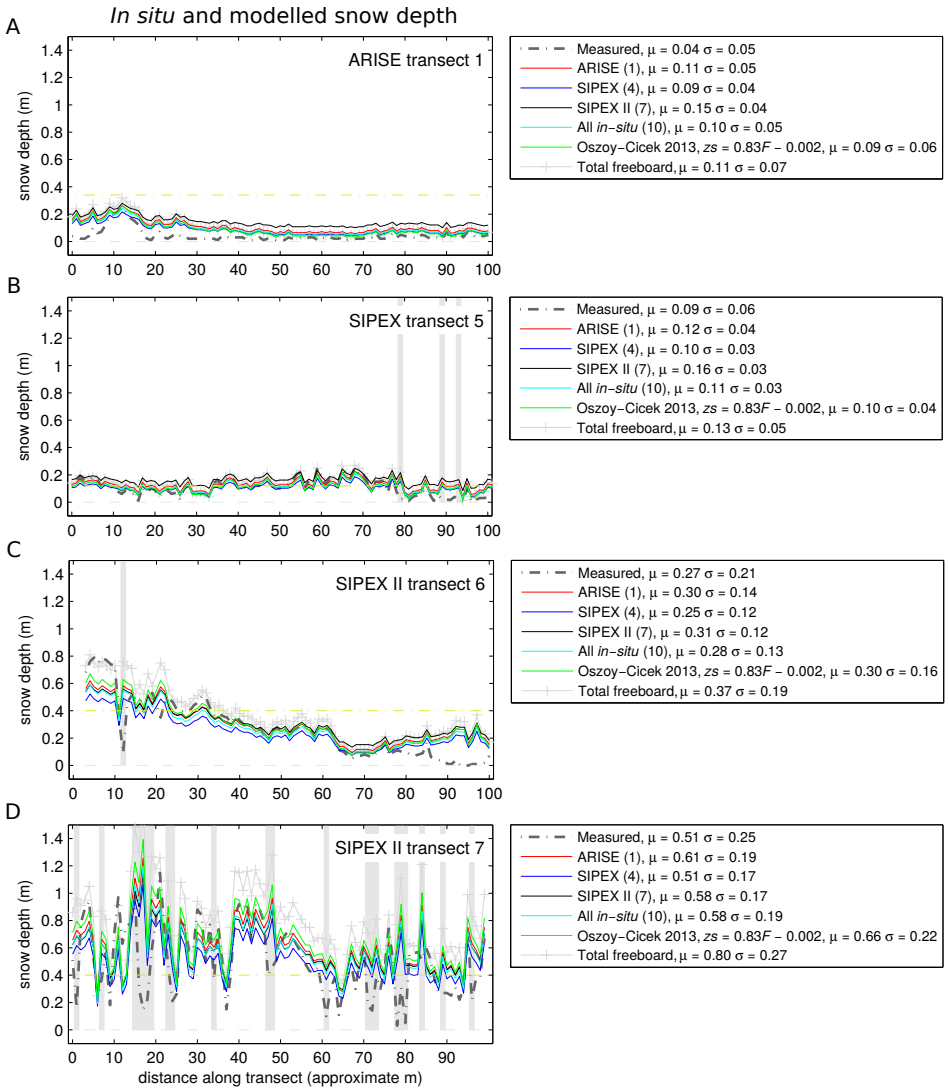

Figure 2.3: Modelled vs in situ snow depth for ARISE site 1 (A), SIPEX ice station 5 (B), SIPEX-II ice station 6 (C) and SIPEX-II ice station 7 (D). Bracketed numbers in the legend give relationship models in Table 2.3, the horizontal light grey dashed line is relative sea level, the yellow dashed line is the ice elevation threshold from Table 2.3, and grey bars show points where F is greater than the ice freeboard threshold above which linear modelling breaks down for SIPEX and SIPEX-II observations. Total freeboard is shown to highlight the tracking behaviour of snow-depth models and where they diverge from measured snow depths.

is within or close to the mean in situ snow depth plus or minus one standard deviation. It is apparent, however, that the distribution of snow depth is less well modelled with snow depth tracking surface topography and ignoring under-ice features. Interestingly, SIPEX-II transect 6 demonstrates the effect of averaging snow depths and ice thickness over transect lines or larger scales. The mean and variance give no appreciation that the contribution of snow to total freeboard steadily reduced over the transect, with deep snow encountered in the first 50 m and relatively little snow in the final 20 m.

ρ snow	$305.67 kg/m^3$	ARISE, SIPEX, SIPEX-II in situ, $n = 301$
ρ ice	$900 kg/m^3$	Hutchings et al. (2015); Ozsoy-Cicek et al. (2013); Price et al. (2014); Worby et al. (2011)
ρ water	$1028 kg/m^3$	Hutchings et al. (2015)

Table 2.5: Ice, snow and water densities used for modelling sea ice thickness

2.5 The impact of snow depth model choice on ice thickness estimates

Ice thickness estimates generated using Equation 1.1 are highly sensitive to elevation and snow depth (Kern et al., 2015; Kwok and Cunningham, 2008; Spreen et al., 2006). In Figure 2.4 the effects of snow-depth estimation strategy on resulting ice thickness using empirical models (Table 2.3) is shown.

Holding densities constant, regression models with a lower slope should result in thicker ice estimates as total freeboard increases, since the slope reflects the proportion of the total freeboard signal which is modelled as snow. Figure 2.4a shows that this is the case. Snow depth modelled with a slope of 0.62 (SIPEX, relationship 2.7) results in approximately 0.5 m thicker ice at 1 m total freeboard compared to a snow model with a slope of 0.73 (ARISE, relationship 2.1), using densities given by Table 2.5. The relationship for East Antarctic pack ice derived by Ozsoy-Cicek et al. (2013) with a slope of 0.83 behaves as expected, with relatively thicker ice for total freeboard near sea level and thinner ice as total freeboard increases.

Snow density used for Figure 2.4a was the mean value from measurements taken on the three voyages described here. Figure 2.4b shows ice thickness modelled using snow densities in the 1-σ range of observations, and holding all other parameters constant. The range of possible snow densities shown here accounts for up to 0.4 m of ice thickness using mean snow depth and ice freeboard from all three voyages ($Zs = 0.21$ m, $Fi = 0.06$ m, Table 2.1).

In this analysis $900 kg/m^3$ (e.g. Ozsoy-Cicek et al., 2013; Worby et al., 2011) is used as a middle ground between an upper bound of observed ice density of $934 kg/m^3$ on fast ice suggested by Price et al. (2014), and a lower bound of $870 kg/m^3$ for columnar pack ice (Hutchings et al., 2015). Holding snow depth, snow density, water density and total freeboard constant, the range between these bounds equates to around 0.5 m of ice thickness (Figure 2.4c), with thickness increasing for greater ice densities. Again, snow depth and ice freeboard used here are the mean values from all three voyages. Varying the density of seawater has little impact on modelled ice thickness (Figure 2.4d).

This exercise demonstrates that the choice of snow-depth model may account for up to 0.5 m offset in estimated ice-thickness when using these empirical relationships between total freeboard and snow depth. The choice of ice and snow density are also key factors in developing ice-thickness estimates, with 0.4 - 0.5 m of ice thickness represented across the 1-σ range of snow density; and the published range of ice densities.

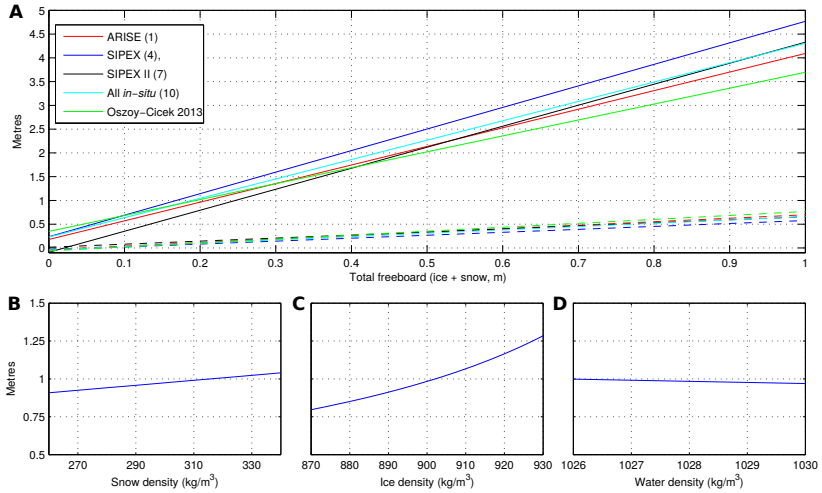

Figure 2.4: A: Impact of choice of snow depth model on ice thickness estimated using Equation 1.1. Solid lines show ice thickness, dashed lines show modelled snow depth. Colours show relationships used to derive snow depth. B - D: Sensitivity of ice thickness to ice density, snow density and seawater density.

2.6 Ice-thickness estimation using snow depth modelled by linear regression

The motivation for modelling snow depth from elevation is to use snow-depth estimates to derive sea-ice thickness, and eventually ice volume from altimetry observations. In this section snow depths derived by linear regression are used to estimate ice thickness, then compare results using different modelled snow depths with in situ ice thickness along drill-hole transects.

Equation 1.1 is sensitive to snow depth, and the choice of snow, ice and water densities. In order to provide a realistic comparison with in situ ice thickness the hydrostatic model is populated with values derived from field data obtained off East Antarctica, given in the previous section (see Table 2.5).

Using the transects analysed previously (Figure 2.3), model realisations using in situ total freeboard measurements in place of altimetry data are used to estimate ice thickness. In this way the uncertainty in ice thickness due to sensor error is minimised. Snow depth and the densities of snow, ice and water are the primary drivers of any mismatch between in situ observed ice thickness and ice thickness modelled using Equation 1.1. Snow depth is derived using relationships given in Table 2.3 and snow, ice and water densities are held constant for all transects. Figure 2.5 shows ice thickness modelled for the selected transects on ARISE, SIPEX and SIPEX-II from empirically derived regression models for snow depth. Ice thickness modelled from in situ snow depth as input to Equation 1.1 is included for comparison.

In general, applying the hydrostatic equation with the snow and ice densities in Table 2.5 will underestimate ice thickness, even when in situ snow depth observations are used as

Voyage	Freeboard ratio	r^2
ARISE	0.17	0.28
SIPEX	0.27	0.42
SIPEX-II	0.20	0.28

Table 2.6: Ice freeboard to total freeboard ratio, and correlation between ice freeboard and total freeboard

input. Eliminating snow depth as an source of uncertainty this way ice, snow and seawater densities are the primary causes of ice thickness underestimation. Applying the upper bound of observed sea ice densities ($915 kg/m^3$) may solve part of the problem, adding approximately $0.1 - 0.15$ m to ice thickness (Figure 2.4b). This is, however, a fairly crude workaround - failing to bring estimated ice thickness for regions like the ARISE transect used here (Figure 2.5a) into the 1-σ range of in situ observations.

ARISE ice station 1 (Figure 2.5a) and SIPEX-II ice stations 6 and 7 (Figure 2.5c and d) captured a highly-variable snow depth and ice freeboard along the transect line. In these instances the snow depth is poorly modelled (Figure 2.3a, c and d). Consequently the model-derived ice thickness does not agree well with observations. For SIPEX ice station 5 (Figure 2.3b), where the snow depth is more evenly distributed, the best model fit to in situ observations is achieved with a snow-depth model derived from SIPEX observations (Relationship 2.4). Figure 2.5d shows a worst case scenario for sea-ice thickness estimation using altimetry - a highly deformed site with high and variable underlying ice freeboard. The snow depth mis-modelling associated with this sampling site (Figure 2.2d) feeds directly into a thickness estimation error in the order of metres.

A key difficulty in obtaining an accurate estimate of snow-depth distribution is the decoupling of surface and ice topography. Table 2.6 shows the relationship between the surface and ice topography for the three voyages used in this study. In general, surface topography is a poor predictor of both ice freeboard and draft, leading to poor estimates of the relative contribution of ice and snow to the total freeboard signal. For each voyage, the amount of ice contributing to the freeboard signal varied between 17 and 27 %.

For the most part, ice thickness over a 100-200 m transect is not well replicated using snow depths derived from empirical models predicting snow depth from total freeboard. The obvious decoupling of surface- and ice topography represents a substantial conundrum for high resolution laser altimetry - being how to represent realistic sea-ice thickness distribution from sparse observations.

2.7 Discussion

Implementing a simple, easy-to-apply model for snow depth over Antarctic sea ice is highly attractive for deriving circumpolar estimates of sea-ice volume using airborne or satellite-borne altimeters. Using a combined set of ARISE, SIPEX and SIPEX-II drill holes in

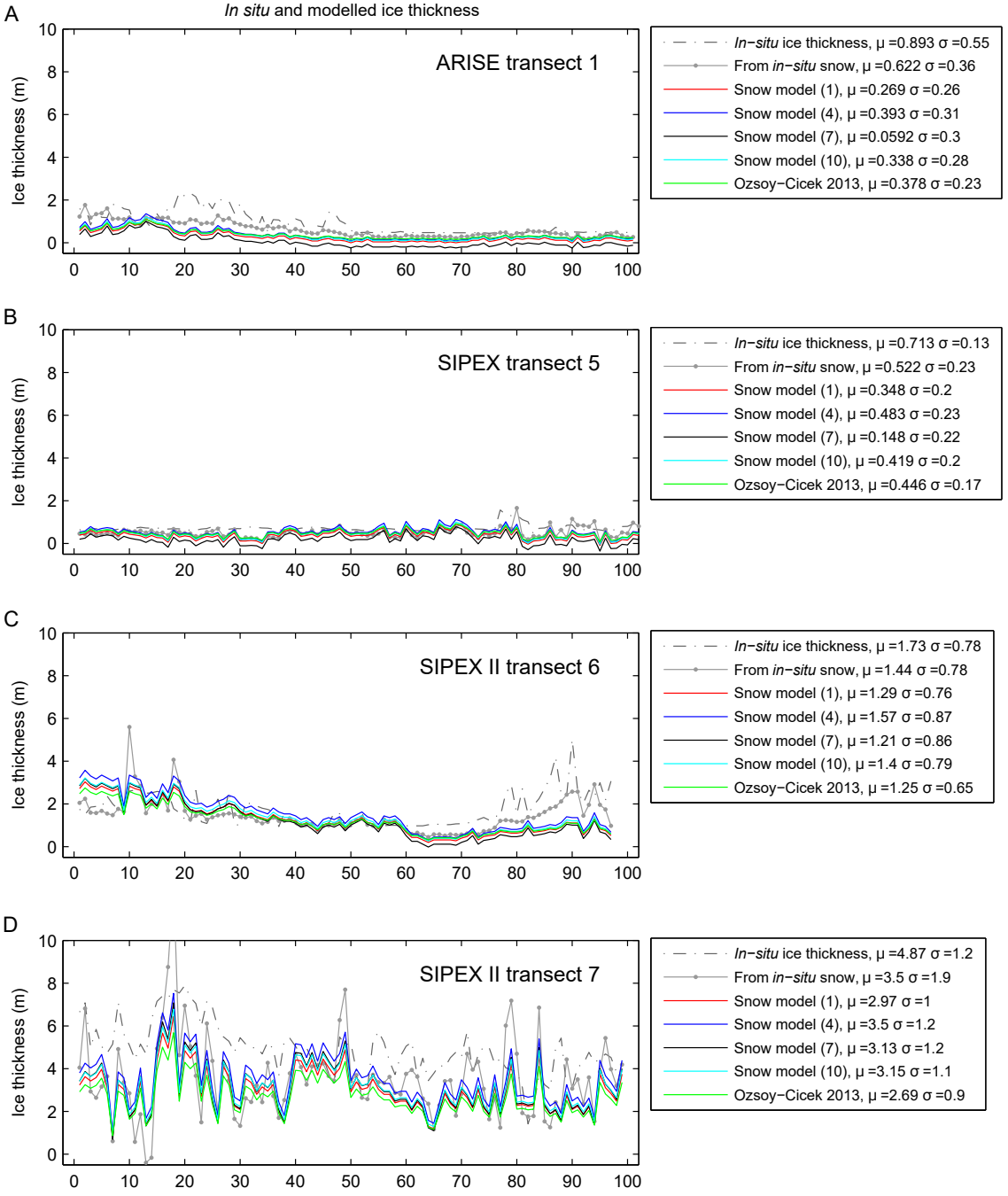

Figure 2.5: Modelled vs in situ ice thickness for ARISE site 1 (A), SIPEX ice station 5 (B), SIPEX-II ice station 6 (C), and SIPEX-II ice station 7 (D). At each site the in situ thickness is drawn as a broken grey line. Modelled ice thickness using Equation 1.1 are derived using in situ snow (grey line with points), and snow depths derived from total freeboard by relationships 1, 4, 7 and 10. Also shown are ice thicknesses derived using the snow depth relationship for East Antarctica sea ice from Ozsoy-Cicek et al. (2013)

the region 110° - 130° E a set of linear regression models for snow depth based on total freeboard is derived, resulting in a similar relationship to the model for East Antarctica derived by Ozsoy-Cicek et al. (2013). This gives a reasonable approximation of snow depth on East Antarctic pack ice at the scale of kilometres. However, as Doble et al. (2011) point out, differences between modelled draft and in situ draft increase as scales of observation become smaller. Further, they found a stronger relationship between total freeboard and draft for rougher regions. The observations presented here were not amenable to splitting into 'rough' and 'smooth' subsets. However, Figure 2.5c shows that over deformed ice at least, draft modelled in rougher surface regions is more representative of the actual under-ice topography. Unlike investigators in the Arctic, there is no attempt model freeboard using a direct relationship, noting that for the in situ observations examined here, surface topography is very poorly related to under-ice topography at length scales smaller than around 100 m, clearly apparent in the same figure.

For all regions, snow depth is overestimated - particularly in surface ridges. Worby et al. (2008a) determined that over 70% of East Antarctic sea ice could be considered 'rough' using a texture-based analysis of aerial photographs, which generally agrees with the percentage of deformed ice identified by Williams et al. (2014b) using upward-looking multibeam sonar deployed by Autonomous Underwater Vehicle (AUV). For comparison, the ASPeCt data derived from shipboard observations (Worby et al., 2008a) indicate that $8 - 18\%$ of Antarctic pack ice is ridged - which potentially reflects the desire of ships to travel in relatively thin, level ice.

The criteria for 'roughness' or 'deformity' and 'ridgedness' differ markedly, since 'roughness' and 'deformity' in remotely-sensed data are determined by mathematical methods, which detect deformed ice features which would potentially not be clearly identified as 'ridges' by an observer. The ASPeCt dataset ridge percentages, however, are based on clearly identifiable ice ridges distinct from the surrounding landscape. Consequently, modelling snow using the method described here will lead to overestimates of snow depth and underestimates of ice thickness for somewhere between 10 and 70 % of Antarctic pack ice.

Variability in snow and sea-ice density also needs to be considered when deriving sea-ice thickness from total freeboard and snow depth. While snow density is relatively well sampled, it is highly variable. Detailed knowledge of snow morphology underlying a set of altimeter observations would allow the application of different density parameters for flight segments. For ice density, observations are sparse and there is a clear need for a broader set of Antarctic sea-ice density observations.

An ice density range of $870 kg/m^3$ to $934 kg/m^3$ equates to around 0.5 m in modelled ice thickness for the model parameters used in this study. Using a mean snow depth of 0.41 m and total freeboard of 0.53 m (mean of SIPEX-II observations, Table 2.1), the same range of densities gives a difference of 0.94 m in derived ice thickness. Determining a realistic density is complicated by the nature of sea-ice as a composite material. Within any ice

station studied here, the sea ice in a sampled floe may consist mainly of consolidated ice with brine channels and air pockets, chunks with interstitial snow-filled spaces, or sea-ice blocks with seawater gaps in between, each with a different density and contribution to the overall mass and buoyancy of an ice floe. So the question of whether in situ measurements reliably capture sea-ice thickness remains open, as does the question of how to model sea ice thickness effectively from surface elevation.

Improving ice-thickness estimates by using the upper bound of ice density as a compensation for overestimated snow depth may be a reasonable approach, but difficult to validate. One could argue that using the ratio F_i/F to constrain the snow depth estimated by linear regression models for snow depth would help, but without coincident in situ observations corresponding to each altimetry mission this proposal quickly runs into the same issue of making an appropriate choice. The ratio is highly variable on the scale of single transects and for regions described here. Geiger et al. (2015) find that for Arctic sea ice, the assumption of isostatic balance inherent in Eq. 1.1 fails at point scales - meaning at the scale of drill hole collection or metre-scale altimetry observations. Hutchings et al. (2015) find densities as low as $728 kg/m^3$ for granular ice in heavily deformed sites, and clearly demonstrate that ice density is variable at sub-basin scales. In a highly deformed ice pack, it is plausible that ice density varies at a sub-floe scale. A deeper examination of variability in ice and snow density, and the assumption of isostasy for East Antarctic sea ice is recommended by this work, as it would undoubtedly provide useful insight into converting altimeter observations into reliable ice-thickness estimates.

Overall, modelling snow depth using linear regression appears to be well suited to determining large-scale mean values for snow and ice thickness. However determining a thickness distribution, or estimating the temporal and spatial variability, is difficult using this method in scenarios where ice freeboard makes a substantial contribution to the total freeboard - which appears to be the case for sea ice off East Antarctica. In regions where total freeboard more or less approximates snow depth (e.g. Xie et al., 2011, 2013), a thickness distribution will be more accurately represented where snow depth is estimated by a linear model using total freeboard as input. A more sophisticated statistical model which estimates the likelihood that a given topographical feature is all snow, or only some percentage of snow, might assist in modelling snow-depth distributions from available in situ observations.

Finally, the analysis conducted here does not consider the influence of total freeboard measurement error in remotely-sensed data. Depending on the choice of instrument, the uncertainty introduced by mis-modelling of snow depth may form only a small component of the overall uncertainty in sea-ice thickness estimation.

2.8 Conclusions

Investigating the pattern of floe-scale variability is important in determining how, where and why estimation uncertainties for snow depth and ice thickness on larger scales (e.g.

kilometres and greater) might occur. In particular, the technique of modelling snow on sea ice by linear regression generally overestimates snow depth over deformed sea ice, leading to underestimation of ice thickness derived from altimetry observations (and modelled snow). Given the possibility that current estimates of Antarctic sea-ice thickness may be low (Williams et al., 2014b), understanding the biases of ice-thickness estimates is critical.

On length scales greater than 1000 m (for example taking the mean of all available in situ observations), our findings confirm those of Ozsoy-Cicek et al. (2013): using an empirical snow depth model approximates in situ snow observations well and provides a reasonable estimate of sea-ice thickness. At scales smaller than a few hundred metres (one transect), the relationship between snow depth and total freeboard gives a less encouraging picture. At these scales, the relationship between snow topography and underlying ice topography is less certain, and the influence of small-scale variability (e.g. in ice density) is greater. For satellite-based altimetry this presents no real problem, as current spaceborne altimeters operate on the scale of hundreds-of-metres or greater per observation and circumpolar ice thickness distributions will be visualised and analysed at scales of hundreds- to thousands of metres (Worby et al., 2008b; Kurtz et al., 2012). For high resolution airborne instrument packages (e.g. Lieser et al., 2013; Studinger et al., 2010), it is helpful to understand how models for sea-ice thickness estimation operate, since the utility of these instruments lies in showing how smaller scale processes integrate into larger-scale satellite observations.

As Kwok and Maksym (2014) point out, the body of knowledge on Antarctic sea ice is limited by the pool of available field observations. Here, three intensive sampling campaigns in East Antarctic pack ice were compiled to show how current sea-ice thickness modelling from altimetry behaves when compared to a set of in situ observations. East Antarctica is relatively well populated with in situ measurements. The recent SIPEX-II voyage shows that the sea ice in this region still holds many surprises and the measurements collected over several years barely begin to characterise the region, let alone all of the Antarctic pack-ice zone. The evidence presented here suggests strongly that increasing the record of in situ observations will lead to improved snow estimation models and therefore sea-ice thickness distributions from altimetry. Without a method for sensing the snow-ice interface (e.g. Galin et al., 2012; Kwok and Maksym, 2014) or determining the spatial distribution of snow and ice densities, the clearest approach to a high resolution sea-ice thickness distribution for Antarctica may be to increase error margins for regions with relatively high total freeboard.

This research will ultimately be superseded by airborne and satellite-based instruments capable of coincident elevation and snow-depth measurements. However, the current holding of altimetry data over Antarctic sea ice will play an important role in extending the time series for estimates of a circumpolar Antarctic sea-ice thickness distribution. For that task the regression modelling approach to snow depth remains a viable method where coincident high resolution snow-depth observations do not exist, with respect to the limitations described in this work. The next step in working toward high resolution estimates of Antarctic sea-ice thickness is understanding the uncertainties

inherent in altimetry observations with airborne LiDAR, and how they propagate through to estimated snow and ice parameters. This is detailed in Chapter 3.

Chapter 3 The APPLS instruments and their uncertainties

3.1 Introduction

In the APPLS package, manufacturer's specifications provide a priori values for uncertainties for some measurement types - notably laser range accuracy and IMU angular measurement. Other uncertainties must be determined a posteriori or by adopting accepted values from the literature. The misalignment between the IMU and LiDAR instrument, known as the 'boresight misalignment', is treated as fixed for a given data collection flight, but must be determined after initial data processing (e. g. Glennie, 2007; Hodgson and Bresnahan, 2004; Shrestha et al., 2007; Slatton et al., 2007; Schaer et al., 2007). On the other hand, GPS positioning accuracy and aircraft attitude accuracy (derived from inertial measurments) are time dependent parameters which vary per-epoch within a single flight. GPS accuracy is based numerous factors including satellite visibility, tracking characteristics and aircraft dynamics.

How these uncertainties propagate through to a geophysical measurement is a subject of interest. With respect to LiDAR, Morin (2002) provides an overview of error sources in an airborne system. Glennie (2007) and Wallace et al. (2011) show how variance-covariance (VCV) propagation can be used to derive a priori 3D errors for several airborne LiDAR configurations, and to determine the relative contributions of each component to the overall 3D point uncertainty. For high relief terrain, Schaer et al. (2007) derived the incidence angle of a LiDAR strike on surveyed terrain by fitting a mesh to the point and its immediate neighbours. Using these data, they derive a 'Q factor' which described the overall quality of each laser point with respect to its 3D accuracy and underlying terrain. Over sea ice the surveyed terrain is essentially flat, but the work of Schaer et al. (2007) provides valuable insight into the visualisation of LiDAR uncertainties.

For the APPLS instrument, positioning of GPS antennae near the aircraft generator, and under rotor blades poses an additional challenge. The effects of the aircraft generator are difficult to quantify, since they are coupled with the passage of rotor blades overhead. Previous work on the passage of GPS signals through a rotor disk suggest that signal attenuation occurs (Brodin et al., 2005), with potential impacts on the ability of the associated receiver to robustly track GPS carrier phase observations (Stebler, 2008).

The main objectives of this chapter are to show how a LiDAR point cloud is realised using the APPLS instrument package, and how point positioning uncertainties are derived

from the system components. The APPLS instrument package layout is detailed, and instrument precisions described. A discussion of the equations for georeferencing airborne LiDAR, and VCV propagation through the LiDAR georeferencing equation follows. Sources of positioning uncertainty in the APPLS package are then discussed. VCV propagation methods are applied to the APPLS system, allowing visualisation of point uncertainty for LiDAR swaths from the APPLS package. A discussion of the results and recommendations for how to reduce uncertainty in APPLS observations concludes the chapter.

3.2 Instrument installation and description

From 2007 to 2012 the APPLS package was deployed in an Aerospatiale AS350 (Squirrel) single-engine light utility helicopter (Lieser, 2008). The aircraft was not dedicated to airborne surveying and the APPLS package needed to be installed in a way that had minimal impact on the airframe. Since the operating environment for the package was over polar oceans, a closed-aircraft system was also required to maintain cabin comfort for operators. With these factors in mind the configuration in Figure 3.1 was used (also shown schematically in Figure 1.5)

The APPLS instrument package was first flown in 2007 on the Sea Ice Physics and Ecosystem eXperiment (SIPEX) (Worby et al., 2011) using a Riegl LMS-Q240i scanning laser altimeter, an Oxford Technical Solutions (OxTS) 3000 series GPS/IMU with a single-frequency Novatel OEMV series GPS receiver, a Nikon D1X digital camera and a Heitronics KT-19 pyrometer. An additional instrument flown during SIPEX and for an expedition in 2008 was a broadband snow radar (see Galin et al., 2012). In 2008 the RT3000 was upgraded to an OXTS RT4003 strapdown navigation system with a dual-frequency Novatel OEMV GPS receiver (hereafter the RT-unit). In 2009, the D1X was retired and replaced with a Hasselblad H3DII-50 digital camera. For all operations, the RT-unit used two GPS antennae. The primary antenna (nearest the IMU) collected dual-frequency GPS observations (after 2008) that are used to position the instrument, and the secondary antennae provides a baseline for the estimation of aircraft heading.

Table 3.1 gives relative displacements between the primary GPS antenna and the RT-unit, the RT-unit and other instruments in metres in the RT-unit's reference frame (shown in red on Figure 3.1), which is considered equivalent to the aircraft body frame. These were measured using an engineering scale rule, plumb line and level in 2007, 2008, 2009 and 2010. In 2012, a reflectorless total station was used to directly sample displacements between instrument mounts as installed in the helicopter, from which instrument displacements could be inferred using engineering drawings of the instruments. A 3D laser scan of the as-flown APPLS package was undertaken at the same time as the total station survey. Figure 3.1 is drawn from the laser scan, to which engineering drawings of the instruments and their mounts were registered. This model was also used to estimate instrument displacements. From all sources, measurements agreed to within the bracketed precision given in Table 3.1.

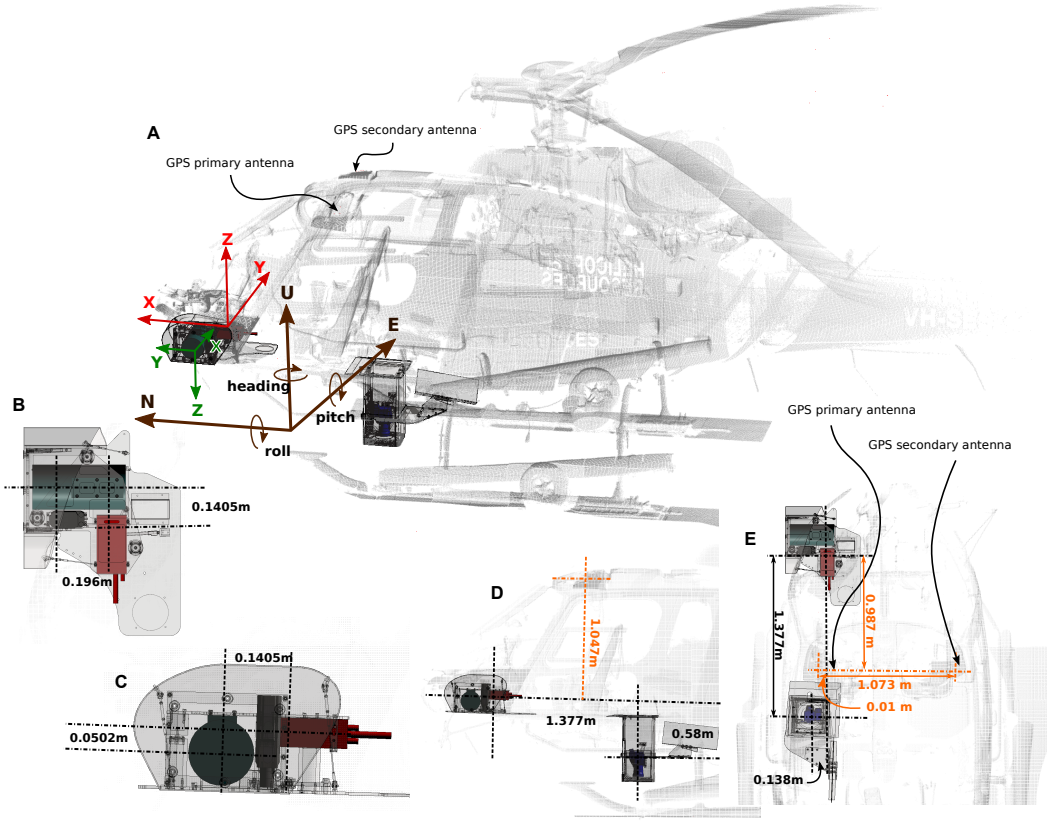

Figure 3.1: APPLS instrument layout and displacements. Red axes represent the Riegl LMS-Q240 coordinate system, green axes the OXTS RT-unit's coordinate system - equivalent to the aircraft body frame, and brown axes represent a mapping frame. Offsets are given in IMU frame coordinates, which approximates the aircraft body frame. Dimensions in orange show the offset between the GPS antennae and the RT-unit. Panel A shows an overview of all instruments in place. Moving counter-clockwise, panel B shows the horizontal offsets between the LiDAR and RT-unit. Vertical offsets are given in panel C. Panel D shows the vertical offsets between the LiDAR, RT-unit, GPS antennae and camera focal plane. Panel D shows the horizontal offsets for the same set of instruments.

In the aircraft body frame, The X-axis passes through the nose and tail of the aircraft (along the aircraft), and is positive to the aircraft nose. The Y-axis passes from one side door to the other (across the aircraft), and is positive to the right when facing in the direction of flight. The Z-axis passes vertically from the floor of the aircraft, approximately parallel to the main rotor shaft, and is positive upward. The LiDAR instrument and IMU are mounted on a single aluminium plate, aimed at providing a rigid relationship between the instruments. This plate is fixed to the helicopter floor by four shock mounts. As seen in Figure 3.1 the GPS antennae are mounted in specially modified skylight windows.

3.3 LiDAR point geolocation

The process for generating a LiDAR point cloud from APPLS is given in Figure 3.2. Processing the aircraft trajectory requires particular care in order to minimise the

	X	Y	Z
primary antenna → IMU	-0.987 (0.01)	-0.010 (0.01)	1.047 (0.01)
primary antenna → antenna 2	0.0 (0.01)	1.073 (0.01)	0.0 (0.01)
LiDAR → IMU	0.1405 (0.005)	-0.196 (0.005)	-0.050 (0.005)
IMU → camera 2007-2008	-1.377 (0.02)	0.138 (0.02)	-0.38 (0.02)
IMU → camera 2009-2012	-1.377 (0.02)	0.138 (0.02)	-0.58 (0.02)

Table 3.1: Displacement of APPLS instruments in the IMU frame (metres). Estimated measurement accuracy is given in brackets.

uncertainty in the position of the instrument payload. GPS observations are post-processed using GrafNav (http://www.novatel.com/products/software/grafnav/, accessed 12 May 2016) to minimise positioning uncertainty before they are combined with IMU observations using the OXTS-supplied 'RT post-process' (RTPP) software package (OXTS, 2011). A Kalman filter employing a loosely-coupled approach is used to merge IMU accelerations and velocities with GPS positions and velocities, to generate a trajectory from which LiDAR points are georeferenced. In this approach GPS positions, velocities and a GPS heading provided by the RT-units dual GPS provide initialisation parameters for a trajectory based on inertial observations. If the two data sources agree within certain parameters, uncertainty around the instrument position is tightened. Where sudden jumps in GPS trajectories occur, the Kalman filter adds an offset, or iteratively adjusts the trajectory to match new GPS positions. Section 3.7 provides a more detailed description of GPS and IMU combination strategies, and gives the parameters used for APPLS data processing.

The general model for georeferencing two-dimensional airborne laser scanner data is given by Equation 3.1 (e.g. Glennie, 2007; Schaer et al., 2007). Each term in the model is described in Table 3.2. The LiDAR instrument records only timestamps, ranges, return intensities and angles which describe the orientation of each range measurement in it's own coordinate system. These are used to compute 2D point coordinates of the LiDAR strike in the LiDAR instrument frame. LiDAR coordinates are then transformed into the IMU frame using the so-called boresight alignment angles (R_s^b) and the offsets which describe the relationship between the two coordinate systems (the lever arm, Table 3.1). Finally, LiDAR coordinates are transformed into the mapping frame using angular measurements from the IMU (heading, pitch and roll; R_b^m), and positions from the onboard GPS ($[X, Y, Z]$). The 3rd dimension for LiDAR measurements is provided by motion of the aircraft, nominally along the IMU/aircraft X axis for forward, level flight.

$$\begin{bmatrix} x \\ y \\ z \end{bmatrix}^m = \begin{bmatrix} X \\ Y \\ Z \end{bmatrix} + R_b^m \left[R_s^b \rho \begin{pmatrix} sin\Theta \\ 0 \\ cos\Theta \end{pmatrix} + \begin{bmatrix} a_x \\ a_y \\ a_z \end{bmatrix}^b \right] \tag{3.1}$$

The application of this system of equations for the APPLS package is the end point of a long processing chain (Figure 3.2). The first steps are extracting GPS observations

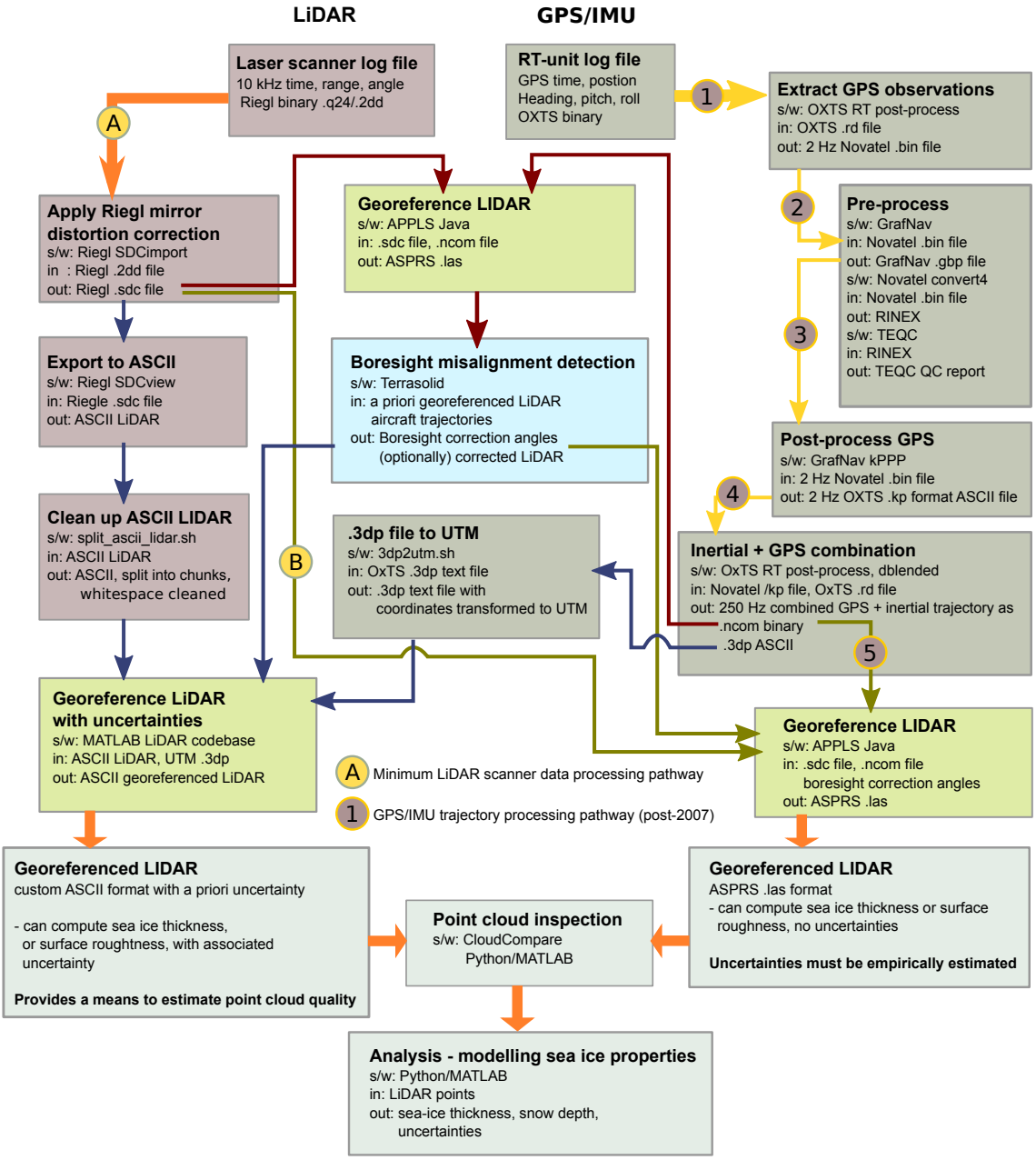

Figure 3.2: LiDAR processing flowchart. The left side shows LiDAR processing steps from data logged by the instrument to binary or ASCII output files which are readable for point cloud generation. The right side shows the pathway for trajectory processing using GPS and IMU observations. Blue arrows show the workflow used for generating ASCII point clouds with a priori uncertainty estimates, green arrows show the process for building .LAS format point clouds. Red arrows show the pathway for estimating boresight misalignment.

and post-processing to extract positions, then combining GPS and inertial data using the OXTS RT post-process application. Raw LiDAR observations from the LMS-q240i are extracted, and then georeferenced using a combined GPS + IMU trajectory, following the processes in Figure 3.2.

$\begin{bmatrix} x \\ y \\ z \end{bmatrix}^m$	is the three dimensional LiDAR point location in a mapping frame
$\begin{bmatrix} X \\ Y \\ Z \end{bmatrix}$	is the aircraft position in a mapping frame
R_m^b	is the rotation matrix between the IMU (aircraft body) frame and the mapping frame
R_s^b	is the rotation matrix which determines the orientation of the laser scanner with respect to the IMU (boresight matrix)
$\begin{bmatrix} sin\,(\Theta) \\ 0 \\ cos\,(\Theta) \end{bmatrix}$	is the laser point coordinate in laser scanner coordinates (2D), where Θ is the orientation of the LiDAR shot in the LiDAR reference frame
$\begin{bmatrix} a_x \\ a_y \\ a_z \end{bmatrix}^b$	is the lever arm offset between the IMU reference point and the LiDAR origin

Table 3.2: Components of Equation 3.1

	heading	**pitch**	**roll**
IMU	0.1°	0.03°	0.03°
	range	**angle encoder**	**beam divergence**
LiDAR	0.02 m	0.005°	0.154°

Table 3.3: Manufacturer instrument accuracy specifications

3.4 Propagation of uncertainties for APPLS LiDAR

Each component in Equation 3.1 has an associated uncertainty. Table 3.3 gives uncertainties provided by instrument manufacturers for system components. Beam divergence is included here because it is assumed generally that a LiDAR point return is collinear with the transmitted pulse. For the LMS-q240i, a beam divergence of 0.27 mRad (0.154°) gives a lidar footprint of approximately 1.08 m at 400 m range over flat terrain. Lichti and Gordon (2004) characterise the uncertainty of return position due to beam divergence as 1/4 of the total divergence, based on the distribution of power in a return signal. For the LMS-Q240i this brings uncertainty due to beam divergence down to 0.039°.

For the remaining parameters in Equation 3.1, uncertainties are determined during post-

processing of observations collected in flight. GPS positioning is an obvious contributor to LiDAR point uncertainty, with positioning uncertainty creating a noise floor for point cloud uncertainty - since additional measurement uncertainty dictates that a point position cannot be any more accurate that the a priori LiDAR instrument position. Following Glennie (2007) and Skaloud et al. (2010a), the variance-covariance matrix of LiDAR points from a two-dimensional airborne laser scanner using a GPS+IMU system for point geolocation is given as:

$$E_{xyz} = JCJ' \tag{3.2}$$

Where J is a 3 x 14 Jacobian matrix containing partial differential equations of the functional model (Equation 3.1) with respect to each of the parameters (Equation 3.3), and C is the covariance matrix of instrument uncertainties, assuming no correlation uncertainties between instrument types (Equation 3.4).

$$J = \left[\; F_{gps} \; \middle| \; F_{rpy} \; \middle| \; F_{bs} \; \middle| \; F_{angle} \; \middle| \; F_{range} \; \middle| \; F_{lever} \; \right] \tag{3.3}$$

$$C_{14x14} =_{diag} \left[\; \sigma^2_{gps} \; \middle| \; \sigma^2_{rpy} \; \middle| \; \sigma^2_{range} \; \middle| \; \sigma^2_{angle} \; \middle| \; \sigma^2_{boresight} \; \middle| \; \sigma^2_{lever} \; \right] \tag{3.4}$$

In practice aircraft position and attitude accuracies are determined as time dependent parameters when aircraft trajectories are computed, and the values given here reflect typical in-flight parameters. Laser beam divergence is not explicitly modelled here, but is added to the LiDAR instrument angular error term as one quarter of the beam divergence, following Glennie (2007). Figure 3.3 shows the expected uncertainty for a LiDAR point as a function of nadir range and scan angle using the a priori observational uncertainties given in Table 3.3, and a GPS positioning error of 0.1 m. This represents an idealised, or best case 'noise floor' to the accuracy of 3D points from the APPLS system for the given input uncertainties.

The sensitivity of LiDAR point uncertainty to input uncertainties in Equation 3.1 is shown in 3.4. Horizontal positioning uncertainty is most strongly influenced by angular uncertainty. Angular uncertainties overtake instrument positioning uncertainty as the dominant source of error as the observed range increases. Input position uncertainties remain constant with range.

Positioning uncertainty is the largest contributor to LiDAR point height uncertainty, but positioning uncertainty is largely insensitive to changes in range to target and likely dominated by the ability to resolve tropsheric path delay (King, 2009). As range to target

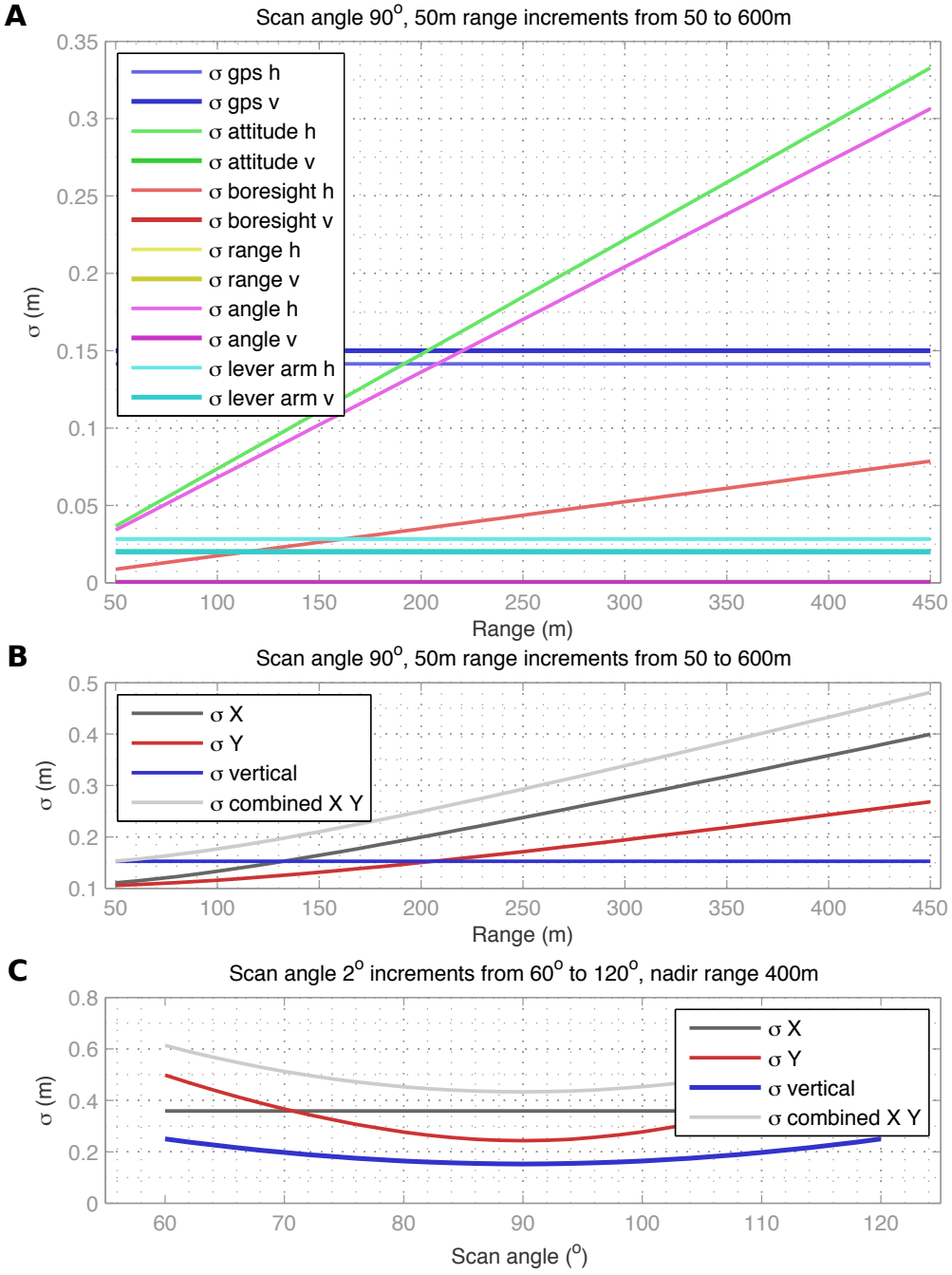

Figure 3.3: Idealised uncertainties (1-σ) of each parameter in Equation 3.1 with increasing range to target at instrument nadir (A), combined uncertainties in the X, Y and Z axes (relative to the aircraft/IMU system) with increasing range at instrument nadir (B), and combined uncertainties across-swath assuming a range to target of 400 m (C).

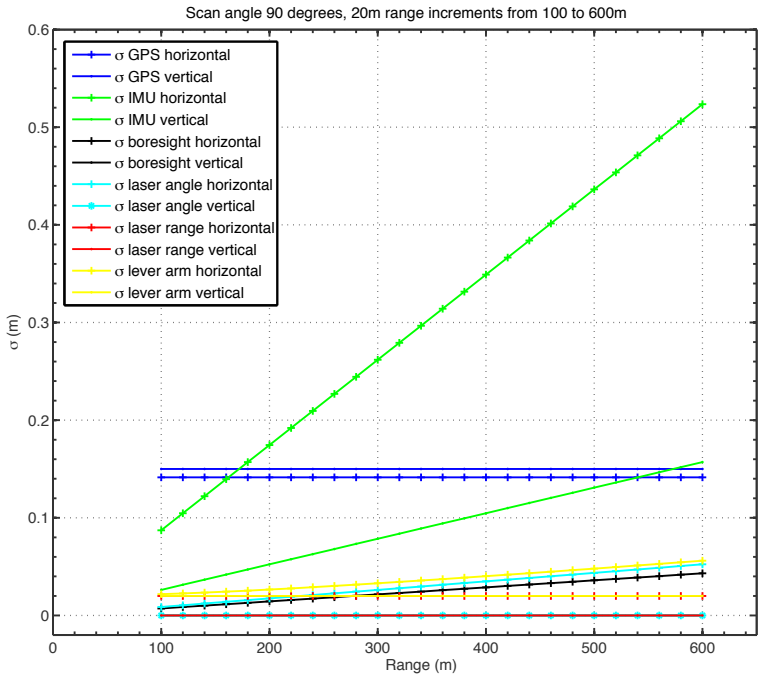

Figure 3.4: Sensitivity of LiDAR point uncertainty with respect to input uncertainties in the parameters for Equation 3.1

increases, minimising angular error becomes increasingly important at swath edges. With a relatively fixed set of angular uncertainties due to instrument choice, minimising the uncertainty in LiDAR point position for the APPLS instrument package is dependent on minimising uncertainties in aircraft position and attitude.

The LiDAR georefencing model (Equation 3.1) and the model for estimating the a priori uncertainty of LiDAR points (Equation 3.2) were implemented in a MATLAB package[1], which was used to produce LiDAR point clouds examined in this study.

3.5 Validation of modelled APPLS uncertainty

The impact of aircraft choice is first demonstrated by comparing observations from the same LiDAR instrument in a fixed wing aircraft. For initial testing, the APPLS LiDAR was deployed in a fixed wing aircraft operated by Airborne Research Australia (ARA). LiDAR observations were captured over low-lying rural regions north of Adelaide, South Australia. Figure 3.5a shows a short section of LiDAR, with a segment near the swath edge highlighted. Figure 3.5b shows the elevation of the highlighted segment, with a 1D spline fit overlaid as an estimate of mean topography. In Figure 3.5c, residuals from the spline fit are shown, predominantly falling within 0.15 m of the spline fit (1-σ 0.073 m). This aims

[1]https://github.com/adamsteer/LiDAR_georeference (accessed 10 May 2016)

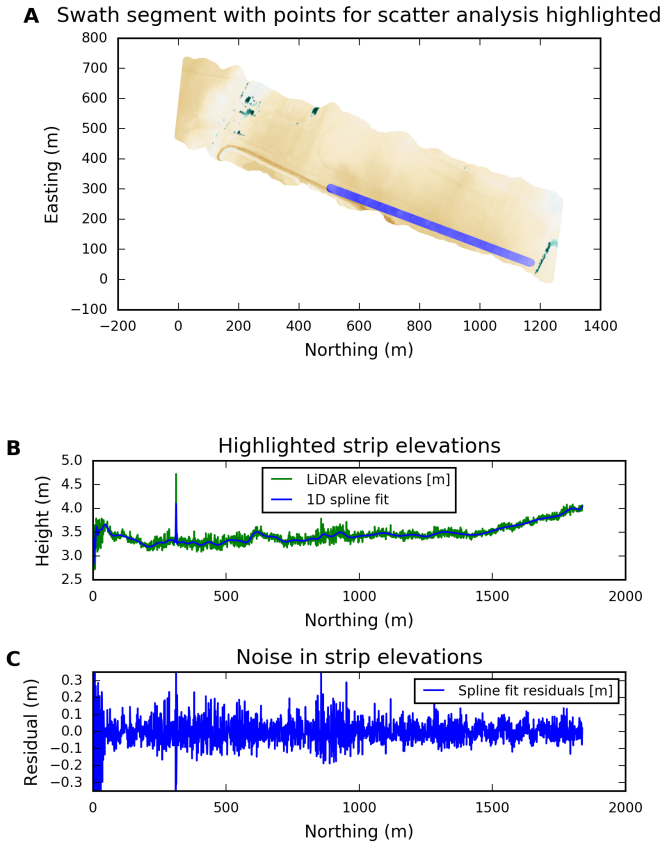

Figure 3.5: Swath edge detail from a calibration flight in 2007, north of Adelaide (South Australia). Panel A shows a LiDAR segment with a patch of edge points highlighted. Panel B shows the elevations for the highlighted patch (green), with a 1-D spline fit (blue) approximating underlying topography. Panel C shows residuals from the spline fit (1-σ 0.073 m). Eastings and Northings are shown relative to the bottom left corner of the swath bounding box in UTM coordinates

to imply the 'noise floor' for LiDAR observations, noting that some of component of these residuals will be from ground cover variability. This survey was also flown with an OxTS RT-3000 strapdown navigator, a less accurate instrument than the more recent RT-4003 used from 2008 to 2012 (including this study).

A similar set of observations was captured over Cambridge aerodrome (International Civil Aviation Organisation Airport Code: YCBG), Tasmania in 2010 and 2012 using the APPLS instrument package configured as shown in Figures 1.5 and 3.1. Figure 3.6 shows a segment of LiDAR next to the runway. The terrain here is gently undulating and has a short (10 cm) grass cover, with bare dirt patches. Following the methodology used for Figure 3.5, a 1D spline was fitted to a thin strip of elevations near the swath edge (RMS 0.12 m). For this flight, aircraft trajectory was processed relative to the nearby GPS reference station HOB2. This analysis suggests that the helicopter platform produces noisier LiDAR observations than a fixed-wing deployment which used lower-precision instruments for positioning the aircraft and georeferencing LiDAR points.

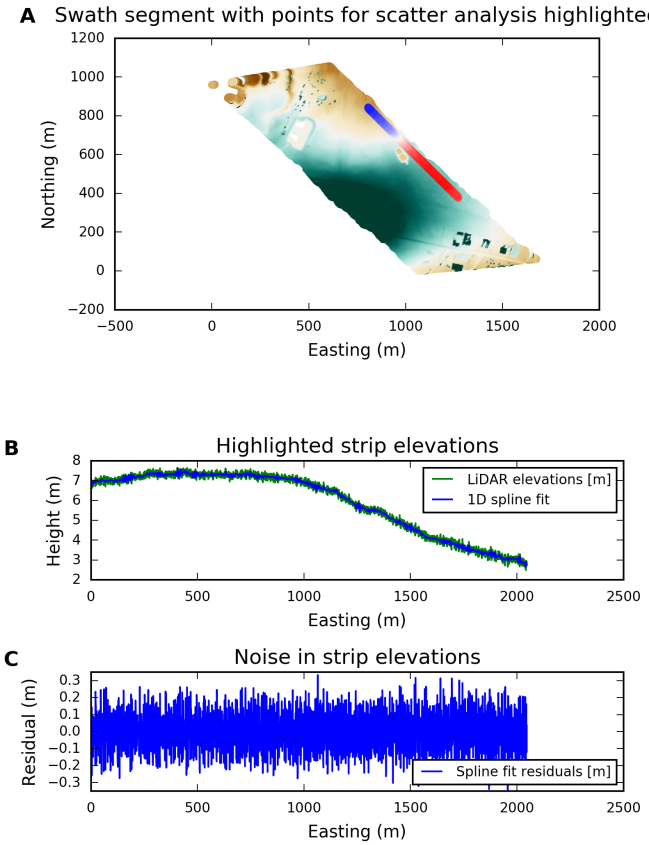

Figure 3.6: Swath edge detail from a calibration flight in 2012, over Cambridge aerodrome (Tasmania). Panel A shows a LiDAR segment with a patch of edge points highlighted. Panel B shows the elevations for the highlighted patch (green), with a 1-D spline fit (blue) approximating underlying topography. Panel C shows residuals from the spline fit (RMS 0.12 m). Eastings and Northings are shown relative to the bottom left corner of the swath bounding box in UTM coordinates

Following the same method and looking closer to instrument nadir, Figure 3.7 shows a segment from a 2010 testing and calibration flight over the University of Tasmania playing fields This swath shows three playing fields with separated by grassy ramps, visible as steep slopes between relatively flat surfaces. Each playing field surface is relatively smooth, characterised by elevation variations in the order of centimetres per metre. It shows that nadir looking LiDAR scatter is lower than for swath edges (RMS 0.074 m vs 0.12 m), which is predicted by the uncertainty modelling shown in Section 3.4. However, LiDAR point 'noise' in the centre of a swath obtained using a helicopter is greater than at the edges of the data acquired using a fixed wing aircraft. In the following section, the contribution of noise sources specific to the APPLS system is examined.

3.6 Uncertainties specific to APPLS

Section 3.4 provided the idealised case for the estimation of uncertainties in APPLS LiDAR data. In practice it remains important to determine if a prioriestimates are realistic, or if

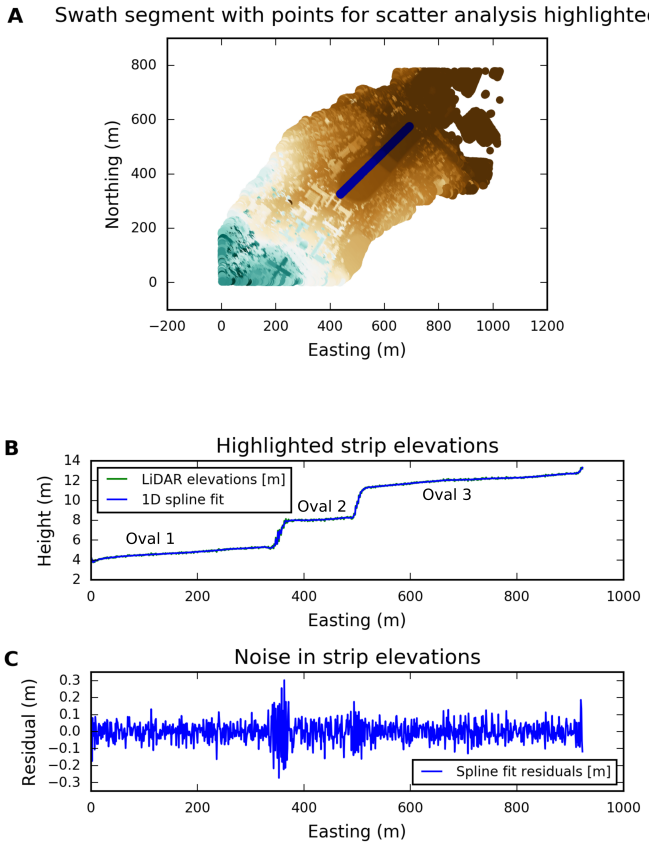

Figure 3.7: Swath edge detail from a calibration flight in 2010, over the University of Tasmania Sandy Bay campus, Hobart, Tasmania. Panel A shows a LiDAR segment with a patch of edge points highlighted. Panel B shows the elevations for the highlighted patch (green), with a 1-D spline fit (blue) approximating underlying topography. Panel C shows residuals from the spline fit (RMS0.074 m). Eastings and Northings are shown relative to the bottom left corner of the swath bounding box in UTM coordinates

there are additional systematic sources of uncertainty which need to be considered. For the APPLS instrument package, two areas of concern are GPS precision given the positioning of antennae beneath the rotor disc; and IMU precision given helicopter airframe vibration. These are primarily constrained by the instrument mount design, and hence are specific to APPLS. In this section, these uncertainties are quantified with observations from the test flight over Cambridge aerodrome and Hobart (Tamania) used in Section 3.5.

3.6.1 Helicopter rotors and impact on GPS performance

Previous studies investigating GPS performance for helicopters has indicated that helicopter rotors may act as diffusers for GPS signals (Brodin et al., 2005). The British Civil Aviation Authority investigated GPS signal attenuation from helicopter rotor blades and found that GPS signals were perturbed by the passage of rotor blades overhead. Despite this, there was no detectable increase in Coarse-Acquisition (C/A) pseudorange noise or signal availability when the main rotor was turning. C/A pseudorange positioning

was not degraded by using GPS antennae under the rotor disc (Brodin et al., 2005). However, the use of helicopters as a surveying platform dictates the use of carrier-phase observations (using the GPS signal wavelength to determine position) which were not assessed by Brodin et al. (2005)

Stebler (2008) found that the signal-to-noise ratio was reduced for GPS data acquired below a rotor disc, and developed a system for in-flight quality estimates based on GPS reception. Replicating a GPS signal quality measure is beyond the scope of this thesis; however, the impact of spinning rotors on positioning accuracy was investigated using two short experiments. To assess the impact of rotors on the APPLS GPS system, at the end of a test flight in 2010 the aircraft landed and rotors were left spinning for up to five minutes while the RT-unit collected GPS and inertial observations. The rotors were then turned off, and a further five minutes of observations were collected after the rotors came to a full stop.

Figure 3.8 shows a number of metrics obtained over the course of rotors stopping. At 25 seconds, the aircraft is landed and on the ground. At 170 seconds, power to the main shaft is cut off, and at 280 seconds the rotors have come to a stop. Z-axis (vertical) acceleration from the RT4003 is shown in dark green with Z-axis velocity in light green. L1 carrier phase (1575.42 mHz) RMS is shown in black. The blue line denotes estimated vertical accuracy, and the red line shows ellipsoidal height from a post-processed solution. As each of the datasets shown in Figure 3.8 are in different units and only a relative comparison is required, the y-axis is not labeled. The key point is to show the relative impact on signal quality when the helicopter is fully operational, compared to the same equipment in the absence of overhead rotor blades.

The IMU observations shown in Figure 3.8 show the expected increased motion (vibration) while the rotors are under power, reducing to a noise floor once the rotors stop. The height component of the GPS solution shows a slight reduction in the high frequency variability after the rotors stop, reducing from a standard deviation of 0.004 m to 0.003 m. Strikingly, the L1 carrier phase RMS is substantially reduced from approximately 0.08 m while rotors are running to approximately 0.04 m after the rotors stop. The uncertainty in the GPS height (blue line) is not sensitive to the rotor motion, suggesting that GrafNav's variance propagation is not fully considerate of systematic effects in the observations.

3.6.2 Helicopter airframe vibration

In the APPLS package, IMU and LiDAR instruments were connected to the helicopter airframe by shock mounts, which aimed to dampen vibration in a noisy helicopter environment. This strategy removed a range of high-frequency motion above 1.2 kHz (Morrissy, 2009). However, vibration below that threshold is transmitted to the IMU and LiDAR instruments. Figure 3.9 shows vibration frequencies recorded by the RT-unit's accelerometers. The dominant vibration frequency for the helicopter installation is

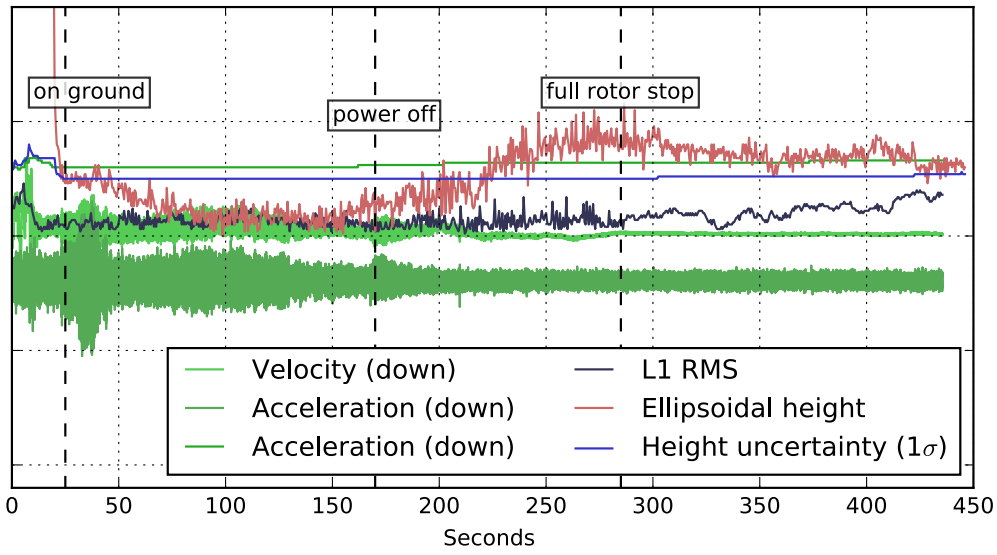

Figure 3.8: IMU and GPS observations during rotor shutdown. Green traces show IMU observations of vertical acceleration and velocity. The black trace shows L1 RMS (m) observed by the GPS receiver. Red shows ellipsoidal height (range approximately 5 cm after landing), and the blue trace shows the estimated height uncertainty. No y axis scale is shown, as the components of this plot all have different units and ranges. The key point is to show the relative impact on each in the presence and absence of rotor blades spinning overhead.

19.5 Hz, with harmonics at approximately 40, 60, 70 and 80 Hz. This makes physical sense as the nominal main rotor shaft speed of the aircraft is approximately 400 revolutions per minute, meaning that one of three rotor blades will pass over a given point in the airframe approximately 1200 times per minute, which translates to a frequency of 20 Hz.

The effects of vibration on the RT-unit were assessed by determining displacement and rotation of the IMU at frequencies above 10 Hz. At these frequencies the RT-unit was displaced 0.2 mm in the vertical axis, with an order of magnitude smaller displacements along its horizontal axes. Vibration above 10 Hz was responsible for a rotation of 0.04 degree about the IMU X and Y axes (corresponding to aircraft pitch and roll), and 0.005 degree about the IMU Z axis (corresponding to aircraft heading).

These observations show that the IMU is capturing rotor-induced vibration experienced by the APPLS instrument package. Critically, motion due to vibration survives the Kalman filter employed by RT post-process to combine GPS observations and inertial data (Figure 3.10), although higher frequency harmonics are slightly attenuated. In the APPLS package, the LiDAR and RT-unit were mounted on the same rigid plate. Capturing as much detail on the real motion of that plate, and by implication the LiDAR scanner head, is essential in accurately georeferencing LiDAR points since small movements at the LiDAR scanner head are encoded in the LiDAR range and angle signals.

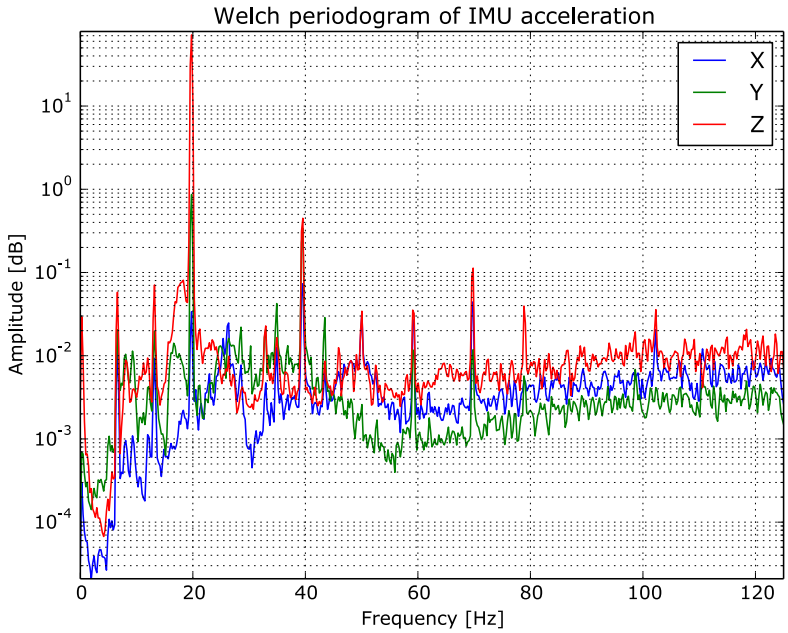

Figure 3.9: Welch periodogram of IMU accelerations along each axis.

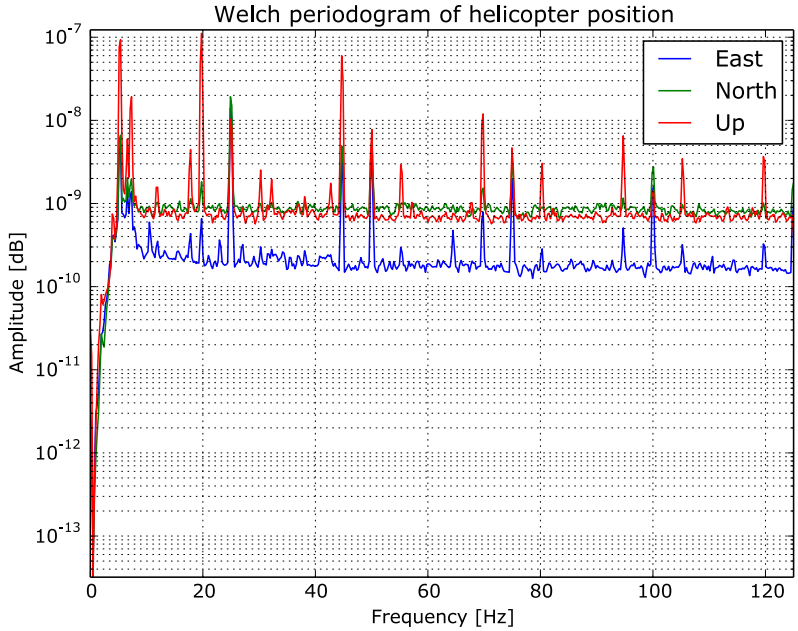

Figure 3.10: Welch periodogram showing relative power of signals above 5 Hz in geographic position (east, north, up) output from RT post-process.

3.7 Minimising positioning uncertainty for APPLS LiDAR

The use of GPS reprocessing strategies and combination of GPS and inertial observations to improve the accuracy of aircraft trajectories and resulting LiDAR observations is a standard procedure (e.g. Glennie et al., 2013; Kwok and Maksym, 2014; Schaer et al., 2007; Skaloud et al., 2010b; Shrestha et al., 2007). For the APPLS package the optimal strategy for positioning in the field was single-receiver kinematic Precise Point Positioning (kPPP), since the nearest fixed base stations were several hundred kilometres distant. While studies employing LiDAR over sea ice have used relative positioning strategies (e.g. Doble et al., 2011; Forsberg et al., 2002; Kwok and Maksym, 2014), these were able to obtain reliable estimates of GPS ambiguities by leaving from, and returning to, a terrestrial airport near GPS reference receivers. As King (2004) points out, relative positioning against land based reference sites will likely have significantly degraded precision when the separation distance is large, particularly because the atmospheric conditions between the aircraft and land reference sites are likely to be significantly decorrelated. Even with the ability to fix ambiguities prior to long flights over sea ice, Forsberg et al. (2002) report uncertainties in the range of decimetres for aircraft positioning at baselines of hundreds of kilometres, a range which is achievable using a kPPP strategy (e.g. Castleden, 2004; Geng et al., 2010). Others (e.g. Doble et al., 2011; Kwok and Maksym, 2014) do not report the accuracy of airborne trajectories at all.

Novatel's GrafNav software was used to process APPLS trajectories using a kPPP approach. Figure 3.11 shows results from two GPS post-processing strategies for the Hobart test flight used in Section 3.5. A flight map coloured by height uncertainty (Figure 3.11a) shows that higher positioning uncertainties are associated with dynamic flight segments (notable in tight turns likely associated with loss of lock of signals from one or more satellites). The plot of height uncertainties from kPPP and relative baseline positioning (Figure 3.11b) show that for this case, the uncertainty surrounding aircraft position using relative baseline position is clearly lower than for a kPPP strategy. However, GPS reprocessing is only the first step in developing a trajectory for use in georeferencing airborne LiDAR. GPS observations must be combined with inertial observations to capture aircraft attitude, and as Figure 3.11b shows, using a combined GPS + IMU strategy for processing the trajectory results in a reduction of the aircraft positional uncertainty.

3.7.1 Combining GPS and inertial observations

The RT-unit instrument deployed in the APPLS package contains accelerometers which measure acceleration and rotation rate over three axes as 250 Hz.The resolution of these observations is given in Table 3.3. In post-processing, a GPS trajectory including positions, position uncertainties and Doppler velocities is combined with inertial observations using a Kalman filter (Kalman, 1960) implemented in the OXTS software package 'RT Post-process' (RTPP). For the APPLS system, the trajectory merging is performed in a loosely-coupled process (shown in Figure 3.12, adapted from Yi (2007)). Here, GPS positions and

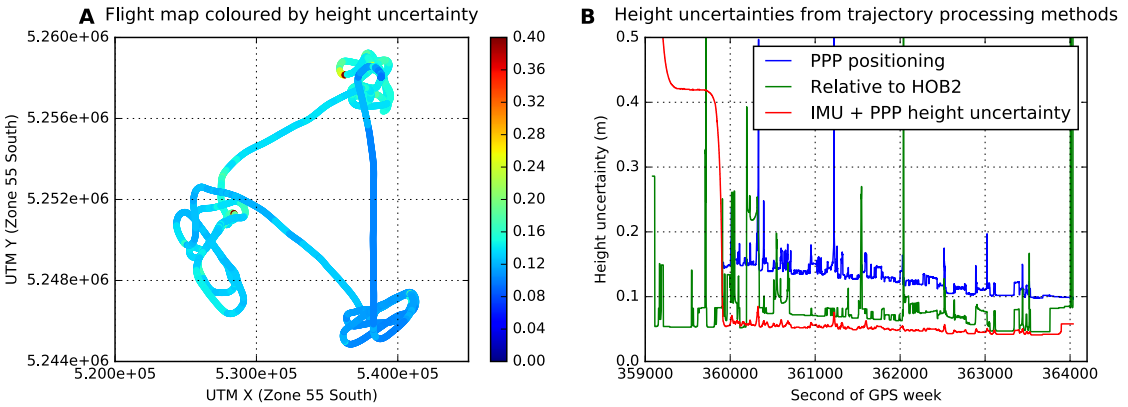

Figure 3.11: Comparison of height uncertainties from processing methods for APPLS trajectories, using relative baseline positioning, kPPP and kPPP + inertial observations

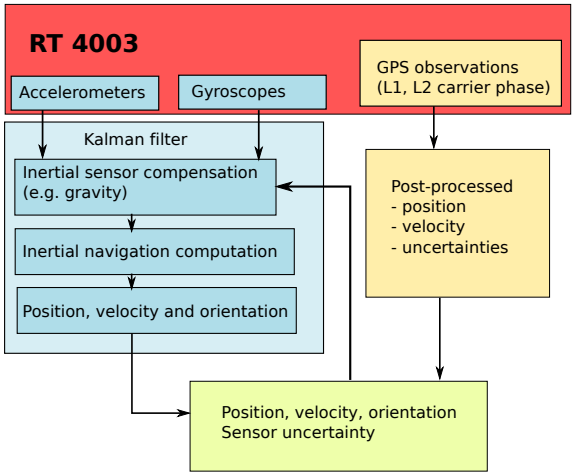

Figure 3.12: Block diagram showing an overview of loosely-coupled merging of IMU and GPS observations. Adapted from Yi (2007)

aircraft heading from the RT-unit's two GPS receivers are used to provide an a priori position and orientation, which is updated using both GPS and inertial observations at each epoch. As well as acting to fill in the gaps between a 1 Hz to 2 Hz GPS time series and a 250 Hz inertial observation time series, the inertial observations are used to iteratively constrain the uncertainty surrounding the instrument position, with the result that final positioning uncertainty is a function of inertial observation uncertainty and GPS uncertainty. Details of the principles of inertial navigation and combination with GPS observations can be found in Yi (2007), and Stebler (2008).

The technical report 'RT post-process cookbook' (Steer, 2015) describes how the Kalman filter was configured for APPLS projects. RTPP could be configured to assign higher confidence to either GPS or inertial observations depending on the scenario. For APPLS, given the vibration and likely increased noise in the GPS trajectory associated with the rotor disk interference, a high confidence was placed on all inertial measurements. In the APPLS environment the strategy was to capture as much system motion as possible, so it

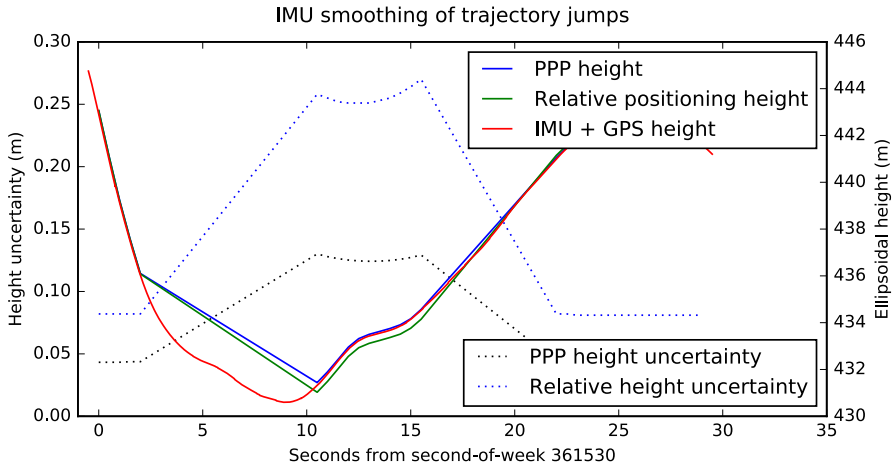

Figure 3.13: Using GPS + IMU to avoid trajectory jumps. The green and blue lines show GPS heights for a short segment of an APPLS flight, with a jump in position between 2.5 and 10 seconds. The red line shows the result of GPS + IMU processing, which uses inertial observations to track aircraft motion between GPS epochs, and for short outages.

could be accounted for during LiDAR processing. As such all filtering (smoothing) options were switched off. Finally, unexpected GPS measurements were discarded in preference to integrating inertial measurements to maintain trajectory stability through loss of lock events (e.g. during turns). This is demonstrated in Figure 3.13. Here, there is an apparent loss of signal for 7.0 seconds between 2.5 and 10 seconds where the GPS height jumps almost 5 m, but the motion of the aircraft is captured by inertial observations. Without inertial observations to fill in these gaps, LiDAR processed using the GPS trajectory alone would reflect the height step and produce erroneous topography.

3.7.2 Correcting for boresight misalignment

In the APPLS package, the instrument installation was designed to be orthogonal. In practice, this can , but in practice this can vary due to temperature, or small differences in reassembling the instrument package. Given the range between the instrument package and the ground based target, small alignment errors at the instrument translate into substantial variability in the system's data products. These are the so-called 'boresight misalignments', which must be estimated a posteriori using LiDAR swaths and imagery generated by the system. 'Calibration flights', or data collection specifically for assessing instrument misalignment, are commonly used to rectify any installation errors and determine lever arms and boresight misalignment (Shrestha et al., 2007). In general, data are collected over a set of well-known or easily identifiable target points (e.g. airfields) in different directions and preferably at different heights (e. g. Rost and Grierson, 2008). Instrument misalignment will express as a mismatch between repeated swaths flown in different directions (and optimally different heights), or repeat imagery, over the same area.

Test flights undertaken in 2010 and 2012 provide suitable data for estimation of boresight

	heading	pitch	roll
2010	0.0272°	0.0035°	0.0043°
2012	0.2058°	0.1117°	0.0189°

Table 3.4: Boresight misalignment correction values for the APPLS LiDAR and IMU

misalignment for the APPLS LiDAR, with the 2012 flight also providing sufficient image overlap to examine camera boresight misalignment. These are described in the technical reports Steer (2013) and Steer (2014). Boresight misalignment for the LiDAR instrument was estimated using the Terrasolid software suite (http://terrasolid.net). Terrasolid employs two strategies - the first is detecting the offset between LiDAR strips and computing corrections based on translation and rotation between overlapping swaths (Burman, 2000). The second approach is to detect linear features ('tie lines') in overlapping LiDAR swaths, and minimise the angle and distance between them (Rost and Grierson, 2008). Boresight misalignment is taken as the set of angles by which the LiDAR $\rightarrow$ IMU relationship needs to be altered in order to minimise the angular offset between overlapping flight lines.

The second approach was used for APPLS flights, with the derived values given in Table 3.4. No uncertainties were provided by the processing software using this method. Published correction uncertainties of 0.001° for pitch and roll, and 0.004° (Glennie, 2007) for heading were applied for uncertainty analyses and LiDAR processing for this thesis.

While small, the technical reports Steer (2013) and Steer (2014) show that applying these corrections results in substantial improvement in LiDAR swath alignment. In practice, these figures may change between a test flight and deployment in the field due to temperature changes, and removal/reinstallation of instruments. For APPLS missions over drifting pack ice, it was not possible to determine a boresight misalignment for each flight so the values in Table 3.4 were used as an a priori estimate.

3.8 Visualising uncertainties for LiDAR points

The work of Schaer et al. (2007) provides the basis for a next step - visualising the 3D error for each LiDAR point. The functional model in Equation 3.1 generates a 3D position for each point, and the uncertainty model in Equation 3.4 allows the computation of uncertainty at each point. During LiDAR processing, each XYZ point is given a 3D uncertainty value based on combination of the East, North and Up uncertainties provided by Equation 3.2.

Figure 3.14 shows a point uncertainty map from APPLS over the UTAS oval, also used for Figure 3.7. Here, the theoretical uncertainty of ± 0.05 m for point elevations near swath nadir is slightly optimistic. Using the same flight, Figure 3.7 showed that scatter near nadir was approximately ± 0.074 m. However - the estimation of a priori point

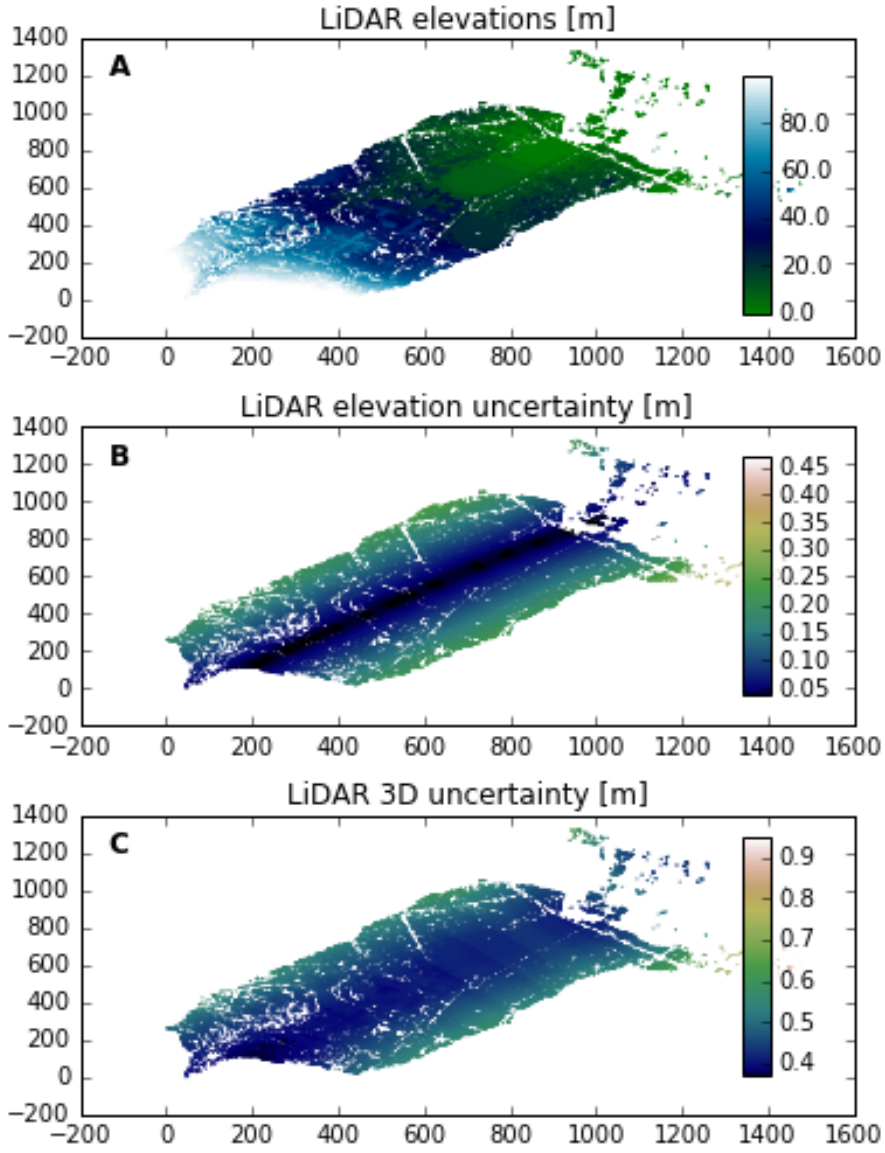

Figure 3.14: Uncertainty estimates computed using Equation 3.2 for APPLS during a calibration flight over the University of Tasmania playing fields. Panel A shows heights relative to the lowest point in the dataset, Panel B shows the vertical component of point uncertainty, Panel C shows the combined 3D uncertainty for point positions.

positioning uncertainty does not take into account noise which is not modelled by the aircraft instruments. For this flight segment, a relative posuitioning strategy was employed using the nearby HOB2 reference receiver, andGPS height uncertainty was in the order of 0.05 m prior to combining with IMU observations

Comparison with uncertainty from a field site shows how the quality of trajectory determination affects the uncertainty associated with each LiDAR shot. Figure 3.15 shows a similar map for a field site on the SIPEX-II voyage, which was positioned using kPPP with a GPS height uncertainty in the order of 0.15 m. Correspondingly, estimated point

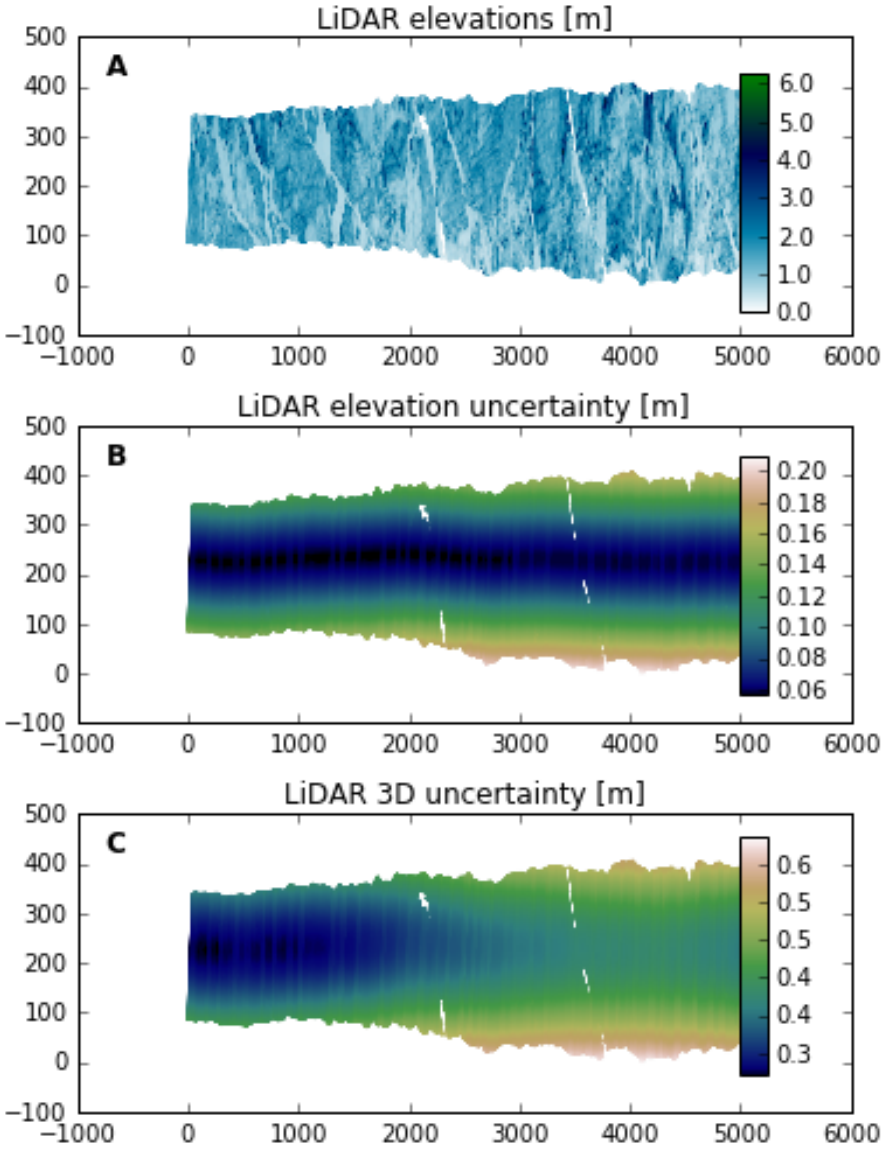

Figure 3.15: Uncertainty estimates computed using Equation 3.2 for APPLS LiDAR points over Antarctic pack ice during the SIPEX-II voyage (Flight 11, 13 October 2012). Panels as for Figure 3.14

elevation uncertainty (Figure 3.15b) is slightly higher (±0.06 m at nadir) than for the UTAS oval test site. The dependence of point uncertainty on angular uncertainty as the aircraft-to-target distance increases is shown clearly in Figure 3.15b and c. From left to right, LiDAR ranges increase, and in Figure 3.15b, elevation uncertainties become greater at swath edges. Looking at 3D point uncertainty, Figure 3.15c shows clearly that uncertainties increase as range to target increases. This is primarily a function of angular uncertainty, since absolute positioning and LiDAR ranging uncertainties are essentially constant over the swath shown here.

These maps show that the expected uncertainty range for APPLS elevations are in the

order 1 to 4 decimetres, with uncertainties increasing toward swath edges. The dependence on scan angle is particularly clear for the vertical uncertainty component. Given that the response of the Kalman filter used to blend GPS and inertial observations is to increase angular uncertainties in high vibration environments, prioritising the reduction of vibration in any future deployments would reduce the uncertainty surrounding points at swath edges. Further, the expected uncertainty is optimistic, as it does not account for unexpected vibration.

3.9 Discussion

3.9.1 Realistic uncertainty expectations for APPLS over sea ice

The work presented here shows that the APPLS system is able to achieve close to its theoretical 'noise floor' when deployed in a rotary-wing aircraft. However, the system has residual vibration-induced noise that is difficult to fully characterise and attenuate in post-processing. When deployed in the presence of additional vibration, any unmodelled vibration will be expressed as noise in the resultant point cloud. The need to mount GPS antennae below the rotor disc incurs additional uncertainty in aircraft position. During level testing, the effect of rotors overhead was minimal, but there was a clear increase in carrier phase noise. The noisy GPS environment is a likely contributor to difficulty in maintaining satellite lock, particularly during aircraft turns. In turn this likely impacts the ability to accurately position the aircraft, especially using kPPP methods. With these factors in mind, the current store of APPLS LiDAR points should be considered accurate to the order of 1 decimetre range at nadir, and 3-5 decimetres at swath edge.

3.9.2 Implications for sea ice thickness estimation

The uncertainty inherent in LiDAR elevation measurements has a direct impact on the uncertainty of sea ice thickness derived from airborne LiDAR using the model discussed in Chapter 2. In Figure 2.4 we see that each 0.1 m of uncertainty in sea ice elevation propagates through Equation 2.12 to snow thickness as $\sigma Z_s = Slope * \sigma F$, and then through Equation 1.1 to approximately 0.3 m of uncertainty in the thickness of sea ice. To keep within a reasonable uncertainty boundary - e.g. 0.5 m of ice thickness, uncertainty in elevation estimation must fall below 0.1 m, a challenging task for helicopter-borne instrumentation. The noisy nature of APPLS data presents an additional challenge, with detail obscured due to unmodelled instrument vibration.

The scatter present in the LiDAR point cloud (reflecting the uncertainty estimates presented throughout this chapter) influences the method used to determine a reference surface from which thickness may be derived. Where scatter about this surface exists (as for UTAS oval, Figure 3.7), the optimal strategy is to use the central tendency of the scattered points as the reference surface, and drop any points which fall below the surface

from further analysis. The cost of doing so is a reduced dataset, and the expense of keeping all points (for example, placing the reference surface at the lowest point) is overestimating sea-ice thickness. This method is implemented in Chapter 4, which employs the LiDAR processing steps shown in this chapter to derive and validate sea-ice thickness estimates. Taking the findings of this study into account for future iterations of the instrument package will improve the quality of ice properties derived from APPLS observations.

3.10 Conclusion

The APPLS instrumentation deployed in a rotary-wing aircraft was subject to greater systematic noise than than when tested in a fixed wing aircraft. However, the data collected are capable of delivering geophysical results if the uncertainties in the data are adequately understood. In this chapter, systematic uncertainties are exposed, and the means for estimating the impact of those uncertainties on geophysical results are presented. For the existing set APPLS LiDAR observations, this study developed methods which allows analysts to determine an acceptable boundary for point uncertainty and select appropriate data from the APPLS system for further analysis. It also enables a rigorous estimation of uncertainties in products derived from APPLS LiDAR.

The instrument installation described here is no longer in use, and future deployments will use an improved installation. For future development, measures to mitigate avoidable noise sources may include removal of the LiDAR system from a hard mount to the airframe (e.g. to use a towed pod deployment) and removing the instrument package from a position where GPS antennae are under a helicopter's rotor disc.

Well known strategies for minimising uncertainties that may arise during deployment should also be employed. Sharp turns during flight have had a severe impact on the system positioning quality, and should be avoided. Calibration flights every deployment to collect ISO boresight misalignment information are impractical for drifting sea ice. However, these parameters should be estimated prior to departure for a field season, and assessed for change over the course of a field deployment. These technical issues are not unique to APPLS, and following a rigorous survey method (e.g. Shrestha et al., 2007; Slatton et al., 2007) alongside instrument mounting modifications will assist further in generating high quality observations. Finally, post-processing strategies might include the use of tightly-coupled systems for combining IMU and GPS observations, where raw GPS carrier phase, doppler and pseudeorange observations are integrated with inertial observations to tightly constrain possible solutions for the GPS trajectory (e.g. Stebler, 2008; Yi, 2007)

In the Antarctic pack ice zone, logistics, personnel resources in the field and weather all conspire to make airborne surveying a challenging operation. Where ideal flight conditions cannot be met, this study provides some insight into how the quality of resulting data can be assessed. The insights gained in this chapter are applied in Chapter 4, which undertakes the estimation of sea-ice thickness from airborne LiDAR.

Chapter 4 High resolution estimates of East Antarctic sea-ice thickness from airborne LiDAR

4.1 Introduction

The previous chapters addressed the motivation and key prerequisites for attempting to estimate sea-ice thickness using high resolution airborne LiDAR. Understanding how to estimate snow depth in order to derive a sea-ice thickness model (Chapter 2), and understanding the sources of uncertainties in sea-ice thickness estimates (Chapter 3) are essential building blocks.

This chapter presents estimates of sea-ice thickness using the AAD's APPLS system over East Antarctic sea ice with a detailed study of ice station 6 (IS6) from the SIPEX-II field campaign (2012), where an autonomous underwater vehicle (AUV) collected coincident observations of ice draft using an upward looking multibeam sonar (Williams et al., 2014b,a,c). This allows a direct comparison of surface and under-ice topography in three dimensions, albeit over a very small region of Antarctic pack ice. Observations from SIPEX-II have been published independently (Lieser et al., 2013; Williams et al., 2014b), however this is the first attempt to integrate airborne, under-ice and on-ice observations from the SIPEX-II voyage.

A key issue for sea-ice thickness estimation from altimetry is the determination of a reference surface from which to measure total ice+snow freeboard. A generalised approach to this problem is to select the lowest points in a set of LiDAR elevations over some length, and derive a fitting plane or curve from those points to define an instantaneous 'sea level' reference surface (Dalå et al., 2005; Doble et al., 2011; Hvidegaard and Forsberg, 2002; Kurtz et al., 2013; Wang et al., 2013). This study takes a similar approach, seeking to fit a surface to points which fall on water or very thin ice and use the fitted surface model to 'level' LiDAR elevations such that returns from water have a mean elevation near zero. Doing so removes the need to compute geoid heights, tide models and dynamic sea surface topography for each LiDAR swath. Kurtz et al. (2013) and Onana et al. (2013) use an automated lead detection algorithm for aerial photographs to determine where LiDAR points lie on water or thin ice. This study derives a reference surface using only LiDAR as input data, but validates the point selection using coincident aerial photography. From altimetry datasets, snow depth and ice thickness are estimated using the methods detailed in Chapter 2. Using coincident AUV draft observations, this study will investigate the

input parameters required for sea-ice drafts modelled using Equation 1.1 to match the observed ice drafts.

The small-scale topography of the ice/ocean interface plays an important role in turbulent heat flux to the underside of sea ice (Skyllingstad et al., 2003), and larger features (e.g. ridge keels) are important modifiers of momentum exchange between the ocean and ice. Given that under ice roughness has implications for the transfer of heat and momentum between the sea ice and underlying ocean (e.g. McPhee, 2002; Skyllingstad et al., 2003), it is important to understand where, and how, the ice/ocean interface generated from altimetry differs from the in situ ice/ocean interface. When sea-ice thickness estimates are averaged over hundreds of metres (e.g. Cryosat-2, ICESat), topography on the scale of a single ridge or floe is essentially smoothed and these interactions must be derived from empirical models. As instrument resolutions increase (e.g. IceBridge, and the proposed ICESat-2) and the ice/ocean interface is modelled at higher resolutions, it is increasingly important to point out differences between the modelled surface and the actual ice/ocean interface to avoid erroneous assumptions about dynamic and thermodynamic ice/ocean interaction.

In the Arctic, Doble et al. (2011) used coincident LiDAR, AUV draft observations and field data to investigate the relationship between total freeboard and ice draft. They used a single snow depth for all observations, and a representative ice density to investigate the ratio R - which is a scalar multiplier for converting total freeboard into ice draft. Given that the analysis in Chapter 2 found the relationship between total freeboard and ice draft very weak, this question is revisited using the coincident LiDAR and AUV observations from SIPEX-II. In this study the utility of the ratio R is examined using coincident LiDAR elevations and AUV drafts for IS6, for all observations and for subsets of rough and smooth ice. Critically in this study, LiDAR elevations are used to segment observations into 'deformed' and 'undeformed' subsets, rather than using ice draft.

Extending the detailed study of IS6, a second case study makes a qualitative comparison of ice thickness estimated from LiDAR and from ship-based observations following the ASPeCt protocol (Worby et al., 2008b), over approximately 100 km of sea ice where an APPLS flight was aligned with the ship's track over subsequent days of travel through the ice. It is unrealistic to make a rigorous direct comparison, since sea ice sampled by the APPLS flight will have drifted out of the region at the time of the ship-based observation. However, both LiDAR and ASPeCt observations sample a similar ice regime.

A description of the methods used to derive sea-ice parameters from APPLS LiDAR and imagery follows. The chapter then proceeds to a case study using SIPEX-II ice station 6 (IS6), which is used to validate the methods employed to obtain total freeboard and then model sea-ice thickness from LiDAR. It is also used to examine the relationship between surface and under-ice topography, at a whole-floe scale and then under ice which is classified as rough or smooth using surface topography. The findings here are applied to a larger-scale analysis of LiDAR-derived ice thickness alongside ship-based ASPeCt

observations. Finally, an opportunistic application of Structure-from-Motion techniques for modelling terrain from overlapping photographs is discussed with respect to drill hole, AUV and LiDAR observations over IS6.

4.2 Data description and methods

4.2.1 Study region and flight selection

The SIPEX-II voyage made a transit of east Antarctic pack ice from north to south along approximately 120° E, encountering very thick ice at the southern end of the voyage and drifting more or less with the ice pack for close to a month. Eight 'ice stations' were deployed during the voyage, at which a number of observations were made below, on and above the sea ice. For this study, LiDAR and imagery from the APPLS system is used (Lieser et al., 2014), along with in situ drill hole observations (Heil, 2014) and sea-ice draft observations collected by AUV (Williams et al., 2014c).

At the sixth ice station (IS6, 12-14 October 2012) the largest set of AUV observations was collected (Floe 10 in Williams et al. (2014b), Figure 2), covering a region just over 300 m × 300 m beneath the ice station. This gives enough coverage to compare with coincident LiDAR, sampled with a swath width approaching 300 m. A 100 m transect was used for in situ drill hole observations, which are used as a reference for airborne and AUV observations of total freeboard and draft, respectively. Figure 4.1 shows a regional map of SIPEX-II ice stations and survey flights used in this analysis, and Figure 4.2 shows a detailed map of IS6. Over the three days the station was occupied, the ice floe drifted slowly eastward from 119.94° E 65.3° S to 120.04° E 65.3° S

Extending methods from the detailed study of IS6 to a broader scale, RSV Aurora Australis followed the southern flight line of APPLS Flight 22 for approximately 100 km between 1 and 3 days after the flight was undertaken. On this transit through the ice, regular ice thickness observations following the ASPeCt protocol were recorded on the ship. While it is unlikely that the ship-based observers saw the same ice flown over on Flight 22, the two sets of observations are close enough in space and time to make a preliminary comparison of LiDAR-derived ice conditions and ice thickness estimates obtained using the ASPeCt protocol. Further, it provides an opportunity to test the methods developed here on larger datasets, with a view to deriving sea-ice parameters from all existing APPLS data.

4.3 Obtaining a reference surface for LiDAR measurements of total freeboard

Over the Antarctic pack ice zone, it is impractical to establish 'ground truth' points to determine a sea surface height from which total freeboard can be measured using airborne LiDAR. Approaches to this problem have generally involved a mixture of modelling

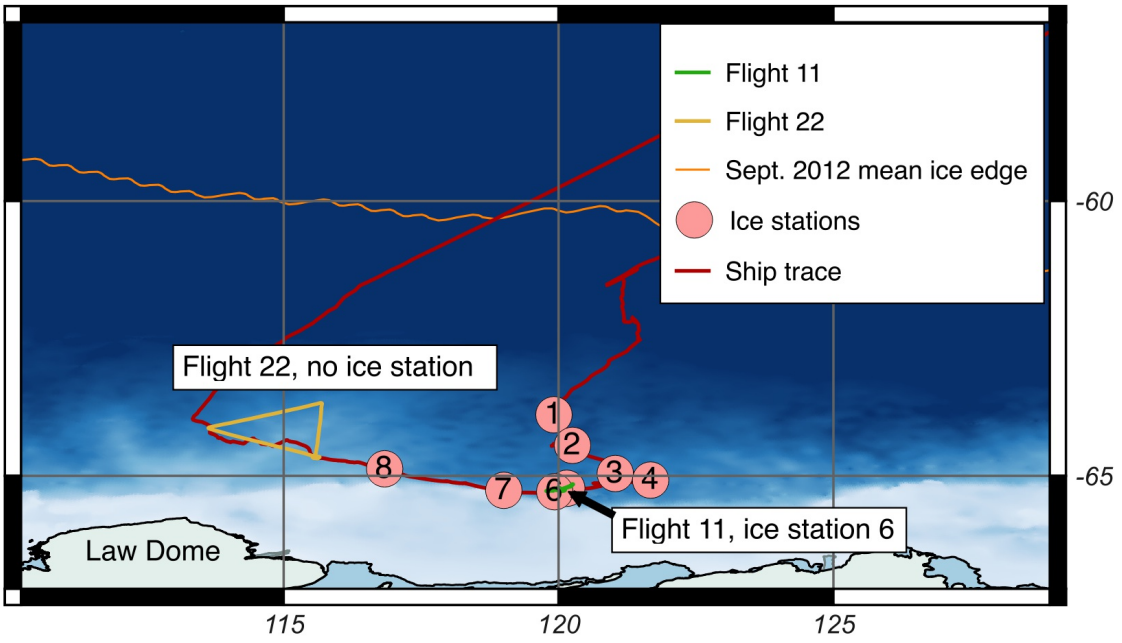

Figure 4.1: SIPEX-II ice stations and flights used in this study. Flight 11 is a short local flight centred on ice station 6, Flight 22 is a long survey flight, with the southern leg approximating the ship's route.

geoid surfaces and tides, and then subtracting heights from those models from altimeter observations - which potentially introduce additional uncertainty into derived heights and cannot account for swell penetration (e.g. Worby et al., 2011). In this work, water surfaces are derived from the LiDAR observations without additional geophysical inputs using an automated process (e.g. Wang et al., 2013).

The key prerequisites for this approach is the presence of leads spaced in the order of hundreds of metres along-track, ideally containing very thin grease ice. The APPLS LiDAR operates in the near-infrared spectrum, and is generally absorbed by water rather than reflected. Over open water, returns are only recorded within a few degrees of instrument nadir. Where grease ice is present, returns are recorded across the entire swath. Returns over water and thin ice can generally discriminated by return intensity, which is invariant to ambient illumination. However, low-intensity returns may occur at swath edges or over wet snow, so return intensity alone is not a sufficient discriminator of ice and leads. Where they do occur on ice, low intensity returns are generally isolated. In this study a neighbourhood size filter is applied to low-intensity points to remove isolated returns. A height filter is not applied because the noisy elevation signal means that low-elevation ice is difficult to isolate from open water by height alone.

Coincident imagery has been used to help select reference points (Kurtz et al., 2013; Wang et al., 2013) for determining an ocean surface and then a total freeboard from LiDAR. In this study, imagery is used to assist in manual validation of reference points derived from analysis of LiDAR return signals.

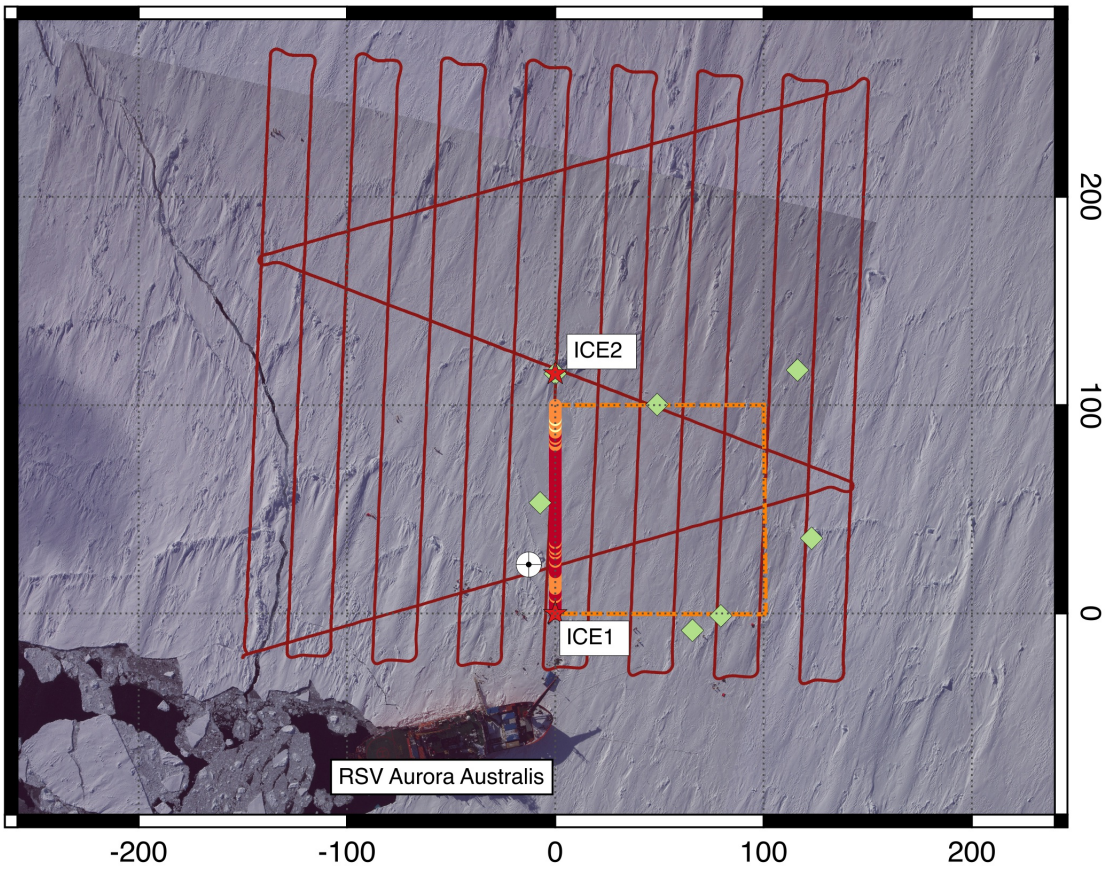

Figure 4.2: SIPEX-II Ice station 6. Red lines indicated AUV tracks under the ice, the orange dashed line indicates an intensively sampled 'survey plot', with dots along the axis y=0 indicating the 100 m drill hole transect. Red stars indicate the baseline GPS sites (ICE1 at origin, ICE2 marking false north). The crosshair shows the site of the total station (TRS). Green diamonds mark distributed drill holes around the survey plot. Ice thickness observations were also taken under ICE2 and the total station.

4.3.1 Extracting sea surface reference points from airborne LiDAR

To extract LiDAR returns from water or very thin sea ice, a two-stage filter is applied to the point cloud. The first stage in the filter is to detect the lowest Nth percentile of intensity returns, which collects most returns from water and thin ice, with a few returns from the sea-ice surface. Since these are isolated, points which survive an intensity low pass filter are then passed to a neighbourhood size filter. For each LiDAR point, neighbouring points within a user-defined radius r are collected. If there are fewer than $r \times 3$ points in the neighbourhood the point is discarded. For the APPLS system, the lowest 2% of intensity values are kept, and the neighbourhood width is set to a radius of 20 m, meaning a low-intensity point must have 60 neighbours which pass the intensity filter to be considered viable for use in estimating an 'instantaneous sea surface'.

The median elevation is computed for remaining neighbourhoods, and the 10 points whose elevation is closest to the neighbourhood median are selected for the reference point set.

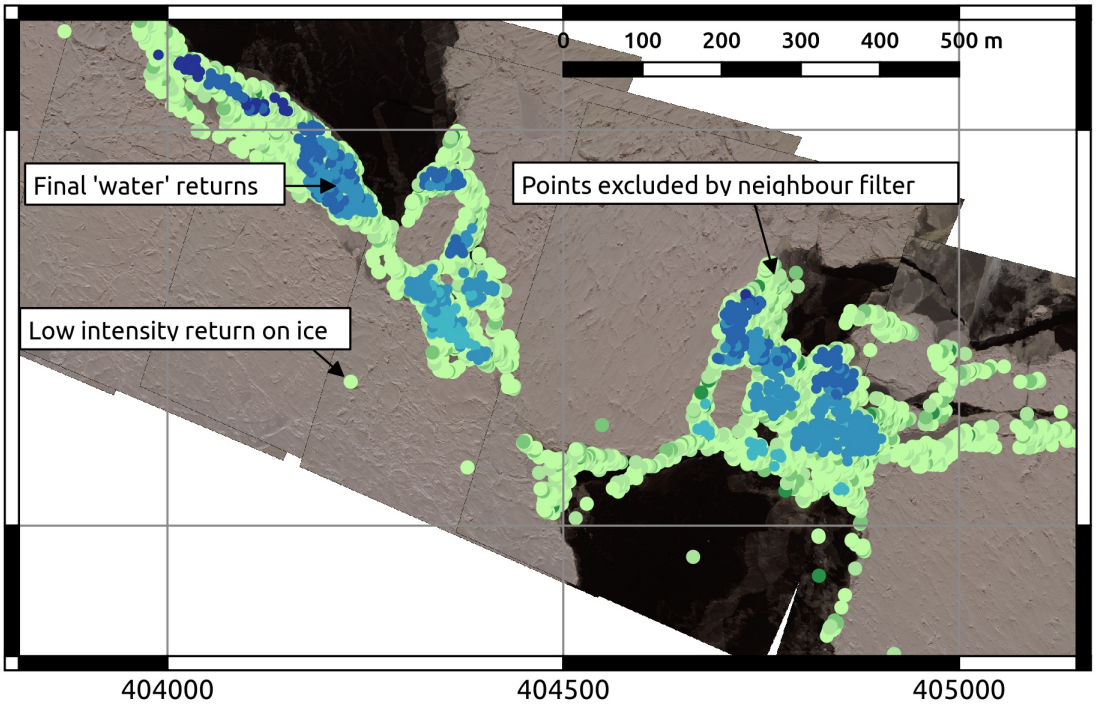

Figure 4.3: Results of filtering for elevation and a minimum points-in-neighbourhood threshold for low intensity returns. Green points are returned by an intensity low pass filter. Since isolated low intensity returns occur on the ice surface, an N-neighbour filter is used to exclude points which are isolated or with few neighbours.

The central tendency of a set of noisy points is used because LiDAR points scatter in both directions about the surface which is being measured (Steer et al., 2012), and with noisy LiDAR it cannot be assumed that the lowest Nth percent of points actually lie on a surface. This function results in many false negatives - i.e. actual water points are excluded - but returns a reliable, sparse set of open water points (Figure 4.3).

4.3.2 Using reference points to model a dynamic sea surface

A LiDAR swath may slope across-track in the absence of reliable boresight calibration for ship-based surveys. It may also undulate along-track due to dynamic sea surface topograhy (e.g. long wave swell, tides, wind stress). Kurtz et al. (2013) establish that the sea surface under pack ice in the absence of swell may slope (relative to the ellipsoid) in an essentially linear fashion over hundreds of metres. This is appropriate across a LiDAR swath (for APPLS, 250 m to 400 m), but a typical survey over sea ice may cover hundreds of kilometres, at which scale the sea surface is essentially variable and has non linear topography. This is addressed using a polynomial spline fit to the extracted reference points, which is used to extrapolate a sea surface beneath ice floes.

Point coordinates are normalised such that the spline surface is fit to points within the same range along their X and Y (or East and North) dimensions - for example $0 < E < 1$ and

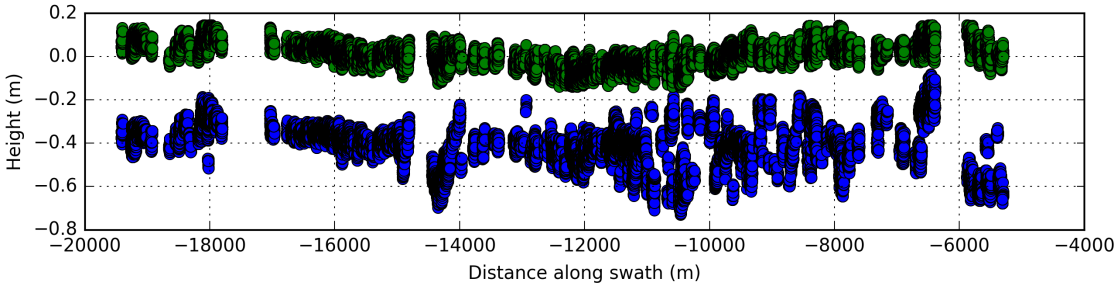

Figure 4.4: Results of adjusting water points using a 2D spline fit. Points in blue are identified as water by intensity and neighborhood size filtering in the original LiDAR swath (translated vertically by 22 m to allow plotting both sets of points on one axis). Points in green show the result of levelling by fitting and subtracting a 2D spline to the identified points. Point scatter is still present due to instrument noise described in Chapter 3.

$0 < N < 1$. The normalisation of each axis ensures that the bounds of an extrapolated spline surface closely approximate the bounds of the interpolated spline surface, which helps to constrain extrapolated values to within realistic ranges. The spline is heavily smoothed to minimise plane variations due to systematic LiDAR noise, and evaluated at each water point to determine a set of elevations near the fitted spline.

These are subtracted from water point heights to produce a set of point elevations approximating a plane at $Z = 0$. Evaluating the spline fit at each LiDAR point in the set provides a 'surface' to which points are 'levelled' by subtracting elevation on the fitted spline surface from raw points. After modelled surface elevations are removed and the point cloud is 'levelled' to a water surface and point coordinates are transformed back to real world coordinates. This process is iterated twice - once to translate points from ellipsoidal heights to the water surface frame, and a second pass to remove any remaining across-swath swath slope, which is occasionally observed after a single processing run[1]. Figure **??** shows the input (blue) water points and the results (green). The LiDAR swath these points are drawn from is mapped in Figure 4.19. Point scatter present in adjusted points is the result of systematic noise described in Chapter 3.

The approach used here is roughly analagous to previous efforts at determining 'sea level' from LiDAR points (e.g., Hvidegaard and Forsberg, 2002; Kurtz et al., 2013; Wang et al., 2013), and most similar to the ordinary kriging method used by Kurtz et al. (2013). It has two key differences: first, there is no predetermined 'scale of linearity' - for example the 2 km segments used by Hvidegaard and Forsberg (2002) or the 1 km segments used by (Wang et al., 2013); and second: the method captures the central tendency of reference point elevations rather than the lowest $N\%$. This approach is substantially simpler than using gravity and ocean models to approximate a surface at high resolution over a small region and carries with it only the uncertainties inherent in the dataset, but has the following caveats:

[1]https://github.com/adamsteer/phd-notebooks/blob/master/Est_ice_thickness.ipynb, accessed 13 May 2016)

- Evaluating a spline outside of the range of training data leads to spurious results. LiDAR swaths must be split so that each segment begins and ends with water points;
- Points must fill the majority of a bounding box drawn around the LiDAR swath, to avoid extrapolation errors in surface fitting. Curved swaths must be excluded from the analysis, or be transformed such that the swath is straightened along one (x,y) dimension;
- Because of noise in the data, some points in the set will fall below '0', or below the sea surface for adjusted LiDAR swaths. These must be dropped from any further analyses to avoid cases of snow depth >total freeboard, positive ice draft or negative ice thickness;

4.3.3 Coregistration of imagery and LiDAR

Collection of photography on SIPEX-II was planned and executed with the analysis of images for ice classification and floe size/open water fraction detection (e.g. Hutchings et al., 2012; Steer et al., 2008; Worby et al., 2008a). With coincident LiDAR, they form a valuable tool for the validation of reference points. Geoferencing of imagery, and subsequent coregistration with LiDAR in the absence of ground control points requires precise knowledge of the aircraft position and attitude. For the flights used here, camera positions were derived by matching flash timing events to images, and then extracting camera position and attitude data from the post-processed GPS+IMU trajectory.

Lens distortion parameters derived using AgiSoft Photoscan on calibration datasets were used to remove lens distortion from images. After applying the lens distortion correction, images are coarsely georeferenced using a Python program which assumes that the underlying surface is a horizontal plane on which LiDAR points lie, hence applies a simple projective transformation using camera extrinsic parameters (heading, pitch and roll) from the aircraft trajectory along with the range to LiDAR points[2]. This process first uses camera intrinsic parameters (field-of-view, sensor size and pixel dimensions) to compute image corners in three dimensional camera-based coordinate space. Next, the corners are projected onto a horizontal plane which is derived from LiDAR points about the camera nadir. Corner positions on the plane are used to derive a projective transformation for the image. Finally, the transformation is applied to each image, which is scaled using sensor dimensions and range to LiDAR points to determine 'real world' surface coverage and pixel resolution. Geolocation is performed after scaling using the camera centre coordinates captured by the APPLS system. Figure 4.5 shows a set of images with a LiDAR point overlay.

While the method is an approximation containing assumptions about surface flatness, it is adequate for the purpose of validating the selection of reference points from the process

[2]https://github.com/adamsteer/python-opencv-image-projection, accessed 13 May 2016

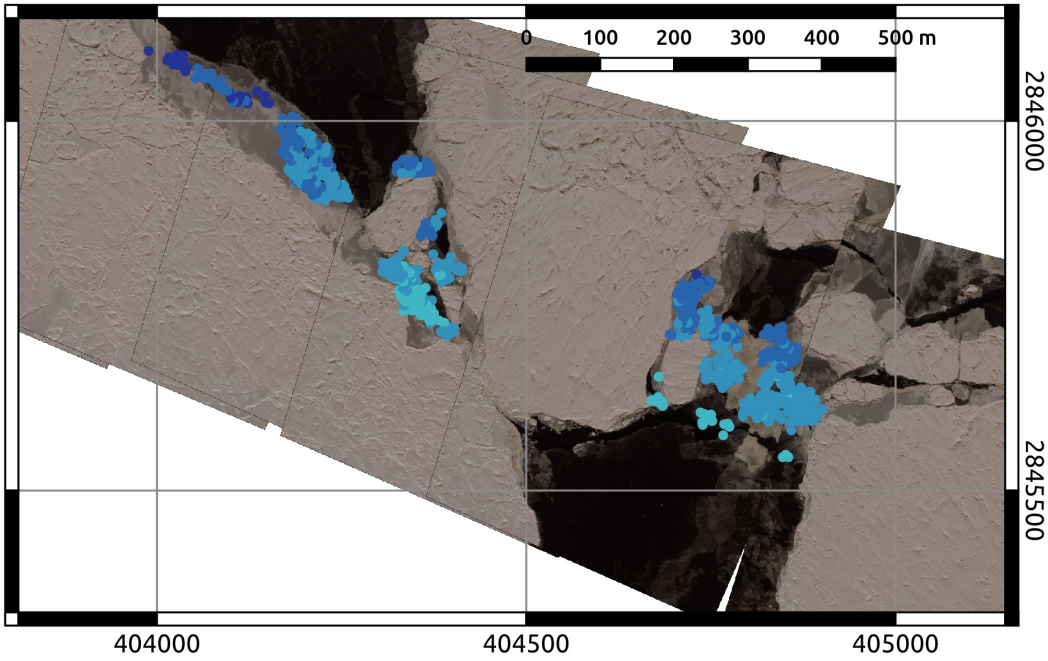

Figure 4.5: A segment of SIPEX-II flight 22, showing keypoints derived from an intensity and neighbourhood size filter overlaid on projected APPLS imagery

described in Section 4.3. It provides visual confirmation that points used as a reference for water or very thin (grease) ice returns are correctly identified. Future development of this method should include a lead classification algorithm (e.g. Onana et al., 2013), and a more rigorous geolocation algorithm, potentially using the surface fitted to water points as an elevation model onto which images are projected rather than a horizontal plane.

4.4 Total freeboard and ice draft from in situ observations and LiDAR: SIPEX-II Ice station 6

At SIPEX-II IS6, a suite of observations were collected which allow a rigorous validation of methods used to derive sea-ice thickness and draft from airborne LiDAR. In situ drill hole observations of ice freeboard and ice thickness were collected on the same day as SIPEX-II flight 11 (13 October 2012). Transect line holes were located along the ICE1 $\rightarrow$ ICE2 line using a tape measure to determine metre spacing, which is accurate to within a few decimetres over 100 m. Ice thickness observations from drill holes distributed around IS6 were positioned in the ice floe reference frame using a total station (see Section 4.4.1). These in situ observations are used to validate total freeboard observations from the APPLS LiDAR Using the distributed drill holes is a particularly important check on biases across the LiDAR swath, ensuring that LiDAR measurements are correctly levelled over a wide area.

Draft observations were collected under IS6 on the same day using an AUV (see Williams et al., 2014b, Floe 10). Figure 4.2 shows the relationship between the AUV track, in situ

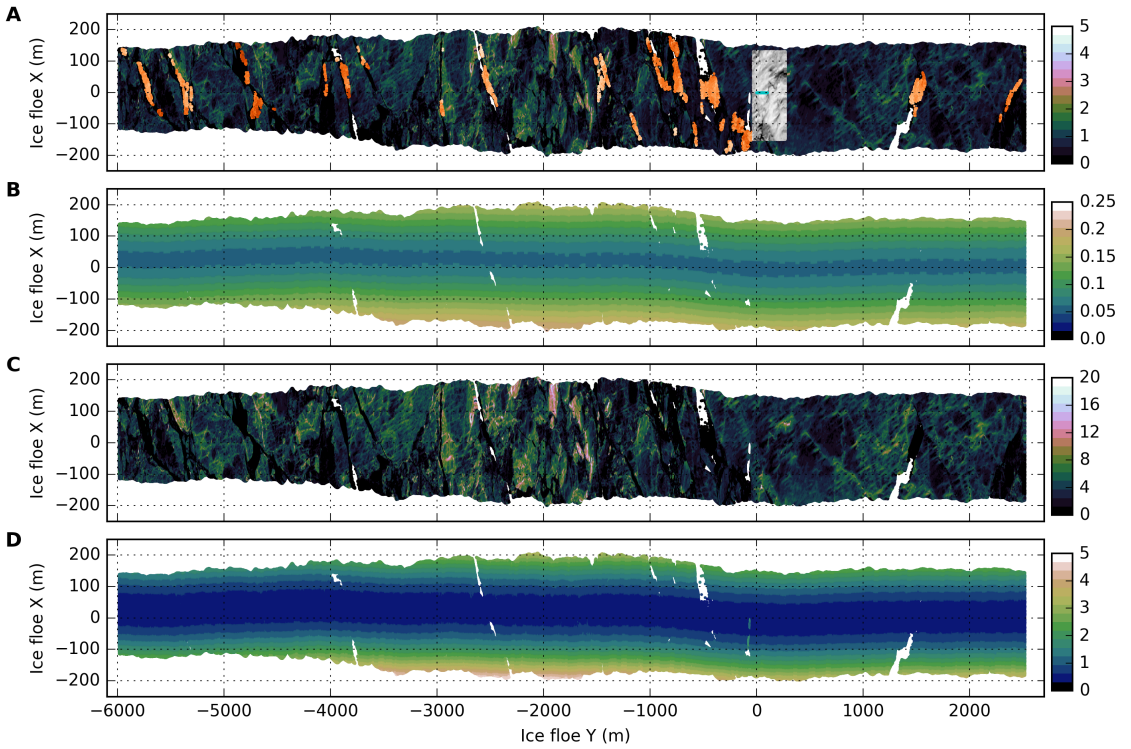

Figure 4.6: Overview of the LiDAR points used for analysis, from SIPEX-II IS6. All colour bar units are metres, and colour scales are chosen to match the parameter range in each panel. X and Y axes scales are unequal, with swaths compressed along-track to aid visualisation of long, thin LiDAR strips. A: LiDAR elevations. Key points used to derive a 'sea surface' are highlighted in orange, the subset of points over the AUV survey are shown in grey, and the 100 m transect line is shown in cyan. B: uncertainty associated with elevations. C: derived ice thickness (note change in colour scale) from each point, and D: uncertainty associated with each ice thickness estimate.

observations and the ice floe surveying system. For IS6, a short segment of LiDAR which covered the region of the AUV survey was used. It contained 1.6×10^6 points, from which 1.63×10^5 were selected as key points for 'levelling' the swath such that the mean elevation of key points is zero (using the method shown in Section 4.3.1 and Section 4.3.2). Figure 4.6 shows the full swath, with key points highlighted, elevation uncertainties, estimated ice thickness and ice thickness uncertainties in Figure 4.6a→d respectively. The subset of LiDAR overlying the AUV survey region is also highlighted as the set of grey points in Figure 4.6a .

4.4.1 On-ice observations

Two dual-frequency GPS receivers were deployed on the ice at each station to provide a connection from a local ice-floe centric reference frame and the Earth-centred, Earth-fixed frame used to coordinate the two receivers and the APPLS aircraft trajectory. Receivers at sites ICE1 and ICE2 (Figure 4.2) were used to define a local datum line, with the site ICE1 forming the origin of a local coordinate system and the bearing to site ICE2 forming an arbitrary northing. Site ICE1 and ICE2 positions were monitored in the local frame

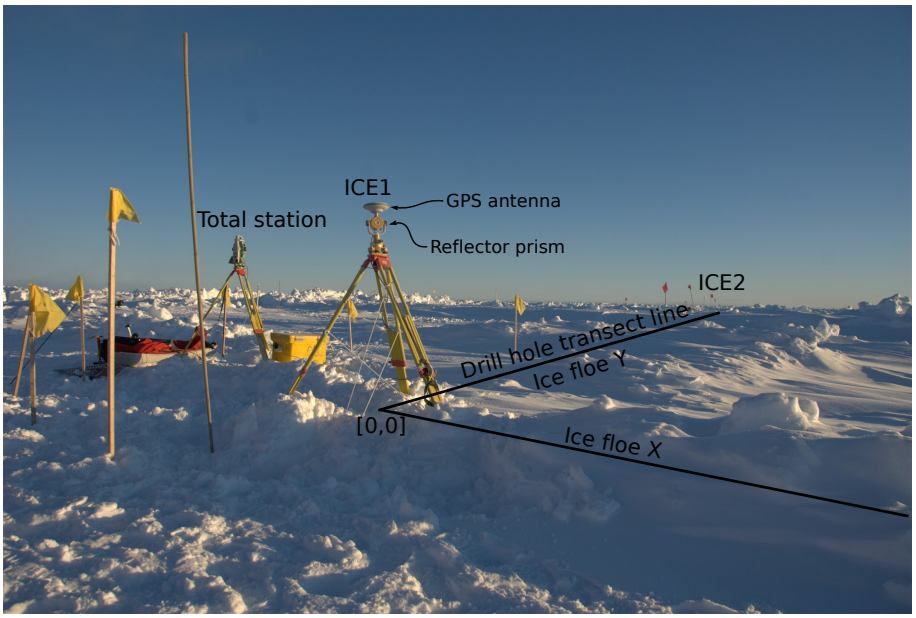

Figure 4.7: Overview of SIPEX-II ice station surveying setup, showing the ice floe reference frame origin at ICE1, the 100 m transect line along the ice floe Y axis, and the total station used to record locations in the ice floe reference frame.

	μF_i	σF_i	μZ_s	σZ_s	μF	σF	μZ_i	σZ_i	$\mu draft$	$\sigma draft$	N
Transect	0.098	0.11	0.27	0.21	0.37	0.19	1.73	0.78	1.63	0.73	100
Distributed	0.13	0.27	0.55	0.31	0.68	0.34	2.61	1.36	2.48	1.15	8

Table 4.1: Descriptive statistics for in situ observations of snow and ice along the transect line, and for the distributed drill hole set

using a total station, which was also used to obtain positions for acoustic beacons used to locate the AUV. Figure 4.7 shows a typical layout for a SIPEX-II ice floe survey, with the reference frame origin at the GPS receiver ICE1, and the drill home transect line forming the ice floe Y axis.

At each ice station, a set of drill hole observations of sea-ice thickness, ice freeboard and snow depth were collected along the baseline between ICE1 and ICE2, approximately 1m apart (hereafter the 'transect line'). For IS6, the first hundred metres from ICE1 toward ICE2 were sampled. Summary statistics are given in Table 4.1. In addition to the transect line, eight drill hole observations were undertaken at sites distributed around the IS6 'survey plot'. Two of these marked floe survey instrument sites (ICE2, and total station), and two were opportunistically gathered at other instrument sites. The remaining four were chosen with geometry and ice types in mind, aiming to complete a rough square around the 'survey plot', and sample ice topography which was distinct from the 100 m transect line. All drill holes were referenced to the floe-local frame using the total station. The six holes not corresponding with survey instruments are shown as green diamonds in Figure 4.2, and summary statistics are presented in Table 4.1.

4.4.2 Airborne LiDAR and imagery

On the SIPEX (2007) and SIPEX-II (2012) research voyages LiDAR survey flights were undertaken over each ice station, and for longer flights extending up to 60 nautical miles (110 km) from the ship. Instruments are detailed in Section 3.2.

For IS6, coregistration of LiDAR and under-ice sonar observations required the translation of the LiDAR points to the floe-local coordinate system. Using the timeseries of GPS observations collected at ICE1 and ICE2, the position of the station ICE1 at the time of overflight was subtracted from the aircraft trajectory which was used to geolocate LiDAR points. The azimuth between (ICE1→ICE2) was used to rotate aircraft positions[3] and derive an aircraft trajectory in floe-local coordinates, fixed at the point in time where the helicopter flew closest to the floe-local origin. A new LiDAR point cloud in floe-local coordinates was derived from this trajectory, using a MATLAB implementation[4] of the LiDAR georeferencing and uncertainty propagation methods presented in Chapter 3

The aerial camera deployed aboard the APPLS system was intended for analysis of sea ice physical characteristics in two dimensions (e.g. Hutchings et al., 2012; Steer et al., 2008). Images were captured every 3 seconds, with a forward overlap between 50 and 60%. This was aimed at providing enough image overlap for mosaicking, and avoiding double-counting of features which extended outside of a single image (e.g. Steer et al., 2008). Over ice stations, many overlapping images were collected, as the camera began operating during instrument initialisation flights prior to undertaking longer surveys.

4.4.3 Total freeboard from in situ observations and LiDAR

Figure 4.8 shows profiles from the airborne LiDAR and transect line drill holes. For LiDAR observations, points within a 1 m wide swath along the transect are shown. Figure 4.9 shows a comparison between LiDAR, photogrammetric point cloud and in situ total freeboard observations (Figure 4.9a). Figure 4.9b shows a map of the drill holes in ice floe local coordinates with the 100 m transect line shown in green.

This shows a very small subset of LiDAR elevation data, but it is a valuable reality check. LiDAR observations are unmodified after levelling using water level points, as described in Section 4.3. Importantly, in situ total freeboards match well with remotely-sensed observations for the distributed drill holes with the exception of point 7, located below the 'survey plot' on IS6. The anomalous observation at that point is likely due to an error in drill hole observation recording.

[3]https://github.com/adamsteer/phd-notebooks/blob/master/aircraft_trajectory_to_local.ipynb, accessed 13 May 2016

[4]https://github.com/adamsteer/LIDAR_georeference, accessed 13 May 2016

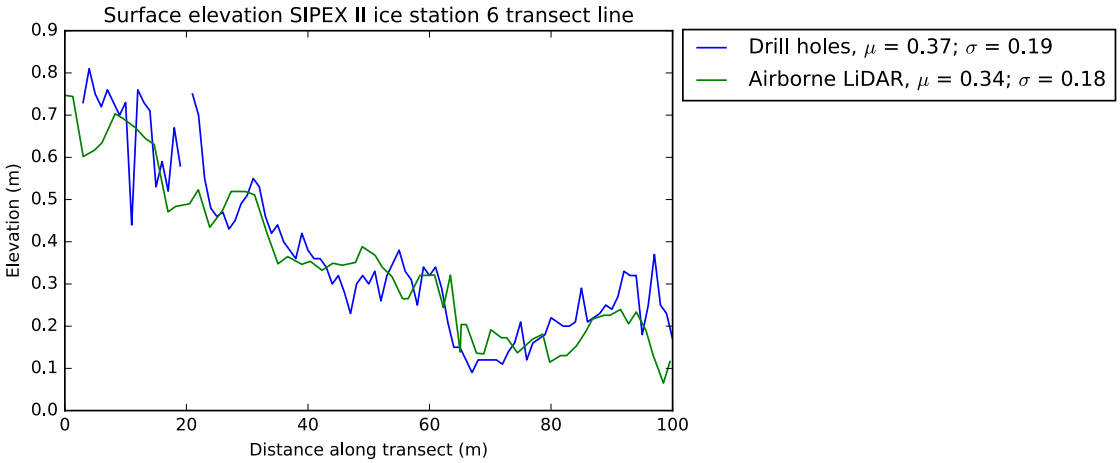

Figure 4.8: Surface elevation along the transect line on IS6 from in situ observation and airborne LiDAR

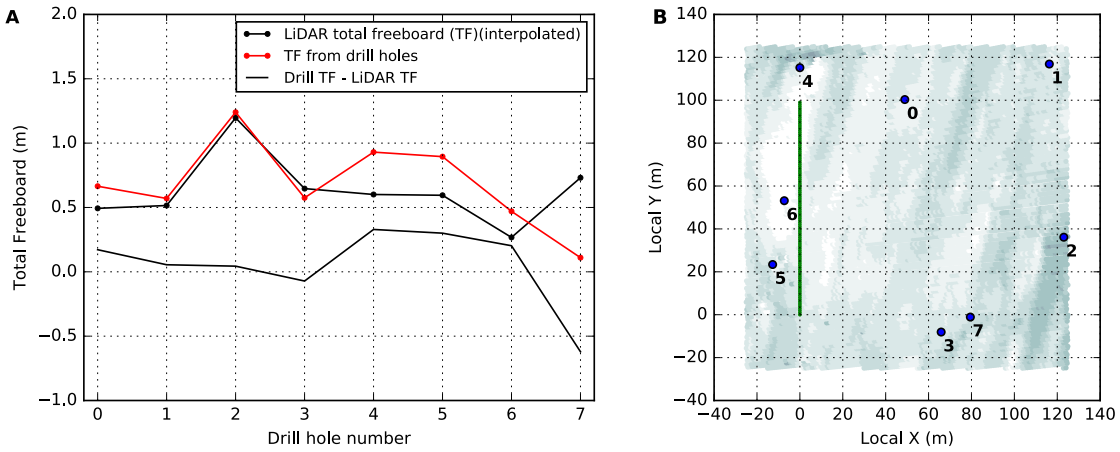

Figure 4.9: A: Total freeboard (TF) from distributed drill holes and LiDAR; and B: positions of distributed holes in the ice floe coordinate system. Green dots along x = 0 indicate approximate transect drill hole sites. Shading in panel B is LiDAR elevation, shown for illustration only.

4.4.4 Ice draft from UAV-based multibeam sonar

The multibeam sonar used to collect ice draft observations on SIPEX-II is described in Williams et al. (2014b). It was deployed aboard a SeaBED class AUV provided by the Woods Hole Oceanographic Institute. Here, we use a set of ice drafts interpolated to 50 cm resolution as a 3D point cloud (Williams et al., 2014a). Airborne LiDAR and AUV-based draft observations are collected in different spatial reference frames. Doble et al. (2011) coregistered LiDAR and sonar observations by iteratively adjusting the two datasets to align features. On SIPEX-II, Navigation beacons for the AUV were tied to the floe-local reference frame using total station measurements. Hence, AUV drafts were expressed in the floe-local coordinate system. Figure 4.13 shows AUV draft observations with LiDAR and in situ observations expressed in the same reference frame.

A subset of AUV draft observations covering an area of 280 m × 305 m (85 400 m^2, 8.54×10^{-4} km) was selected for the following analysis, which had full sonar data coverage, contained the IS6 100 m drilled transect line, and had full LiDAR coverage. While this is a tiny region compared to the extent of Antarctic pack ice, this dataset contains more observations at a metre scale than the record of in situ data collected from East Antarctic pack ice to date.

4.4.5 Choosing model parameters for deriving ice draft from altimetry

Before estimating ice draft from altimetry, appropriate choice of parameters for the hydrostatic model (Equation 1.1) is essential for a realistic estimate of sea-ice thickness. Using AUV draft and in situsnow depth observations as a guide, an empirical approach is used to determine the set of model parameters which can be applied for thickness estimation from airborne LiDAR, such that the best match to UAV drafts is obtained.

Figure 2.3c gives snow depths derived using snow models 1, 4, 7, and 10, and the in situ snow depth from the ice station. Model 10 is the most appropriate choice for this station, giving the closest approximation to in situ values. Snow density is derived from SIPEX-II in situ observations (326.31 kg m^3, Toyota et al. (2016)), as is sea water density (1028 kg m^3, Hutchings et al. (2015)). Ice density is the remaining variable, with a published range of 800 kg m^3 to 915 kg m^3 (Hutchings et al., 2015; Price et al., 2014). From SIPEX-II, observed densities were in the lower range (Hutchings et al., 2015), with a starting point at 800 kg m^3 for samples consisting of granular porous ice. Chapter 2 showed that snow depth, ice density and total freeboard were the strongest drivers of sea-ice thickness using the model employed here. Ice density, in particular, is very poorly understood for sea ice off Antarctica.

To choose an 'optimal draft', the intersection between mean ice draft from AUV observations and mean ice draft from LiDAR observations was found. Figure 4.10a shows the optimal density using a snow model from all east Antarctic observations (Relationship 10, Chapter 2). Figure 4.10b shows the optimal density using a SIPEX-II only snow model (Relationship 7, Chapter 2).

Using the snow depth model for all East Antarctica, the mean modelled snow depth for IS6 is 0.5 m, almost double the transect line mean of 0.27 m. The ice density required to match AUV draft from IS6 is 915.6 kg m^3. Table 4.2 provides a comparison of draft summary statistics from the AUV and modelled from LiDAR using these parameters. While the empirically determined draft value is within the range of observed Antarctic sea-ice densities, it is substantially higher than the observed range for SIPEX-II (800 kg m^3 to 870 kg m^3) from direct measurement of ice cores. However, this figure does fall within the range of densities (915 kg m^3 to 930 kg m^3) obtained from SIPEX-II sites using the ?transect method? (Hutchings et al., 2015, see), which is based on the same model used to derive sea-ice thickness from elevation (see Equation 1.1). With this in mind, for the rest of this study the snow model derived from all East Antarctic observations is used when estimating ice thickness from LiDAR, with a sea-ice density of 915.6 kg m^3.

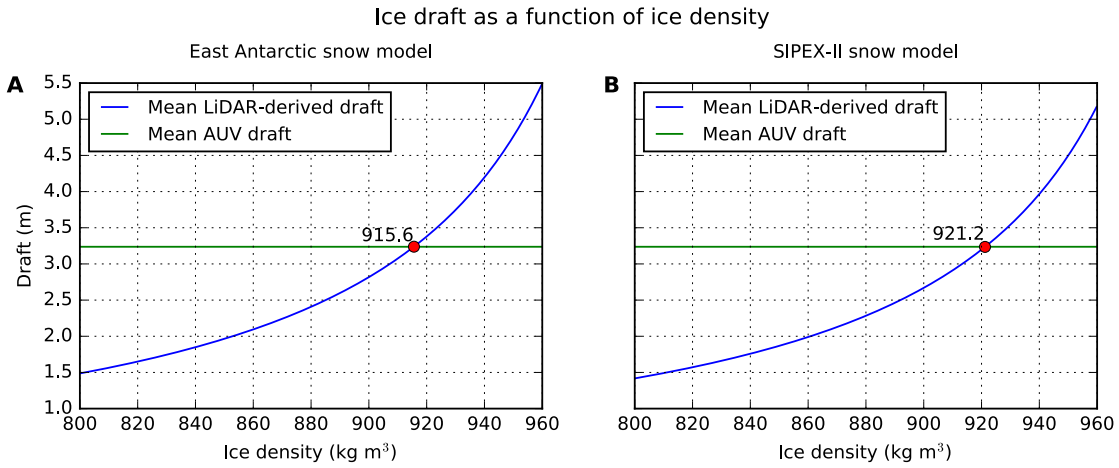

Figure 4.10: Picking an optimal density for modelling ice draft from LiDAR such that mean draft is similar to mean draft from UAV observations. A: using the snow model derived from all east Antarctic in situ observations, and B: using the snow model derived from only SIPEX-II in situ observations.

	Ice density (kg m^3)	$\mu draft$	$\sigma draft$
LiDAR estimates	915.6	3.23	1.62
AUV observations	-	3.23	1.94

Table 4.2: Mean draft estimates from LiDAR and AUV observations

4.4.6 Ice draft from in situ observations, LiDAR and AUV

With model parameters in place, an assessment against in situ measurements of sea-ice draft is given in Figure 4.11. Drill hole observations and draft from AUV-based sonar match quite well. This implies that the difference in thickness distributions shown in Williams et al. (2014b) is more reflective of sampling bias than a methodological problem with drill hole sampling. For LiDAR the results are consistent with those seen in Chapter 2: under-ice topography reflects surface topography. At around 70 m, the LiDAR derived draft estimate diverges from drill hole and AUV observations because the surface topography is essentially flat (see Figure 4.8), and does not reflect the underlying ice bottom topography.

4.5 Floe-scale total freeboard and draft

Using a small set of drill hole observations is a valuable tool to check the veracity of remotely sensed observations, but limited by spatial coverage and potential sampling bias. In this section, the view is expanded to a floe-scale using draft observations from the AUV deployed under IS6 and coincident airborne LiDAR. The AUV observations were collected in a local coordinate system derived from the GPS and total station survey described above. The airborne LiDAR used in this section were co-registered to AUV observations by transforming the aircraft trajectory into the local coordinate system, accounting for ice

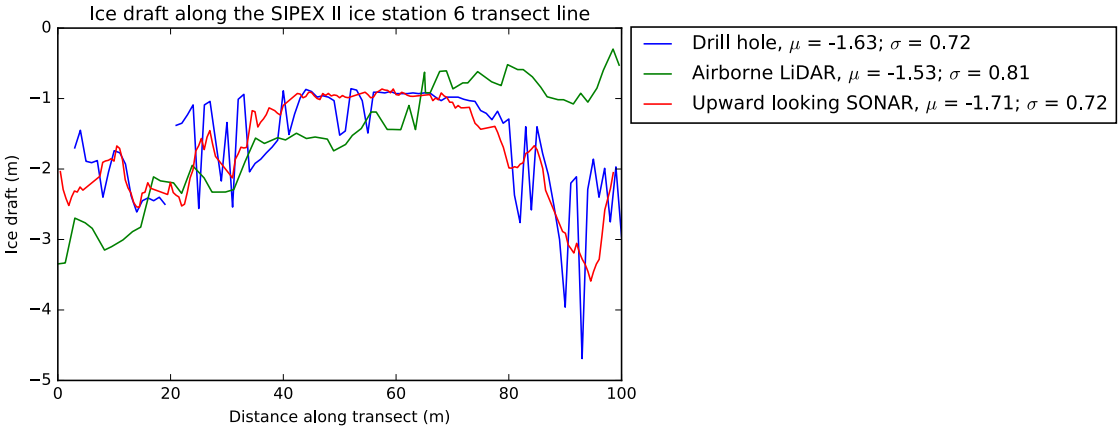

Figure 4.11: Along-transect draft observations and estimates for SIPEX-II ice station 6, from in situ observations, LiDAR, and upward looking SONAR (AUV)

floe drift and rotation using observations from the on-ice GPS system[5]. The LiDAR point cloud was then produced directly in the floe-local coordinate system using the MATLAB implementation of the georeferencing equations shown in Section 3.3. Water points were extracted and the point cloud levelled using the procedure shown in Section 4.3.

4.5.1 Uncertainty surrounding ice thickness estimates from airborne LiDAR

Uncertainties in the draft estimates from airborne LiDAR propagate from the LiDAR point cloud, and from in situ observations used to derive draft. Figure 4.12 shows a map of LiDAR point uncertainty (detailed in Chapter 3) and corresponding ice thickness uncertainty (Detailed in Chapter 2).

For the patch considered, mean elevation uncertainty is 0.08 m with a range from 0.06 m to 0.14 m from swath nadir to swath edge. Mean uncertainty for draft estimates is 1.08 m, approximately 30% of the mean thickness, with a range from 0.43 m to 2.74 m. The dominance of angular uncertainties as range increases is documented in Section 3.8, and the pattern of point scatter away from nadir is demonstrated in the technical report Steer et al. (2012). Applying a mean value for elevation uncertainty would artificially reduce uncertainty for thickness estimates away from instrument nadir, and artificially increase uncertainty near nadir.

4.5.2 Qualitative comparison of LiDAR-derived and AUV draft

Figure 4.13 shows a map of ice draft derived from airborne LiDAR, and draft observed by the AUV-borne upward looking SONAR. This is a view from above, and shows the drill hole transect line highlighted in orange along the AUV draft surface.

[5]https://github.com/adamsteer/phd-notebooks/blob/master/aircraft_trajectory_to_local.ipynb, accessed 13 May 2016)

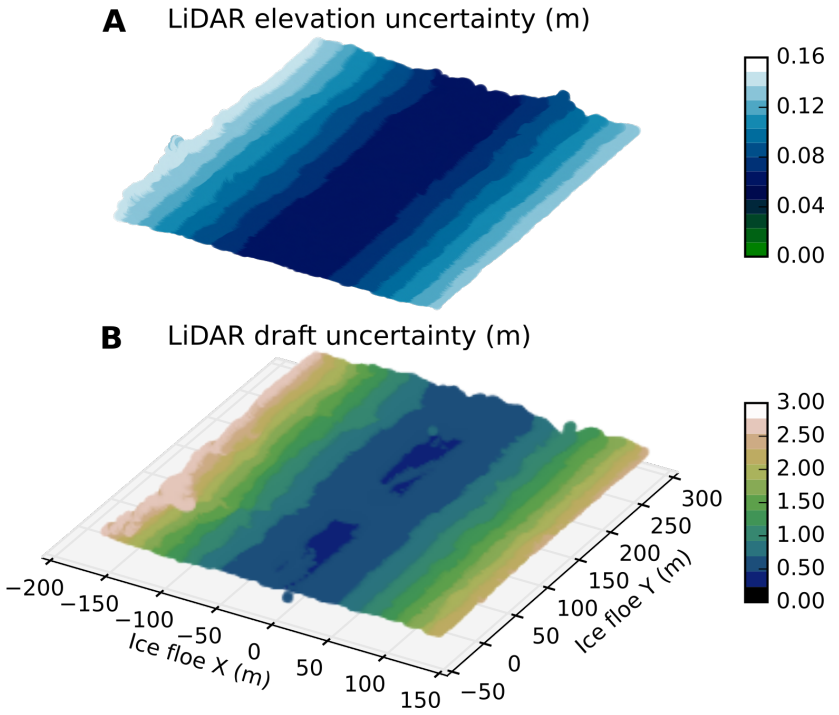

Figure 4.12: Height uncertainty in LiDAR elevations (A) and derived drafts (B). Averaging uncertainty over the swath would unrealistically reduce uncertainty about swath edges, and increase uncertainty near nadir.

The standout feature in these maps is that small-scale under-ice topography derived from altimetry is exaggerated. Where the AUV observations found relatively smooth surfaces, there are dune-like features modelled at the ice/water interface. Larger features are relatively well represented, although the shape and extent of deep keels is not well reflected in surface topography. This clearly visualises a key numerical observation of Chapter 2, being that surface and under-ice topography are poorly related. However - focussing on larger-scale features there is a clear correspondence at least between ridge peaks and ridge centres, and under-ice features. Finally, this work clearly shows the sampling bias inherent in drill hole observations. Drill holes sample a very small section of ice, and for this ice station are quite unrepresentative of nearby ice conditions.

4.5.3 The relationship between LiDAR-derived and AUV draft

At the scale of individual ice floes, the relationship between surface and under-ice features is important in properly modelling the sea-ice thickness distribution from altimeters. In Chapter 2, using drill hole observations, the relationship between surface and under-ice topography is weak. This implies that the estimation of sea-ice thickness at a floe scale

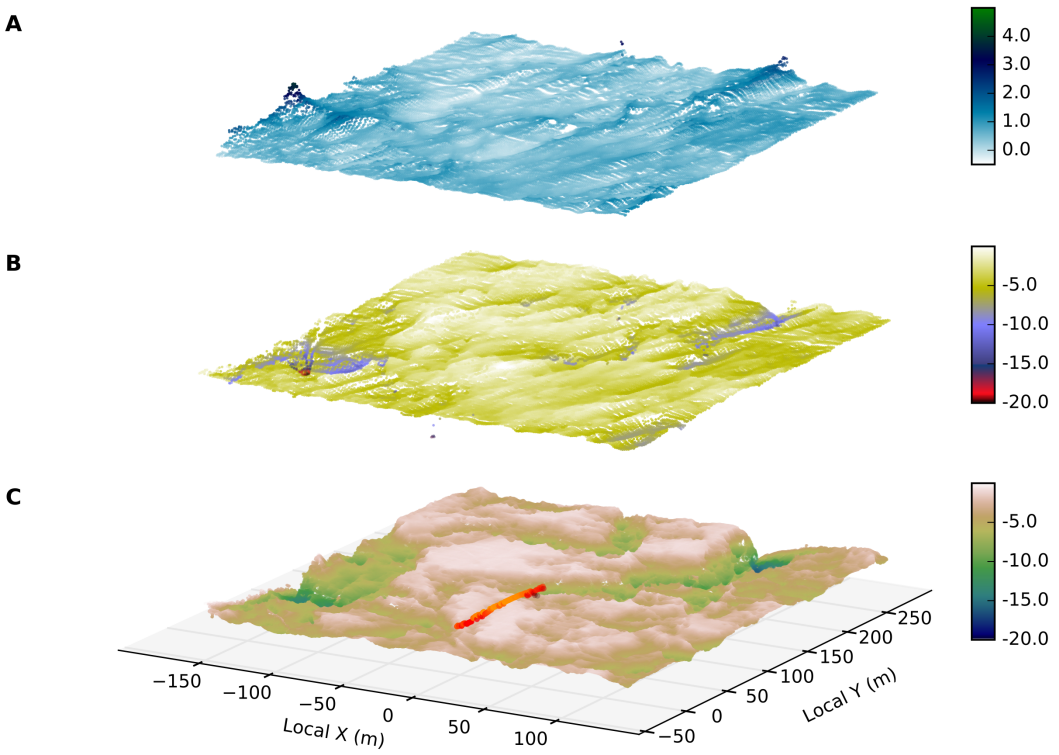

Figure 4.13: Airborne LiDAR topography and draft, compared to AUV-observed sea-ice draft. A: ice topography observed by the APPLS LiDAR. B: ice draft derived from airborne LiDAR. C: ice draft observed by AUV-borne upward looking sonar. Drill hole draft observations are highlighted in orange.

is nearly meaningless, as the upper surface is a poor predictor of the ice below. However, drill hole lines are a very limited sample of the spatial variability of sea-ice. Using co-located AUV and LiDAR observations over a larger patch of ice, it is clear that large surface features are reflected in under ice topography, but smaller-scale features bear almost no resemblance to the snow-filled surface, since the underside of the ice is smoothed by constant contact with the ocean.

Resampling AUV and LiDAR derived draft observations to a common 1 m grid allows direct examination of the differences between the two datasets. Figure 4.14 shows AUV draft (a) and draft derived from LiDAR (b). Figure 4.14c shows a difference map between AUV draft and LiDAR-derived draft. The keels underlying ice ridges on this ice floe were substantially wider than ridges, consistent with previous investigations (Doble et al., 2011; Granberg and Lepparanta, 1999; Kovacs et al., 1973; Timco and Burden, 1997; Wadhams

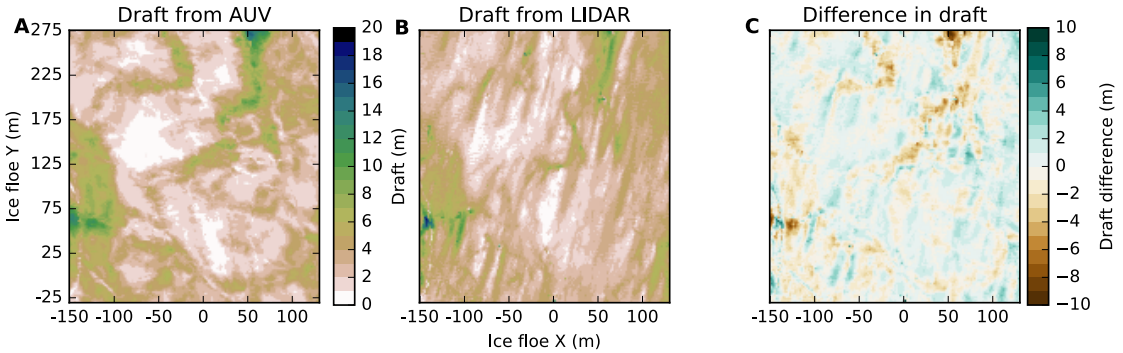

Figure 4.14: Draft maps from AUV observations (A), and derived from airborne LiDAR (B); C shows a difference map between the two surfaces. Positive values (blue) indicate that LiDAR-derived draft is deeper than AUV draft. Negative values (brown) indicate that AUV draft is deeper than LiDAR-derived draft. The snow dune pattern reflected well in LiDAR based estimates, as linear features where LiDAR draft is deeper than UAV draft.

et al., 1992). This is visible as a phase change between strongly positive (blue) and negative (brown) differences near keels. Using the non-parametric Spearman?s *Rho*, the correlation between LiDAR-derived draft and AUV draft is 0.67, providing reasonable confidence in the methods employed here to estimate ice thickness and draft from LiDAR at a floe scale. However, there are clear differences between the LiDAR-derived and observed ice-ocean interface at smaller scales (tens of metres).

4.5.4 Relationship between surface and under-ice features

On this 'floe scale' representation, topography and draft are very well correlated. Using the non-parametric Spearman's *Rho*, the correlation between LiDAR topography and AUV draft matches the relationship between LiDAR-derived draft and AUV draft. This indicates again that using the ice thickness models presented here, surface features are directly reflected as under-ice features, and the modelled ice/ocean interface is highly correlated with observed total freeboard ($Rho = 1.0$).

A strong correlation between surface and under-ice features is the basis for investigating an ice draft/total freeboard ratio R, to allow direct conversion of total freeboards to an ice draft estimate. For the patch of ice shown here, the ratio R (draft/total freeboard) is 5.89. However, Figure 4.15a shows that while there is an apparent linear relationship, the predictive power of a model following the central tendency of the scattered points is extremely weak. For any choice of total freeboard below 3 m, the range of drafts to choose from is 5 m to 10 m. Figure 4.15b and c show total freeboard and draft for 'rough' and 'smooth' ice respectively (detailed in Section 4.5.5).

The vertical lines in Figure 4.15 are plotted at 2 m (red), 1 m (green), 0.5 m (blue) and 0.2 m (black). At elevations of 1 m and 2 m, there is a range of approximately 12 m in ice draft values which could apply to a model for predicting draft directly from elevation.

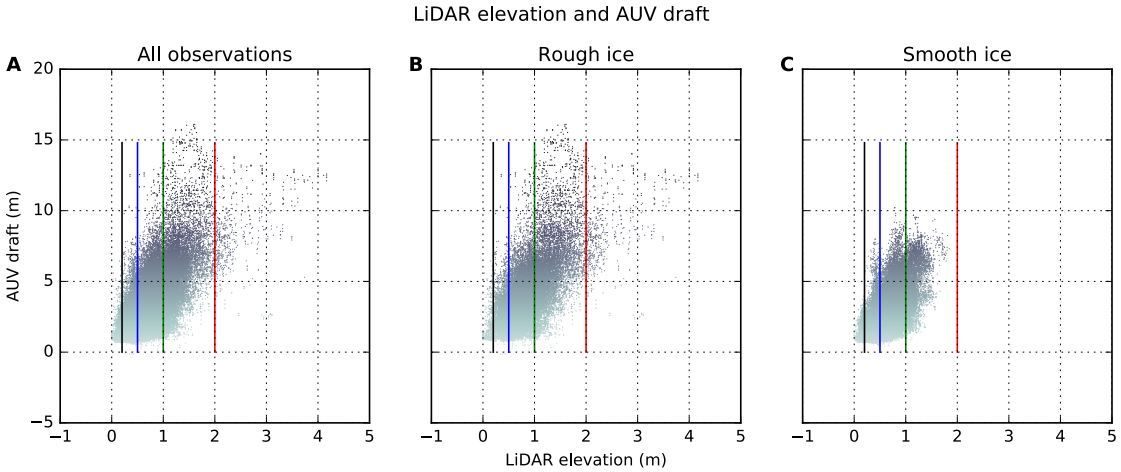

Figure 4.15: Scatter plots of LiDAR elevation vs. draft from AUV. Vertical lines denote total freeboards of 0.2 m (black), 0.5 m (blue), 1 m (green) and 2 m (red) to illustrate the range of draft choices available for a given total freeboard observation. Panel A shows all observations, panel B shows 'rough' ice, and panel C shows 'smooth' ice.

At 0.2 m the situation is better, narrowing the range to approximately 2 m. For the ice studied here, determining a draft directly from surface elevation is unrealistic - which adds some confidence to the process of first modelling snow and then deriving a sea-ice thickness and draft.

Figure 4.15b and c provide an insight into the distribution of elevations for deformed and relatively smooth ice. Figure 4.15b shows that 'roughness', presumably showing deformed ice, occurs across the range of observed total freeboard - and cannot be taken alone as a proxy for high total freeboards. Figure 4.15c shows that total freeboards for 'smooth' ice are lower, but still cover at least 30% of the observed range.

4.5.5 Mapping 'smooth' and 'rough' ice

In the Arctic, Doble et al. (2011) found that 'rough' regions in the under-ice topography showed a stronger relationship between total freeboard and draft than 'smooth' surfaces. This is likely in part due to the decoupling of surface and under-ice topography near deformed surface features, where ice keels extend beyond the boundaries of 'ridge' features on the surface. In the context of estimating ice thickness from instruments mounted on aircraft or satellites the roughness of the ice/ocean interface is beyond current remote sensing capabilities. In this study, 'rough' and 'smooth' regions estimated from surface topography are used investigate surface $\rightarrow$ keel relationships.

The standard deviation of total freeboard within a 5.5 m radius of each LiDAR point is used as a proxy for ice roughness, based on the 11 m smoothing distance chosen by Doble et al. (2011), which both mimics the footprint of the future ICESat-2 instrument and increased the correlation they found between total freeboard and ice draft. The mean

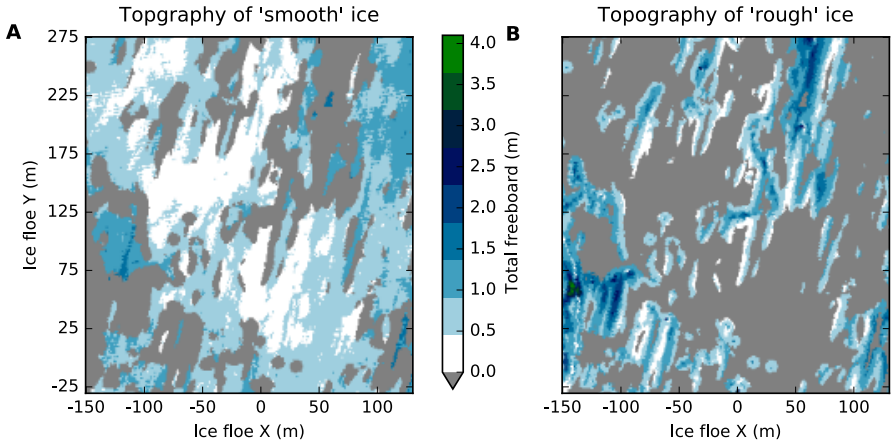

Figure 4.16: Surface topography for 'smooth' (A) and 'rough' (B) ice. Grey regions are masks, colours show total freeboard

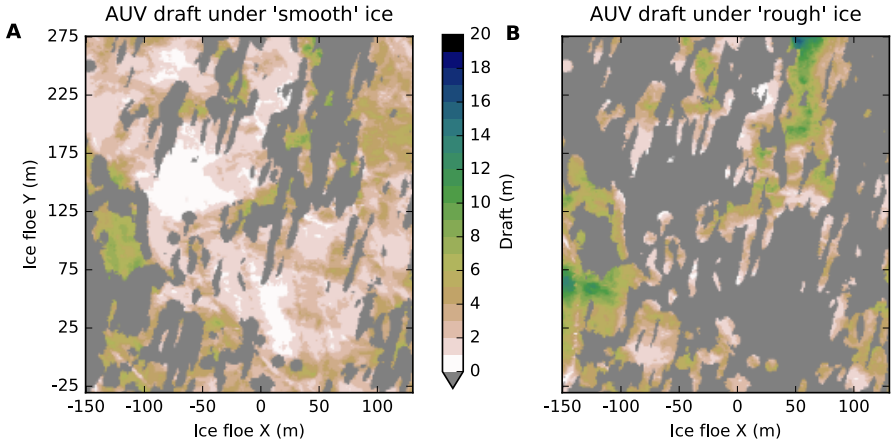

Figure 4.17: AUV draft underlying 'smooth' (A) and 'rough' (B) ice. Grey regions are masks, colours show ice draft.

of neighbourhood standard deviations was used to segment 'rough' and 'smooth' regions of ice. The segmentation of ice topography is shown in Figure 4.16. Using this method, 64.5% of the surveyed patch was 'rough' ice and 35.5% of the surveyed ice was 'smooth', a division similar to that found by Williams et al. (2014b) and Worby et al. (2008a). Mean total freeboard for 'rough' ice was 0.89 m (σ 0.43), and for 'smooth' ice 0.64 m (σ 0.28) Figure 4.17 shows maps of AUV draft underlying 'smooth' and 'rough' surface topography.

The deepest ice drafts are captured under 'rough' terrain, and shallower drafts appear to correspond well with 'smooth' regions, shown also in Figure 4.15c. Also evident is that ice keels (deep drafts) extend beyond regions of deformed ice on the surface, which is well documented for sea ice in the Arctic (e.g. Doble et al., 2011; Kovacs et al., 1973). Fully exploring the relationship between individual ridge systems and their corresponding keels is beyond the scope of this study. However, this work has provided the tools required to

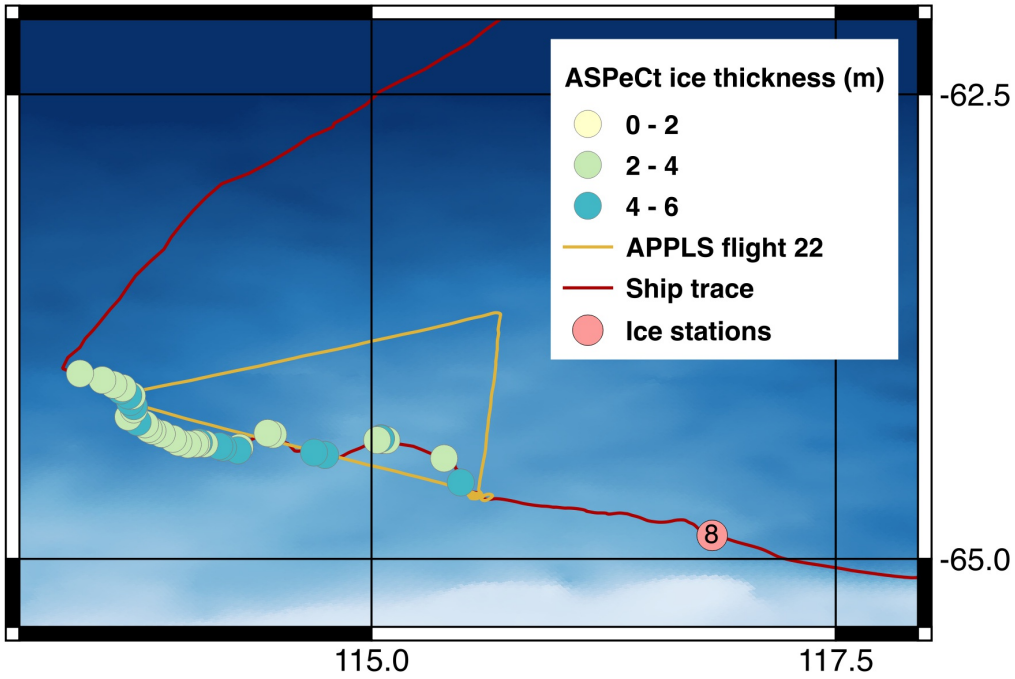

Figure 4.18: Map of ASPeCt ice thickness observations and LiDAR derived ice thickness in the same region.

start a deeper analysis[6].

4.6 Regional-scale sea-ice thickness from airborne LiDAR

Between 5 and 9 November 2012, RSV Aurora Australis sailed west in the pack ice, roughly following the southern leg of APPLS flight 22 (5 November 2012). Ship based observation of ice thickness following the ASPeCt protocol (Worby et al., 2008b) were taken at hourly intervals. While the sea ice surveyed by flight 22 will have drifted westward by the time the ship completed it's passage, the ship remained within a similar ice regime for most of its time in the pack ice zone. Given this factor, the two sets of observations can be used to compare results in a qualitative sense. Figure 4.18 shows both sets of observations. A subset of the LiDAR points used is shown in Figure 4.19.

4.6.1 Airborne LiDAR and ASPeCt observations

Flight 22 was georeferenced in an Earth-Centred, Earth Fixed frame, from which LiDAR points were projected in UTM coordinates. For sea level determination, these were transformed to a local coordinate system centred about the middle of the swath, to assist with normalising the 2D space occupied by LiDAR points for surface fitting. For computational reasons, the flight leg was split into two segments of approximately 55 km,

[6]https://github.com/adamsteer/phd-notebooks/blob/master/draft_r_roughsmooth.ipynb, accessed 13 May 2016

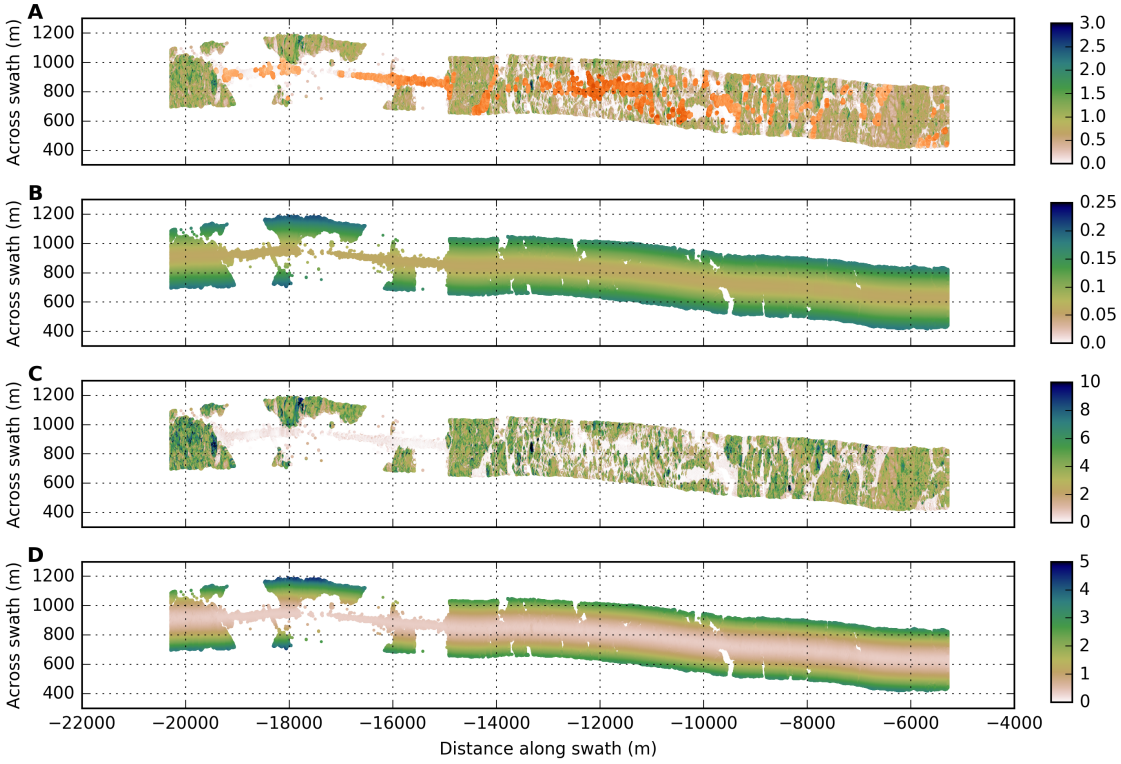

Figure 4.19: A short segment of points used for analysis from SIPEX-II Flight 22. All colour bar units are metres, and colour scales are chosen to match the parameter range in each panel. X and Y axes scales are unequal, with swaths compressed along-track to aid visualisation of long, thin LiDAR strips. A: LiDAR elevations. Key points used to derive a 'sea surface' are highlighted in orange. B: uncertainty associated with elevations. C: derived ice thickness (note change in colour scale) from each point, and D: uncertainty associated with each ice thickness estimate. The coordinate system shown here is transformed from UTM such that the swath fills most of a bounding box around the points.

containing 10.3×10^6 and 8.7×10^6 points respectively. In the first segment, 1.27×10^6 water key points were detected and used for surface fitting. In the second, there were 8.1×10^5 key points. These were confirmed as 'water points' by visual inspection of the point clouds and using co-registered imagery to examine segments of the LiDAR observations. From 19.02×10^6 LiDAR points, estimated mean ice thickness was 4.02 m (σ 2.73 m), with propagated uncertainty ranging from 0.35 m to 5.2 m. The uncertainty in total freeboard observation ranged from 0.06 m to 0.22 m, with extreme uncertainty values arising from high freeboard (up to 10 m) icebergs present in the LiDAR. Dropping observations where total freeboard exceeded 3 m reduced mean ice thickness by 0.01 m, well inside the sensitivity of the instrument.

Over three days, 55 ASPeCt observations were collected in the region covered by Flight 22. The ASPeCt protocol asks observers to identify three thickness classes, with 'primary ice' being the thickest class, 'secondary' the next thickest, and 'tertiary' the thinnest ice class. Where more than three distinct ice types are present, the observer exercises their judgement about how best to fit manifold ice types into 3 classes. Where deformation is

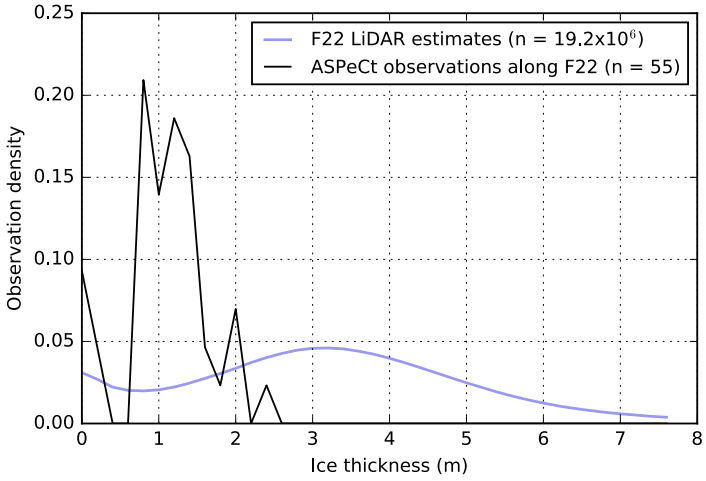

Figure 4.20: Density functions for ice thickness from ASPeCt observations and airborne LiDAR at a regional scale (F22).

present, the observer must estimate the relative proportions of rough or smooth ice and ridge sail heights (Worby et al., 2008b). Primary ice thickness estimates are used here, as weighted mean ice thickness estimates from the ASPeCt observations for SIPEX-II are not yet available.

4.6.2 Comparing ice thickness estimates from LiDAR and ASPeCt

In the same region, the thickest ice class recorded from 55 ASPeCt observations had a mean of 1.83 m (σ 0.55 m). A probability density plot (Figure 4.20) shows that ASPeCt observations essentially captured one tail of the sea-ice thickness distribution, assuming that the LiDAR-based estimates represent reality. This is unsurprising, since ships navigating in ice prefer the easiest route - whereas aircraft overfly ice without concern about the ability to navigate through it. Anecdotally, determining ice thickness for a region surrounding a ship is a difficult task. From a ship?s bridge ice all looks relatively flat, sail heights are difficult to judge, and observers are asked to define ice classes which average much of the variability inherent in Antarctic pack ice over essentially unknown scales. Finally, where ice thicker than 1 m to 2 m is encountered, it is difficult to directly assess ice thickness and an observer must make an estimate to the best of their ability.

In this section the parameters used to estimate ice thickness from LiDAR were specifically tuned so that mean draft at a floe scale would match AUV observations of ice draft (Section 4.4). Using sea-ice density value from the range observed on SIPEX-II (800 kg m^3 to 870 kg m^3) would reduce the mean ice thickness by 1 m to 2 m (Figure 4.10), bringing thickness estimates from LiDAR closer to ASPeCt observations. However, observations of sea-ice draft in the regions (Williams et al., 2014b) are in general agreement with the values estimated from LiDAR elevations. In this light, sea-ice thickness estimates using the ASPeCt protocol are clearly biased toward the thinner ice encountered in the SIPEX-II region.

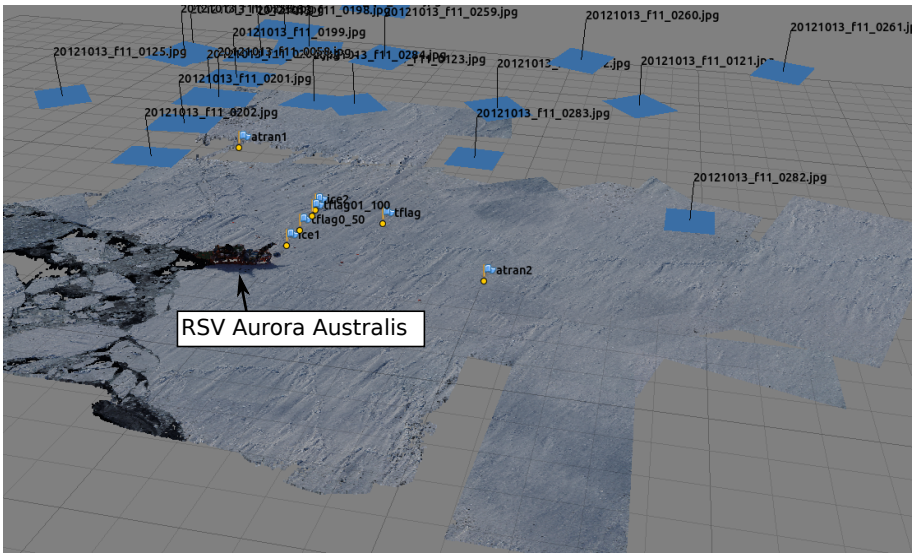

Figure 4.21: Photogrammetric model overview, showing camera positions and ground control points used to constrain the ice topography model.

4.7 3D photogrammetry as a method for modelling sea ice

The APPLS camera system was not operated with reconstruction of sea ice topography in mind. However, closely overlapping flightlines near ice stations provided image sets with enough overlap to test reconstruction of sea ice using 3D photogrammetry (e.g. Fonstad et al., 2013; Snavely et al., 2006; Turner et al., 2012). Numerous studies apply the method to cryospheric observations (e.g. Cimoli, 2015; Eckerstorfer et al., 2015; Nolan et al., 2015; Vander Jagt et al., 2015), providing a strong basis for investigating the use of this technique over sea ice wherever appropriate imagery exist. This study takes the opportunity to compare results over sea ice with coincident in situ observations and LiDAR from IS6.

A set of 30 images obtained over IS6 was used to derive the models shown here. Images were referenced to the local coordinate system, with heights derived from coincident LiDAR observations. Agisoft Photoscan (http://www.agisoft.ru) was used to match images and generate the point cloud. Figure 4.21 shows the geometry of the camera positions, ground control points, and the generated point cloud.

Deriving elevation models using this method gives extremely dense data, approaching the ground resolution of the camera employed to capture images (for APPLS, approximately 0.07 m/pixel). Table 4.3 gives an estimate of point density from each data source used here. For LiDAR, photogrammetry and AUV data, the point density is the number of points in an arbitrary 5 m × 5 m patch, divided by 25 to give a number of points per m^2. For drill holes, the density is nominally 1 point per m^2.

The terrain model derived from imagery was trimmed to a 150 m×150 m patch around the central 'survey plot', to avoid elevation errors arising from lack of image coverage at

Source	Points per m^2
Drill holes	1
LiDAR	7
Photogrammetry	78
AUV	20

Table 4.3: Point density for LiDAR, 3D-photogrammetry, AUV and drill hole observations over SIPEX-II ice station 6

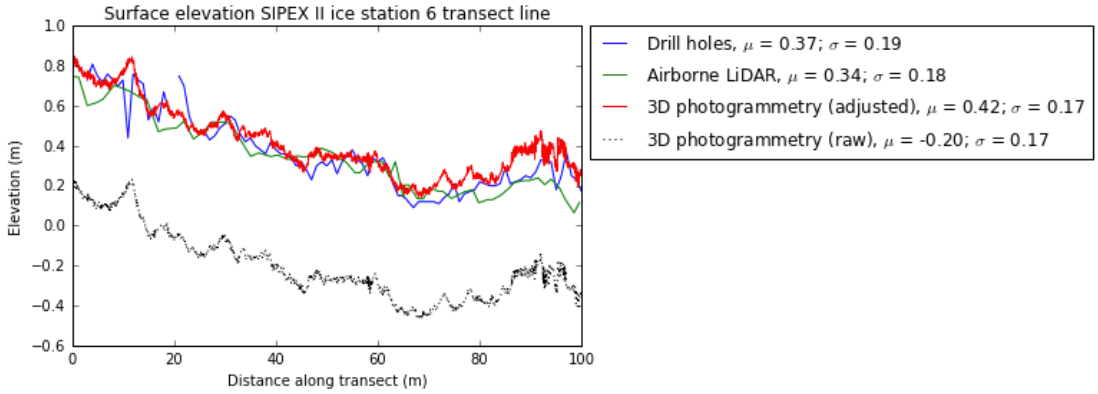

Figure 4.22: Surface elevation along the transect line on IS6 from in situ observation, LiDAR and 3D-photogrammetry

the edges of the UAV survey plot. This left approximately 20×10^6 points in the elevation model. As for LiDAR observations, total freeboard measurements from IS6 drill holes were used for validation. Figure 4.22 shows total freeboard measured at drill holes along the IS6 transect line, LiDAR observations and elevation observations from a 0.5 m swath along the transect are shown.

Photogrammetric points needed a constant 0.614 m added in order to match transect line measurements of ice elevation above sea level. Once this correction was added, the surface model matched in situ observations well at the transect line. Around the floe, the adjusted photogrammetric model performed less well due a lack of overlapping imagery, deviating substantially from in situ and LiDAR observations at sites 2, 4 and 5 in the distributed drill hole set (Figure 4.23).

4.7.1 Comparison of photogrammetry-derived and AUV draft

Following the same process as the LiDAR points, sea-ice thickness and draft was estimated from the photogrammetric point cloud. Figure 4.24 shows ice draft modelled using Structure-from-motion (SfM) elevations (Figure 4.24b) compared with ice draft from UAV observations (Figure 4.24c). Figure 4.24b shows that surface features are very clearly replicated at the modelled ice-ocean interface. For regions of undeformed ice, this presents the same issue as modelling ice draft from LiDAR - an excess of small-scale roughness.

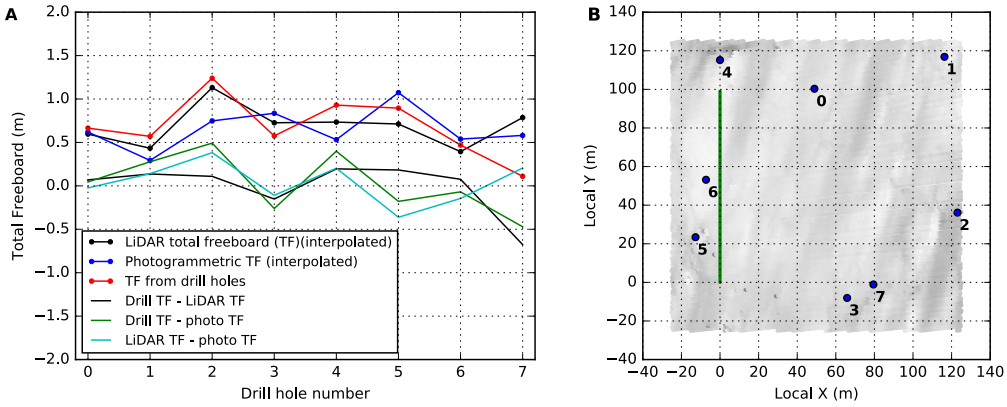

Figure 4.23: A: Total freeboard (TF) for distributed drill holes, LiDAR and 3D-photogrammetry; and B: positions of distributed holes in the ice floe coordinate system. Green dots along x = 0 indicate approximate transect drill hole sites.

However, the use of SfM techniques for modelling surface topography may have an application for increasing detail where appropriate. Figure 4.25 shows that greater detail in surface topography may assist in better modelling of ice thickness over regions of deformed ice. In the final 20 m of the transect line, draft derived from an SfM model is substantially closer to observed draft than its LiDAR counterpart. Combining LiDAR and photogrammetric point cloud observations over 'rough' ice regions is beyond the scope of this study, but may prove useful if conditions for generating accurate photogrammetric models exist.

The primary goal of this exercise was to test a now-common method for terrestrial mapping on sea ice. It is clear that the method is workable, and provides a reasonably accurate and highly detailed view of the sea-ice surface. However, the method only works where substantial overlap exists between images, and relies heavily on accurate matching of features between images (e.g. Fonstad et al., 2013; Snavely et al., 2006). Outside of the small region shown here, inadequate image coverage leads to substantial surface warping. Outlying points make the dataset unsuitable for a broader scale analysis, which is primarily a function of the flight pattern. Nolan et al. (2015) shows that SfM techniques can acquire highly repeatable results over snowy surfaces with rigorous ground control, and a very well controlled aircraft trajectory. These conditions are difficult to meet on drifting sea ice.

4.8 Discussion and Conclusions

Investigating ice thickness modelled from altimetry at the scale of floes or smaller is only made possible by the confluence of several technologies and a well organised field expedition. Missing any of the components in this study would make it practically impossible to adequately asses the results from estimating sea-ice thickness using the APPLS package alone. The on-ice survey work undertaken on the SIPEX-II voyage provided essential data for coordinating airborne, in situ and under-ice observations so

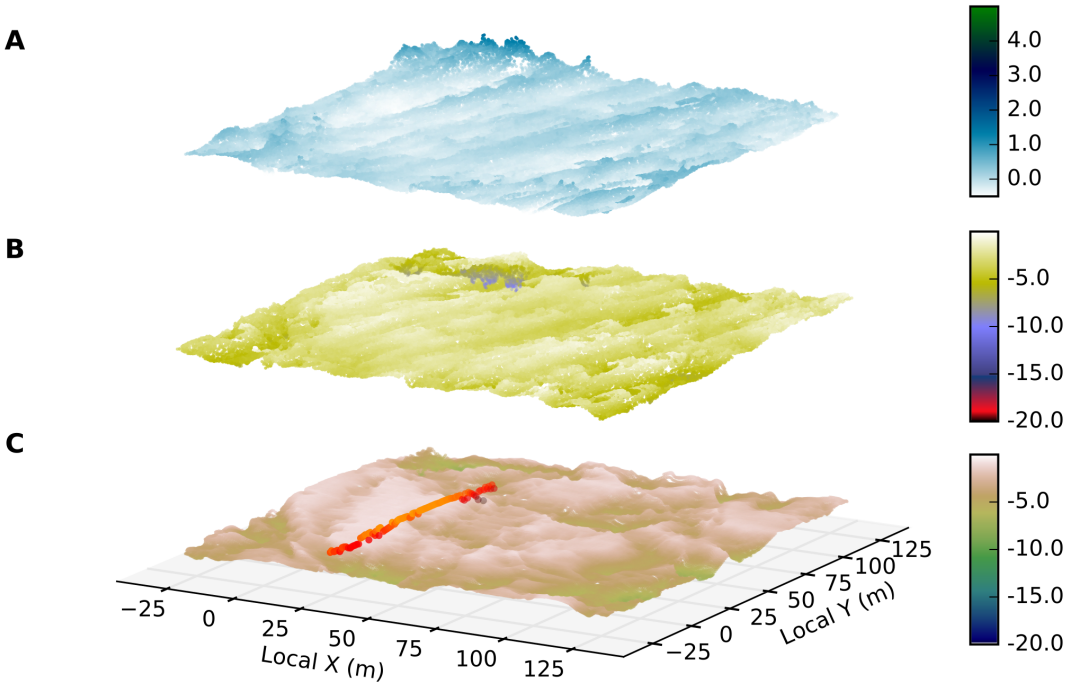

Figure 4.24: 3D photogrammetry-derived terrain and draft models, compared to AUV-observed sea-ice draft. A: ice topography from overlapping aerial photographs. B: ice draft derived from topography C: ice draft observed by AUV-borne upward looking sonar. Drill hole draft observations are highlighted in orange.

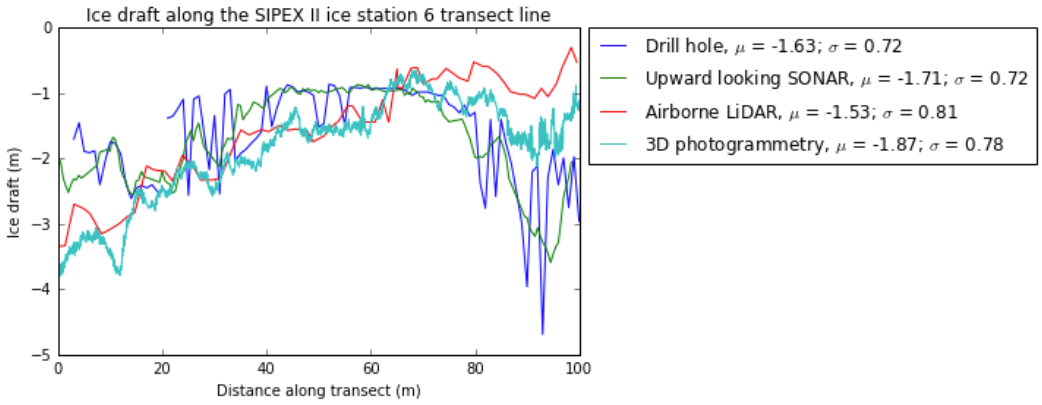

Figure 4.25: Ice draft along the transect line on IS6 from in situ observation, AUV, LiDAR and 3D-photogrammetry

that each could be accurately co-registered and used to validate efforts to derive sea-ice thickness from high resolution altimetry at a floe scale. With these data, a close examination of the correspondence between surface and under-ice topography could be undertaken - in particular investigating the utility of a draft-to-total freeboard ratio (R) for directly estimating ice draft from altimeter observations.

Using AUV draft observations as a guide, input parameters to Equation 1.1 are derived such that ice draft estimated from airborne LiDAR and a snow depth model based an empirical model (Chapter 2) matches observed draft as closely os possible at a floe scale. In turn, doing so, this work indicates that modelling ice thickness at the scale of whole floes is feasible using altimetry observations and an extremely sparse set of in situ ice observations. With a realistic approximation of floe-scale ice thickness, another aim of this study is to demonstrate how the ice thickness distribution estimated by altimetry may differ from the 'true' ice thickness distribution at the scale of metres to tens of metres. It is clear from Figure 4.14 that the under-ice topography estimated using LiDAR is heavily influenced by the snow cover. Visualising the differences between the topography-derived and AUV-observed draft maps makes this extremely clear.

The difference map in Figure 4.14c shows that in this terrain, surface and sub-surface peaks match well. Confirming a well known feature of ice ridge and keel systems, under-ice keels are broader than the ridge systems seen on the surface (e.g. Doble et al., 2011; Kovacs et al., 1973; Timco and Burden, 1997), For smaller features, LiDAR derived draft is overtaken by the topography of snow on the surface. Skyllingstad et al. (2003) point out that small-scale topography at the ice-ocean interface has an important influence on turbulent heat flux from the ocean to the sea-ice cover. This study shows that at high resolutions, the roughness of the ice-ocean interface is overestimated. If these observations, for example, are supplied as input parameters to heat flux models, these will overestimate the turbulent heat flux to the ice. Since deformed ice at the surface generally corresponds with ridge keels, segmenting draft estimates by surface roughness and applying a smoothing factor to ice drafts under 'smooth' surface ice may be an appropriate strategy for future analyses.

Using a ratio of draft to total freeboard (R) to estimate ice draft from total freeboard is unreliable for the ice observed in this study. This is potentially a function of the heavily deformed ice sampled here. While a strong correlation exists between LiDAR elevations and AUV drafts, there are a wide selection of possible drafts at each elevation (Figure 4.15). It is understandable that much effort has gone into defining R or similar values for sea ice (e.g. Doble et al., 2011; Ozsoy-Cicek et al., 2011), since it removes the need to estimate snow depth at every elevation point. However, for the deformed ice sampled on SIPEX-II, it is not appropriate to use R when estimating ice draft from total freeboard. The range of draft values for each total freeboard is potentially explained by variability in the snow depth distribution across the ice floe. Snow depth observations were limited to the transect line and a few distributed sites around IS6. Future efforts to map the snow depth distribution in more detail (e.g. Lieser et al., 2013) will shed more light on the problem of how to model snow depth appropriately.

A key issue is the derivation of an ice density value which brings drafts modelled from LiDAR into close correspondence with drafts measured by AUV. The chosen value ($915.6\,\mathrm{kg\,m^3}$) is artificially high, and impossible to guess without coincident AUV observations. An attempt to modify snow depths such that for total freeboard above the mean total freeboard, snow depth is reduced as a proportion of total freeboard, resulted in an ability to use lower ice densities since snow depths were substantially reduced for ridge systems (Section 5.3.1). However, smooth ice was underestimated and keels were greatly exaggerated, skewing the distribution of ice thickness toward deep, narrow keels[7].

Using a single snow depth value is attractively simple (e.g. Doble et al., 2011; Hvidegaard and Forsberg, 2002), but results in a misrepresentation of the underlying distribution of ice thickness. Applying a RADAR-derived snow depth (Kurtz et al., 2013; Kwok and Maksym, 2014) is an improvement, but applies a single snow depth across a LiDAR swath for each spatial step in the RADAR observation. For level ice with uniform snow, or for point observations (e.g. the retired ICESat) this approach would be suitable. Where ice is deformed and snow depth is highly variable across an altimeter's swath, applying a uniform snow depth across a swath would clearly lead to misrepresentation of the underlying ice thickness distribution. While the approach taken here is not necessarily more realistic, using a variable snow depth distribution opens the door to future improvements in snow modelling - which are strongly dependent on collection of in situ observations which can be tightly coupled to remotely sensed observations. This study begins to take advantage of spatial data integration tools, which will be a powerful addition to future data collection exercises.

At both the single-floe and regional scales, in situ observations of sea-ice thickness are biased toward ice which is navigable by ship and/or safe for deployment of researchers and field equipment. Ships preferentially travel through navigable ice, and drilling teams prefer less deformed ice - evident in Figure 4.13, where the drilled transect line is located near some of the thinnest ice sampled. Figure 4.26 shows the probability density of in situ ice thickness observations from IS6 drill holes, all drill holes from ARISE, SIPEX and SIPEX-II, floe scale and regional scale LiDAR, and ASPeCt observations in the region of SIPEX-II flight 22. The grouping of in situ observations at the thinner end of the sea-ice thickness distribution is a strong reflection of sampling bias, which may be primarily due to logistical constraints on sampling efforts. Using LiDAR-based estimates of sea-ice thickness, mean values for the SIPEX-II region should be in the 3 m to 4 m range, which corresponds with values suggested by Williams et al. (2014b).

4.8.1 Conclusions

Using a floe-scale validation study as a foundation, this study derives sea-ice thickness and draft estimates from high resolution altimetry, and compares the results with in situ

[7] https://github.com/adamsteer/phd-notebooks/blob/master/Snow_model_tinkering.ipynb, accessed 13 May 2016

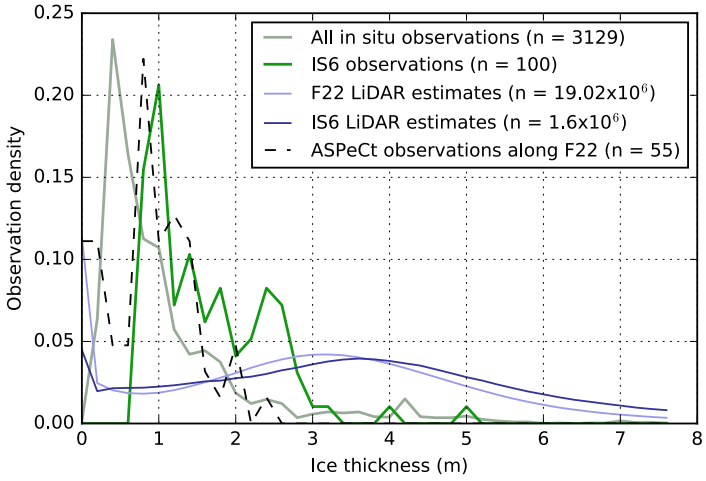

Figure 4.26: Density functions for ice thickness from in situ observations at floe scale (IS6) and regional scale (all East Antarctic drill holes), ASPeCt observations and airborne LiDAR at the floe scale (IS6) and regional scale(F22).

observations at the floe scale, and at a regional scale. Using the LiDAR-based results as a guide, the sea-ice thickness in the SIPEX-II region is under-estimated by close to 50% if only ASPeCt and in situ observations are used to characterise the region.

A qualitative comparison of ice thickness derived from airborne LiDAR shows that at sub-floe resolutions, the ice-ocean interface estimated using altimetry is overly rough, which affects the use of these data as inputs to models of ice-ocean interaction. However, at a floe scale, or at the scale of 'ridge systems' and 'smooth ice', LiDAR based estimates of under-ice topography are reasonable, with the caveat that ice keels are generally wider than ridges, and snow dunes are reflected in under-ice topography. An appropriate segmentation-and-smoothing algorithm for the modelled ice-ocean interface may resolve these issues in future work.

Looking more closely at relationships between surface and under-ice features, the idea that ice draft can be estimated from freeboard using a scalar multiplier (the ratio R) is tested. For the ice examined at IS6, there are many choices of draft for a given freeboard observation. Further, segmenting the ice into rough and smooth regions using surface roughness, there is no improvement in the strength of R as method for deriving ice draft. While the snow modelling methods used in this study are imperfect, they allow for a point-by-point estimation of ice characteristics, and provide a means by which draft (and sea-ice thickness) estimation can be improved in future works by appropriate modification of snow models.

Finally, the importance of a cohesive, coordinated field sampling campaign using multiple instruments cannot be emphasised enough. This study clearly shows the benefit of a systematic approach to operating instruments on, above and under ice, and using them

all as a part of a broader ice measurement system. It shows that drill holes are not a dying art - but clearly a drilling strategy needs to be appropriate to the broader sampling strategy. For example, where an airborne package and under-ice package are collecting data, and the means on the surface exist to accurately position any sample site (e.g. Steer et al., 2014), it is potentially far more valuable to disperse 100 drill holes around a sampling site than to drill them all in one straight line. In this study, the limited set of distributed, well positioned drill holes provided a critical check on the methods used to derive total freeboards and ice thickness from the APPLS LiDAR. Transect lines offer a validation tool along one dimension but give no means for examining, for example, across-swath slope in LiDAR observations. Using a widely distributed set of 'control' points provides validation in both planar dimensions, a blind spot in existing validation methods for remote sensing of sea ice. The toolkit required to undertake this type of validation exercise allows for accurate positioning and co-registration of any activities on, or under an ice floe. It represents a powerful foundation for merging diverse datasets and finding relationships between physical, biological and chemical interactions at the floe scale.

In summary, the work described here shows how a coherent and coordinated effort to capture observations on, over and under the ice along with ancillary spatial data has allowed a rigorous examination of sea-ice properties at multiple scales. It shows how examining small scale properties in detail can inform the estimation of sea ice properties at larger scales, and how multiple sensor approaches can be used to examine sea ice in three dimensions. Antarctic sea ice continues to offer challenges for earth systems science, and these approaches are a step toward a new understanding how best to evaluate the properties of sea ice on the Southern Ocean.

Chapter 5 Discussion and conclusions

5.1 Project discussion

Current understanding of the sea-ice thickness distribution and its role in the Earth system relies on sparse observations (e.g. Worby et al., 2008a; Kurtz et al., 2012), missing much of the detailed variability that exists in the ice pack. This project has provided an intrinsically valuable, and extremely rare glimpse into high-resolution sea ice physical characteristics off East Antarctica using airborne LiDAR, validated with in situ observations and measurements of ice draft by AUV-based sonar.

The primary aim of the APPLS project was to validate estimates of East Antarctic sea ice elevations derived from satellite-based altimeters, including the retired ICESat mission and the current CryoSat-2 mission. Given timing and logistics issues outlined in Worby et al. (2011), achieving a meaningful comparison with ICESat observations was problematic. This work provides a technical basis for analysis of APPLS observations which took place after the launch of CryoSat-2 for comparative purposes, where coincident on-ice observations exist. In an era of increasingly more detailed satellite altimetry, the principles (and pitfalls) of sea ice thickness estimation from altimetry at high resolutions shown here will be valuable guides for choosing appropriate ice thickness modelling parameters.

This work was focussed on extracting and validating high resolution ice thickness observations from the APPLS data, which required the following set of objectives to be addressed:

- Understand sea ice physical processes in the Earth system and the need for in situ and high resolution remotely sensed observations (Chapter 1)
- Understand processes for snow depth and sea-ice thickness estimation from altimetry, and effects of scale on analytical outcomes (Chapter 2)
- Understanding the uncertainties associated with the airborne APPLS system, and their propagation to geophysical quantities (Chapter 3)
- Converting raw observed data into meaningful validated geophysical parameters, and providing interpretation of these novel data (Chapter 4)

The work required to meet these project objectives has led to a detailed examination of snow depth models and the relationship between surface and under-ice topography for the APPLS survey region, incorporating unique in situ observations from the ARISE, SIPEX and SIPEX-II research voyages (Chapter 2). It has also provided an improved understanding of how system design and flight planning affect final results (Chapter 3), which leads to an ability to determine an a priori uncertainty for every LiDAR point captured by the APPLS system. In turn, this allows a rigorous a priori estimation of uncertainty for every sea-ice thickness or snow depth estimate which is derived from the APPLS system. These advances are used collectively in Chapter 4, where APPLS LiDAR observations are used to estimate snow depth and sea ice thickness for specific region of sea ice off East Antarctica. The hydrostatic model for estimating ice thickness from LiDAR points (Wadhams et al., 1992) is applied and validated using coincident in situ and AUV observations. The model is extended to make a qualitative comparison of regional-scale ice thickness estimates from LiDAR and ship based ASPeCt observations. Finally, the potential benefits of 3D photogrammetry using SfM (Snavely et al., 2006) as a tool for observing and improving understanding of sea ice is shown.

Using a validated model for estimating sea-ice thickness using airborne LiDAR allowed a broader view of ice conditions in the vicinity of in situ observations on the SIPEX II voyage. This demonstrated that in situ observations, while accurate, are planned and executed in a fashion which introduces a sampling bias to the record. This has substantial implications for current understanding of sea-ice thickness based on the use of the in situ record as a validation tool, which are discussed below.

5.2 Implications for estimation of sea ice thickness from altimetry

A key message from this study is that the record of Antarctic sea-ice thickness from in situ and ASPeCt observations capture only one tail of the complete distribution. This conclusion is arrived at after validation of the methods used in this study to estimate sea-ice thickness from altimetry, and then applying them to a wider (albeit small) region of sea ice. Figure 4.26 shows that most sea ice for the SIPEX-II region was around 3 m thick, a value consistent with Williams et al. (2014b). Observations from drill holes and the ASPeCt program show a peak at around 1 m, but Figure 4.13 shows clearly that for at least the site studied here, drill holes only capture the least-deformed (and therefore among the thinnest) ice at the sampling site.

Remote sensing efforts have traditionally used in situ observations as standards for calibration (e.g. Kurtz et al., 2012), aiming for agreement at regional scales (e.g. AMSR-E pixels, or ICESat analysis scales). This study shows that doing so may result in a substantial under-estimation of ice thickness. While the community necessarily looks to scales of observation consistent with satellite data collection capabilities (e.g. Ozsoy-Cicek et al., 2013; Weissling et al., 2011), the detailed analysis of small scale datasets using appropriate combinations of in situ and remotely sensed observations is a critical tool for guiding larger-scale efforts at estimating sea-ice thickness.

5.2.1 Geophysical implications for modelling the ice/ocean interface from altimetry

The data produced from observational studies are essential as inputs to models of sea ice in the Earth system. How ice thickness and under-ice topography is parameterised will affect ice/ocean/atmospheric interactions in model systems (e.g. Martin et al., 2016; McPhee, 2002; Skyllingstad et al., 2003). With increased resolution of observations, the shape and distribution of modelled ice features need to be considered. Skyllingstad et al. (2003) investigated the role of keels in thermal heat flux to the underside of the ice. A key implication from their study was that smaller keels may result in a greater heat flux to the underside of sea-ice during the spring melt season. While large keels contribute to the movement of relatively warm water to the underside of sea ice, the turbulent heat flux is localised in the lee of the keel. For shorter keels, the motion of ice and ocean currents are less coupled and turbulent heat fluxes to the underside of the ice are spread over a wider area.

Figure 4.14 shows that spurious features (e.g. snow dune shaped keels) are prevalent in high resolution draft estimates derived from altimetry, and ice keels modelled below surface ridges are generally deeper and narrower than keels observed by AUV-based sonar. These factors potentially affect derived sea-ice thickness and roughness. Martin et al. (2016) suggest that the orientation and spatial frequency of ridge keels is also important in modelling the interactions between ocean and ice, with keel orientation affecting parameterised skin drag at the ice-ocean interface. How well these models translate to reality is uncertain, as the authors note that in situ ice ridges may not conform to idealised geometry used for modelling since the spatial distribution of keels beneath sea ice is poorly understood.

5.2.2 Operational implications for modelling the ice/ocean interface from altimetry

The timely collection of high resolution sea-ice topography observations will eventually find applications in ship guidance and other operations in the pack ice zone. In a hypothetical scenario where LiDAR equipped drones are used for ice reconnaissance and observations are processed in real time (e.g. Skaloud et al., 2010b), the choice of model parameters used to generate ice thickness and draft from altimetry will impact operational decisions in the field. Under-estimating snow depth on level ice and underestimating the level ice thickness will impede the passage of ships, and are both outcomes of choosing inappropriate parameters for estimating snow depth and ice thickness from altimetry.

Large-scale ice thickness estimates are in use as an operational tool in the Arctic, based on SAR imagery and interpretation by experienced analysts (e.g. http://www.polarview.org/services/sea-ice-services/, accessed 2 May 2016). Automated ice thickness estimates derived from satellite-based instruments (e.g. CryoSAT-2, the

upcoming ICESat-2) are an operational possibility that will need to carefully consider how snow and sea-thickness are modelled, especially in regions where validation data are sparse (e.g. Rinne and Similä, 2016). Most importantly, systems for operational sea-ice thickness estimation must be flexible and readily upgradeable, as new methods for estimating snow depth and ice density distributions are realised.

5.2.3 On the relationship between total freeboard and ice thickness - *R*

In situ observations of East Antarctic sea ice used in this study do not show a strong relationship between total freeboard and ice draft. This is a marked contrast to work in the Arctic (Alexandrov et al., 2010; Doble et al., 2011) and larger scale views of Antarctic sea ice (Ozsoy-Cicek et al., 2013). Using total freeboard from LiDAR and draft from AUV observations, Figure 4.15 shows a linear trend with a strong correlation but there is a wide range of possible drafts associated with every total freeboard observation. A clear relationship between ice topography and ice draft only exists in certain cases - where ice is level and snow depth is constant, or where ice is deformed and snow cover minimal. The work presented in Chapters 2 and 4 along with in situ studies from recent voyages (e.g. Toyota et al., 2016; Worby et al., 2011) show that for east Antarctic sea ice, these conditions are the exception rather than the rule.

Computing an R for each ice type (e.g. Doble et al., 2011; Geiger et al., 2015) is a possible way forward for multi-instrument platforms, which requires a robust classification method using a combination of imagery and elevation observations to assess ice characteristics for a given region. This may be a future direction for APPLS and IceBridge style campaigns, but the impact of snow variability should not be ignored. Chapter 2 reaffirms earlier works which show that snow depth accounts for substantial proportion of ice thickness (and therefore draft) modelled using the assumption of hydrostatic equilibrium (e.g. Kwok and Cunningham, 2008; Spreen et al., 2006). Given that the snow component of an ice thickness signal is highly variable, it may be less valuable to try and refine an R, or set of R values (Geiger et al., 2015, e.g.). Future efforts aimed at automated classification of ice features in altimetry observations (e.g. Petty et al., 2015) may show that a set of R values corresponding to ice classes are reasonable, without the overhead of estimating snow depth. However, a more realistic approach may be modelling snow depth using a snow radar (e.g. Galin et al., 2012; Kwok and Maksym, 2014) along with empirical models to determine a workable set of parameters for ice thickness estimation incorporating a variable snow depth.

5.3 Choices in snow depth and ice density

For altimetry-based studies, there are a number of approaches to estimating the distribution of snow on sea ice. Doble et al. (2011) model snow at a constant depth for all total freeboard observations. Another approach is to apply an estimate based on passive microwave imaging (e.g. AMSR-E) (Kurtz et al., 2012; Markus et al., 2011),

which is essentially the same as using a single snow depth for surveys covering less than a single AMSR-E pixel (25 km × 25 km). Using coincident radar observations of snow depth recognises snow as a spatially-variable parameter but acts in a one-dimensional sense, since all off-nadir observations have the same depth value applied (Kwok and Maksym, 2014). The approach of using an empirical relationship derived from in situ observations to model snow (Yi et al., 2011; Worby et al., 2011; Ozsoy-Cicek et al., 2013), allows snow depth to vary at each point in three dimensional space, but overestimates snow depth for sea ice where the ice freeboard makes up a substantial component of the total freeboard signal. Using Equation 1.1 to convert altimetry observations into ice thickness estimates dictates that snow depth and ice density are essentially tune-able parameters informed by available in situ observations. Chapter 4 shows how the choice of input ice density can depend on the method used to estimate snow depth, and decisions about these parameters are critical to deriving consistent thickness distributions. A primary issue for the empirical modelling approach is that snow depth is potentially overestimated on ridge systems, which leads to assigning an artificially high ice density value in order to obtain realistic sea-ice thickness estimates at a floe scale. With this in mind, a method for reducing snow depth on deformed ice is demonstrated below.

5.3.1 A snow model to reduce snow depth over ice ridges

Figure 5.1 shows how a choice of three different snow modelling strategies affect the choice of ice density which is required for altimetry-based ice draft estimates to match AUV observations of ice draft. Figure 5.1a uses the mean snow depth for all SIPEX-II observations (N=447), Figure 5.1b uses the snow model derived from all East Antarctic observations (EA model, as for the analyses in Chapter 4), and Figure 5.1c uses a modified EA model, described below.

Given the very similar ice densities shown in Figure 5.1a and c, it appears that using the mean snow value for a given region would arrive at a realistic draft with a realistic ice density value. However, Figure 5.2 shows that using a mean snow value is less useful at smaller-than-regional scales, with ice draft venturing above sea level in the final 40 m of the transect. The East Antarctic model (EA model) used in Chapter 4 gives the closest result to in situ observations of ice draft, with the SIPEX snow model leading to underestimates of ice thickness.

A modified EA snow model was developed to investigate the effect of thinning snow only where ice is 'rough', and ridge systems with high ice freeboards are likely to be present. Where surface topography is 'rough', snow depth above the mean total freeboard is thinned as a proportion of the total freeboard, such that at maximum total freeboard, $Z_s = 0$[1]. Figure 5.3a shows the difference between snow modelled using the EA relationship and its modified counterpart. Figure 5.3b shows the derived 'multiplier' for snow depth. In rough

[1]https://github.com/adamsteer/phd-notebooks/blob/master/Snow_model_tinkering.ipynb (accessed 13 May 2016)

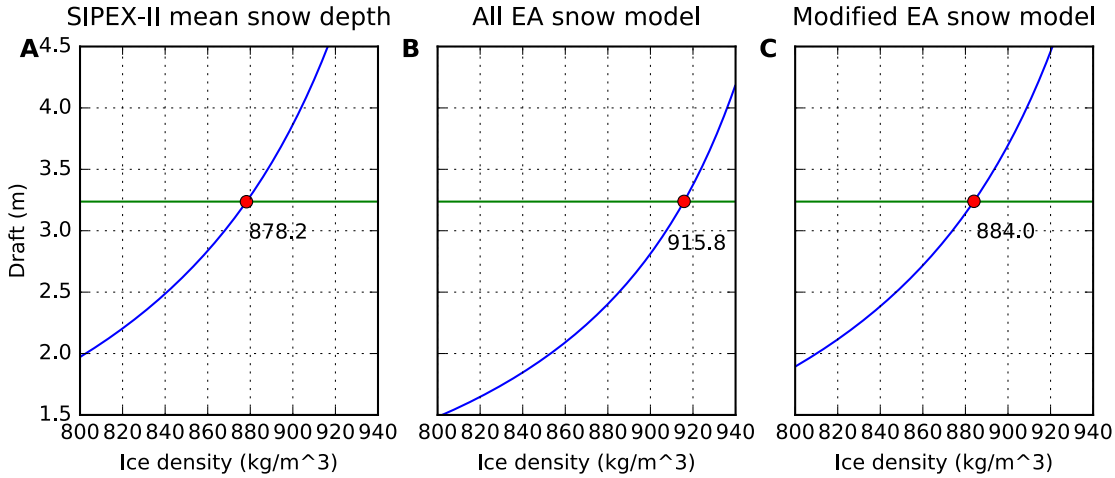

Figure 5.1: Appropriate ice densities for snow depth models in order to match AUV draft observations at SIPEX-II IS6. A: The required ice density to match AUV draft using the mean snow depth from SIPEX II (0.27 m) for all total freeboard observations; C: as for A, with an all East Antarctic (EA) snow model is applied; and C: using a modified EA snow model which thins snow over deformed ice above the mean total freeboard

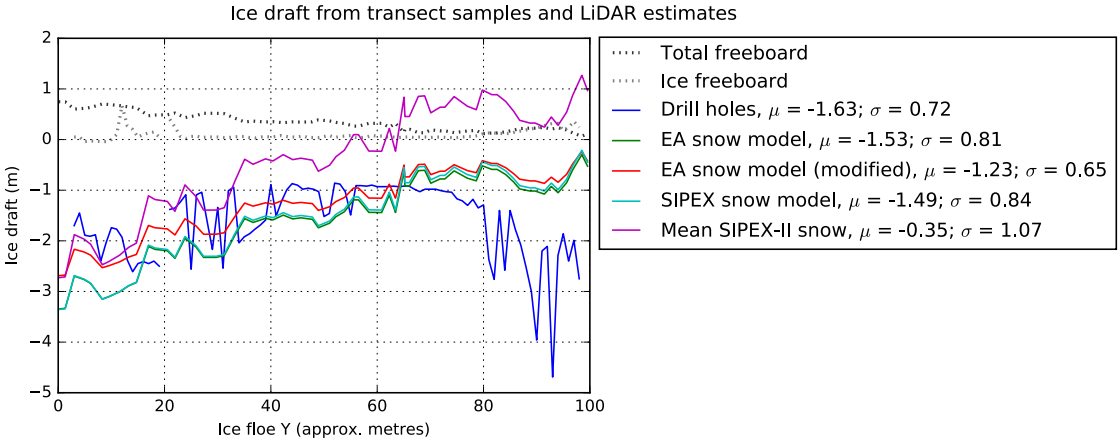

Figure 5.2: Impact on modelled ice draft of snow model and ice density choice

regions, snow depth is progressively thinned. Where total freeboard peaks, up to 2.9 m of snow is removed. Since the transect line (red) lies entirely on 'smooth' ice (white in Figure 5.3a, green in b), the thresholds for 'roughness' and the level above which snow would be modified were adjusted to ensure that part of the transect line would be affected, and the effects of the modified snow model can be visualised alongside in situ observations. Figure 5.4 shows the resulting snow depths, after the first 20 m of transect were classified as 'rough'.

The reduction in modelled snow depth is clear in the first 20 m of Figure 5.4, where deep snow in a ridge systems is thinned by the modified EA model. Figure 5.5 shows resulting drafts using the standard and modified EA snow models. This shows how ice thickness is artificially (and erroneously) concentrated in ridge systems if the approach shown here is

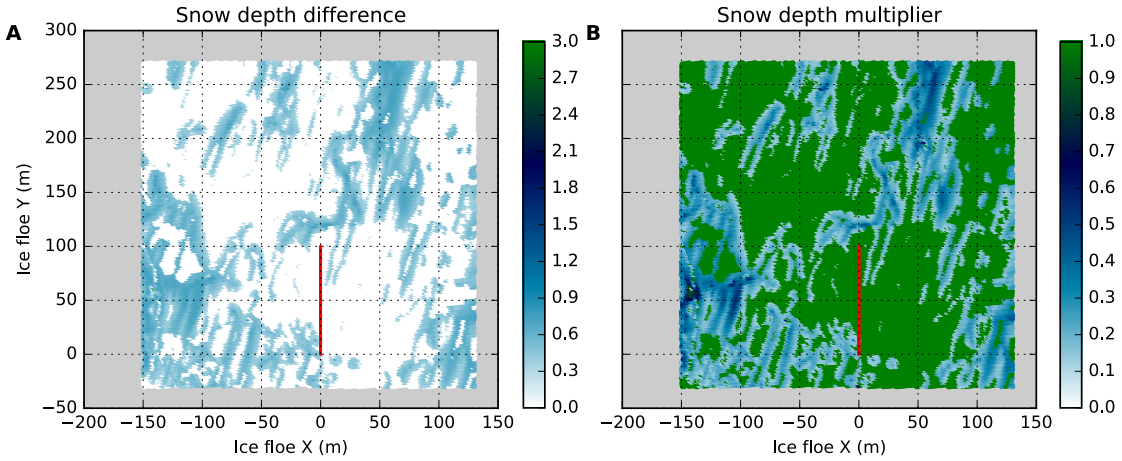

Figure 5.3: Snow distribution difference between EA and modified EA snow models. A: the difference between snow estimated using the EA model and the modified EA model (colour scale in metres); B:the distribution of snow model scaling factors (colour scale showing snow depth multiplier). The red vertical line on each panel shows the position of the 100 m drilled transect line.

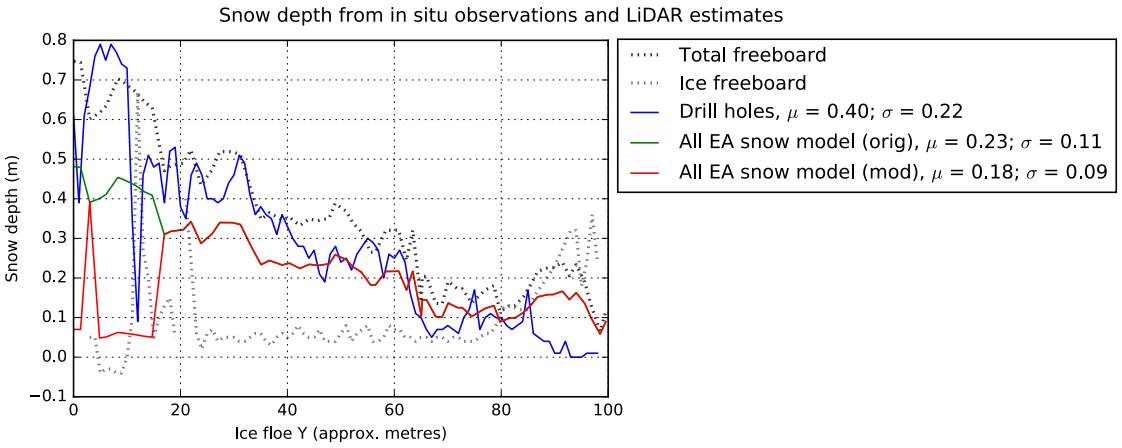

Figure 5.4: Modified snow depths after classifying the first 20 m of the IS6 transect as 'rough' ice.

used to thin snow over ridges. Given that all methods shown in this figure produce near identical mean draft at a floe scale, the analyst essentially faces a choice of scale - is the priority to investigate sea-ice features at the regional, floe, or sub-floe scales? This decision will ultimately guide the type of snow model used in the derivation of ice thickness from altimetry.

A substantial issue for this project is that the only information on snow depth is derived from in situ transect lines. While these data are valuable for validation exercises, Figure 4.13 shows that they may not be representative of the entire floe. Intensive snow depth surveys were carried out over 100 × 100 m areas of sea ice adjacent to transect lines on SIPEX-II (e.g. Williams et al., 2013), but whether these observations are sufficient

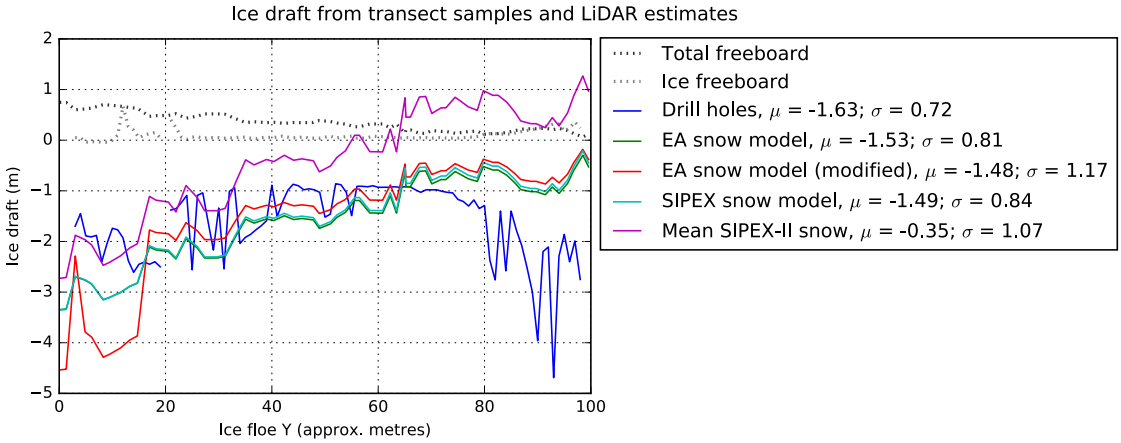

Figure 5.5: Modified ice draft after classifying the first 20 m of the IS6 transect as 'rough' ice.

to characterise the snow depth distribution of an entire floe is subject to future analysis. Answering the questions 'what is the snow depth distribution across an entire ice floe?', and 'can snow depth distributions be characterised using surface features?' will assist greatly in determining appropriate strategies for modelling sea ice thickness from altimetry.

5.3.2 Ice density choices

Choosing an appropriate ice density is another challenge. Applying the observed range from $800\,\mathrm{kg\,m^3}$ to $930\,\mathrm{kg\,m^3}$ results in a range of approximately 2.5 m of ice thickness using Equation 1.1. Density observations are extremely sparse (e.g. Hutchings et al., 2015; Timco and Frederking, 1996; Price et al., 2014), and provide no information on the spatial variability of sea-ice density. In Chapter 4 it was possible to derive a suitable density for a given snow model using AUV observations of ice draft as a guide. These opportunities are rare - analysis of airborne or satellite-based altimetry is typically based on a density parameter with no in situ observations to act as constraints. Given recent work on the assumptions of isostasy at small scales (Geiger et al., 2015), a set of key questions for the estimation of an Antarctic sea-ice thickness distribution should be 'what is the sea ice density distribution?'; 'are identifiable features on the ice surface associated with different densities?'; and 'over what scale does sea-ice density vary?'. For the present, the best strategy appears to be the use of a consistent density parameter. While this approach may bias observations, the bias is applied to all ice thickness estimates and the introduced bias can be understood and corrected as more is understood about the distribution of Antarctic sea-ice density.

5.4 Observing Antarctic sea ice at sub-floe scales

The understanding of sea-ice properties at metre scales is a worthwhile endeavour on its own, as Chapters 2 and 4 have shown. Further, the evidence presented here shows that in situ and remotely-sensed observations the scale of metres, or tens of metres, are an

appropriate for describing sea ice variability. However, given the area of sea ice on the southern ocean, averaging observations to broader scales has been a function of observation resolution. For example, ASPeCt observations are gridded to 5 degree cells because there are insufficient observations to populate smaller grid cells in a circumpolar map (Worby et al., 2008b). Passive microwave snow depths are collected at 25 km × 25 km pixels - so sea-ice properties are averaged to match (Kurtz et al., 2012).

Modern methods of investigating the optical properties of, and and biomass in sea ice operate at sub-floe scales. These also collect spatial data which can be used to related to surface observations from airborne LiDAR and imagery using the floe-scale georeferencing systems described in this thesis. For an example, ROV observations of under-ice light availability and biomass (e.g Katlein et al., 2014, 2015) could be coregistered with surface properties and modelled sea ice properties, allowing any relationships identified at the metre scale to be validated and then extrapolated over regions too large to be surveyed using current under-ice vehicles. In turn, these analyses could help to shed new light on the state of the Antarctic winter ecosystem.

Computation of sub floe scale sea-ice observations at a circumpolar extent may appear to be an impractical task. However, to add some perspective, 12.5 km grid cells gives 128 000 data points over $20 \times 10^2\,km^2$, approximating the area of southern ocean covered by sea ice at maximum extent (Reid et al., 2015). This thesis required processing of datasets two orders of magnitude larger, and modern computing facilities are capable of tracking many billions of datapoints in space and time (e.g Kool et al., 2015). Increasing resolution of sea ice observation to the sub-floe (tens-of-metres) scale is computationally feasible (200×10^9 points at 0.01 km cells over 20×10^6 km) but requires observations of sea-ice variability at those scales - and an understanding of how sea ice varies over broad regions at those scales. As more data are collected at the scales of observations presented here, and the analysis of observations at these scales matures, unforeseen opportunities for unpicking biogeophysical sea-ice properties will present themselves.

5.4.1 Applying new strategies for in situ observation

The SIPEX II ice floe survey described in Chapter 4 was critical for this project. Without the local coordinate frame established using the total station, and its ties to an Earth Centred, Earth Fixed reference frame, the co-registration of AUV and airborne datasets would have been practically impossible. Essentially every in situ dataset collected on the voyage can be located within a local coordinate frame which is relevant to its sampling site, and then related other datasets using a geographic reference frame. From this, relationships between ice thickness, available light, in-ice and under-ice biomass, and the structure of the ice itself can be investigated.

While in situ measurements of sea-ice properties are not perfect, they form a key tool in the interpretation of airborne observations. Chapter 2 shows that the collection of

in situ measurements is critical to deriving methods for estimating sea-ice properties from airborne instrumentation. Chapter 4 shows that in situ observations are generally accurate, but do not necessarily adequately characterise the sea-ice regime they are observed within. In general, there are too few observations on a limited range of ice types. Simply adding to the volume of in situ observations is a valuable exercise, but strategic sample collection in terms of regions, seasons and ice types would make a highly valuable contribution. Density measurements in particular are missing - it is currently impossible to determine the spatial variability of sea-ice density, or derive any relationships between density and other observable parameters which would assist in the estimation of sea-ice thickness from altimetry,

Williams et al. (2014b) question the value of in situ sampling of sea-ice thickness, but this study makes a strong case for updating sampling methods rather than dismissing them. In combination with a floe based surveying system (e.g. Steer et al., 2014), the geometry of drill holes can be vastly improved and samples can be collected on a diverse set of surface ice types. With a small borehole logging system - as simple as a mini video camera on a pole which observes a tape measure along with ice it passes as it descends - drill hole ice thickness and ice composition at sampling sites can be easily verified, and related to coincident (in space and time) physical and biological observations.

Collecting snow distributions using dense, geolocated in situ sampling methods (e.g Williams et al., 2013) is an extremely useful exercise. However, for work published to date it carries the same sampling bias as existing in situ observations - in that ridge systems are generally ignored. Snow depth sampling needs to occur over wider areas and on different ice types. This is highlighted by the short example presented in Section 5.3.1 which attempts to modify the snow distribution over regions of deformed ice. Observations of snow depths at appropriate resolutions over deformed ice are required in order to refine snow depths derived from altimetry over these regions of pack ice.

5.4.2 Choice of airborne instrument platforms

The comparison between fixed-wing deployment and helicopter deployment in Chapter 3 clearly shows how the mounting system used by the APPLS system was the source of substantial degradation in data quality. However, mounting ship-based campaigns clearly offers deployment flexibility that is not possible using piloted fixed-wing aircraft. The IceBridge program, for example, is limited to observing sea ice when long range flight conditions are optimal. Doble et al. (2011) also point to noise in LiDAR point clouds as a data quality issue from fixed-wing aircraft deployment.

While ship based aircraft deployment has its own logistical issues, there is an advantage in being able to fly impromptu surveys with coincident in situ observations in locations and at times where a piloted fixed-wing overflight is unlikely - for example, off East Antarctica in late autumn or early spring. Whichever shape they take, future deployments of LiDAR

and imaging equipment for airborne surveys need to ensure that the instrument package is isolated from airframe vibration and the relationship between all instruments is rigid. The combination of instrument package and flight plane needs to also be appropriate for the desired spatial resolution and coverage. Future deployments should also take advantage of developments in instrumentation: the addition of coincident snow depth radar systems (e.g. Kwok and Maksym, 2014); newer LiDAR instruments (for example the photon counting instrument tested by Farrell et al. (2011), or multispectral instruments described in (Glennie et al., 2013)); and imaging capabilities for a wider range of the electromagnetic spectrum, for example the addition of a near-infrared camera (Yang et al., 2014). Of course, instrument ensembles are constrained by aircraft capability, logistics and science priorities.

LiDAR datasets are clearly useful, but need to be carefully controlled and understood. Rigorous analysis and testing of the LiDAR instrument deployed in this study guided the choice of algorithm used to define a sea level reference surface. Here, the median of a set of points is used to reflect the observation that LiDAR elevations scatter evenly about a desired target surface. The knowledge gained in the analysis of the instrument package also enabled the ability to rigorously estimate the uncertainty surrounding sea-ice thickness estimates.

The use of small remotely piloted aircraft systems (RPAS, or drones) is an approach that is likely to gain popularity (e.g. Nolan, 2014; Nolan et al., 2015; Williams et al., 2016). Smaller airborne sensors are cheap, relatively easy to deploy from small platforms and are a proven method of constructing accurate models of the world (e.g. Turner et al., 2012; Fonstad et al., 2013). However, endurance and the ability to carry relatively heavy instrumentation is a substantial issue for RPAS. The optimal system for airborne surveying of sea ice is a mix of large scale, piloted fixed-wing aircraft surveys, long range piloted aircraft deployed from ships, and RPAS for floe scale surveys.

With the advent of mature systems for generating elevation models from unstructured image collections, the question of 'why fly large scale LiDAR at all?' is relevant - given the costs of instrumentation, fuel and pilots. In this work, a small set of imagery was processed to derive elevation models (Chapter 4). For a survey which was never designed to generate elevation models from imagery, the method works well. Altering flight planning to collect an image set more suited to 3D reconstruction would allow the production of highly detailed floe-scale models of sea ice. However, this presents a sampling dilemma: is it more desirable to sample a number of ice 'patches', or collect long strip flights? 3D photogrammetry is more suited to the former, while a LiDAR system the latter. Both systems can potentially work together, providing independent models of the ice surface at different resolutions and greater detail where required.

The choice of aircraft and instrument platform is one aspect of producing realistic observations from airborne systems. Substantial field work is still required to inform remotely-sensed sea ice attributes. The work in Chapter 2 is only scratching the surface,

with incredibly sparse observations used to estimate snow properties over vast regions of a highly heterogeneous environment.

5.4.3 Future directions: making better use of available data

It is widely recognised that densely-spaced data collected by laser scanners, snow radar instruments, or derived from imagery are difficult to work with and integrate with other data sources. Systems such as Terrasolid are expensive, and difficult to learn to use. The ASPRS .LAS format is limited, since it cannot store additional fields like point uncertainty, or a field for ice thickness, or snow depth. Emerging standards for point cloud storage and interoperability point to a Hierarchical Data Format (HDF5) based system, which would allow a vast number of extra fields and greatly ease interoperability with imagery and other data sources (e.g. SPDLib, http://www.spdlib.org/doku.php, accessed 10 May 2016). This work did not seek to use HDF as a data model for point cloud and image storage, but future efforts should investigate the use of more interoperable data types.

This research could have been improved by the addition of classified and more rigorously georeferenced imagery. For example, the reference surface derivation in Chapter 4 could have been re-cast as a method for collecting points inside polygons defined by a 'water' class in imagery (e.g. Onana et al., 2013). Sea ice image rectification, mosaicking and classification is an intrinsically valuable task (e.g. Hutchings et al., 2012; Toyota et al., 2011; Steer et al., 2008) - and will also assist in the interpretation of LiDAR observations. The 'water points? isolated from LiDAR swaths are also potentially useful as a means to examine dynamic sea surface topography. Doing so would also assist in validation, especially in the swell-affected marginal ice zone.

Identifying individual features on sea ice and investigating their properties in detail (e.g. Petty et al., 2015) is potentially achievable with further analysis of the APPLS dataset. Future analysis of high resolution LiDAR and imagery should focus on feature extraction and defining properties of sea ice classes at the floe, sub-floe and feature scale. This approach should also guide in situ data collection, allowing analysis of which ice types are require more detailed sampling. Ultimately, the in situ sampling of diverse ice features is required to fully characterise and validate ice features identified in remotely-sensed observations.

5.5 Conclusions

In summary, this work provides a detailed analysis of biases present in methods for estimating sea ice thickness from APPLS and equivalent altimetry; the first estimates of the sea-ice thickness distribution at metre resolution over whole floe and multiple-floe scales; and a clear demonstration of likely biases present in the in situ record of East Antarctic sea-ice thickness.

For a small region of Antarctic sea ice, this project was able to visualise and provide a quantitative analysis of how modelling ice thickness from altimetry compares with the actual under-ice topography. At sub-floe scales, modelling ice thickness from altimetry gives a reasonable approximation of keel shapes and depths, but adds topography to the underside of the ice that is dependent on snow dunes. This is a potential issue for future analysts seeking to model ice/ocean interaction. At whole-of-floe scales, it confirms earlier work on scale effects (e.g. Doble et al., 2011; Ozsoy-Cicek et al., 2013), with modelled ice draft closely approximating observed values as the field-of-view increases. The analysis here shows that using a freeboard to ice draft ratio (R) is an unreliable method, as is the use of a single snow depth across an entire floe.

Using a set of models tuned to match LiDAR-derived ice thickness and freeboard with in situ observations, this study found that the mean ice thickness in the region examined was substantially underestimated in drill hole and ASPeCt observation data. For drill holes, this study shows that there were no methodological issues in the physical sampling; however the experiment suffered a significant sampling bias. It is clear that for SIPEX-II IS6, drill holes on the transect line are placed in the thinnest region of an otherwise heavily deformed, very thick ice floe. The off-transect drill hole set provided a small window into the rest of the IS6 floe, but still record relatively thin ice compared to AUV draft observations. LiDAR derived observations of ice thickness support the assertion of Williams et al. (2014b) that Antarctic pack ice is thicker than in situ observations suggest. This study adds evidence to an argument that the in situ record may describe only one tail of the Antarctic sea-ice thickness distribution, but further research is required to fully explore this issue.

Shedding light on the mechanics of sea-ice thickness modelling will assist in answering this question. Analysts are faced with multiple choices in the derivation of a sea-ice thickness and draft from airborne or satellite-based altimetry. Each choice has an impact on the ice thickness outcome. Until more information comes to light that defines the distribution of snow depths on Antarctic sea ice, and the distribution of sea-ice densities, choosing model parameters and deriving an ice thickness from altimeter observations introduces a bias either toward deeper snow and thinner ice, or thinner snow with thicker ice and very deep ridge keels. However, this study has provided insight into the modelling approach as well as open source tools to analyse and interpret decisions about ice thickness model parameters. Finally, the study has shown how a coordinated effort to collect and analyse in situ and remotely-sensed observations together can act as a powerful validation tool. While the remote sensing technologies used here are powerful tools in their own right, their power is only fully utilised when they can be coordinated and validated with appropriate in situ observations and spatial data.

The estimation of sea ice thickness at sub-floe scales using airborne LiDAR and imagery collected by the APPLS package off East Antarctica is not only possible, but has been validated using independent datasets at the floe scale and in three dimensions. While subject to caveats about choices for snow depth and ice density parameters, the work

shown in this study provides the basis for further unlocking the entire APPLS LiDAR collection, covering several hundred nautical miles of sea ice over the period 2007-2012. In doing so, this study shows how in situ observations of thick, deformed sea ice may be biased toward relatively thinner ice in these regions, opening the question of whether in situ observations should be used as the standard for validation of sea ice model outputs or estimates of sea-ice thickness from remote sensing platforms. Finally, this work represents an incremental advance in further understanding the complex role that sea ice plays across three dimensions and at multiple scales in the dynamic Earth climate system.

References

Abdalati, W., Zwally, H. J., Bindschadler, R., Csatho, B., Farrell, S. L., Fricker, H. A., Harding, D., Kwok, R., Lefsky, M., Markus, T., Marshak, A., Neumann, T., Palm, S., Schutz, B., Smith, B., Spinhirne, J., and Webb, C., 2010: The ICESat-2 laser altimetry mission. *Proceedings of the IEEE*, **98(5)**, 735–751.

Adolphs, U., 1998: Ice thickness variability, isostatic balance and potential for snow ice formation on ice floes in the south polar Pacific Ocean. *Journal of Geophysical Research*, **103(C11)**, 24675–24692.

Alexandrov, V., Sandven, S., Wahlin, J., and Johannessen, O. M., 2010: The relation between sea ice thickness and freeboard in the Arctic. *Cryosphere*, **4(3)**, 373–380.

Allison, I., 1981: Antarctic sea ice growth and oceanic heat flux. *Sea level, ice and climatic change (Proceedings of the Canberra Symposium, December 1979)*, no. 131, 161–170.

Altamimi, Z., Collilieux, X., and Métivier, L., 2011: ITRF2008: An improved solution of the international terrestrial reference frame. *Journal of Geodesy*, **85(8)**, 457–473.

Atkinson, A., Siegel, V., Pakhomov, E. A., and Rothery, P., 2004: Long-term decline in krill stock and increase in salps within the Southern Ocean. *Nature*, **432**, 100–103.

Baltsavias, E. P., 1999: Airborne laser scanning: Basic relations and formulas. *ISPRS Journal of Photogrammetry and Remote Sensing*, **54(2-3)**, 199–214.

Bennetts, L. G., Peter, M. a., Squire, V. a., and Meylan, M. H., 2010: A three-dimensional model of wave attenuation in the marginal ice zone. *Journal of Geophysical Research Oceans*, **115(C12)**, C12043.

Brodin, G. J., Cooper, J. A., and Stevens, J. R. A., 2005: Measuring the effect of helicopter rotors on GPS reception. *The Journal of Navigation*, **111(1123)**, 561–570.

Burman, H., 2000: *Calibration and Orientation of Airborne Image and Laser Scanner Data Using GPS and INS*. Ph.D. thesis, Royal Institute of Technology.

Castleden, N., 2004: First results from Virtual Reference Station (VRS) and Precise Point Positioning (PPP) GPS research at the Western Australian Centre for Geodesy. *Journal of Global Positioning Systems*, **3(1)**, 79–84.

Castleden, N., Hu, G. R., Abbey, D. A., Weihing, D., Ovstedal, O., and Earls, C. J., 2004: Recent results of long-range airborne kinematic GPS positioning research at the Western Australian Centre for Geodesy. *The 2004 International Symposium on GNSS/GPS*, no. December, 1–9.

Cavalieri, D. J., and Parkinson, C. L., 2008: Antarctic sea ice variability and trends, 19792006.

Cimoli, E., 2015: *Determining Snow Depth Distribution from Unmanned Aerial Vehicles and Digital Photogrammetry*. Ph.D. thesis, Technical University of Denmark.

Colombo, O. L., Brunker, S., Jones, G., Janssen, V., and Rizos, C., 2010: Wide-area, Sub-decimetre Positioning for Airborne LiDAR Surveys Using CORSnet-NSW. *The XXIV FIG International Congress 2010 'Facing the Challenges - Building the Capacity'*, **(April 2010)**, 11–16.

Colombo, O. L., Nasa, U., and Space, G., 1981: Kinematic Positioning of Buoys at Sea , with Potential Application to Deep-Sea Studies. *Test*, **(September)**, 1476–1484.

Comiso, J. C., Cavalieri, D. J., and Markus, T., 2003: Sea ice concentration, ice temperature, and snow depth using AMSR-E data. *IEEE Transactions on Geoscience and Remote Sensing*, **41(2)**, 243–252.

Connor, L. N., Laxon, S. W., Ridout, A. L., Krabill, W. B., and McAdoo, D. C., 2009: Comparison of Envisat radar and airborne laser altimeter measurements over Arctic sea ice. *Remote Sensing of Environment*, **113(3)**, 563–570.

Dalå, N., Forsberg, R., Keller, K., Skourup, H., Stenseng, L., and Hvidegaard, S., 2005: Airborne lidar measurements of sea ice north of Greenland and Ellesmere Island 2004. GreenICE/SITHOS/CryoGreen/a76 Projects - Final Report,. Tech. Rep. 1.

Doble, M. J., Skourup, H., Wadhams, P., and Geiger, C. A., 2011: The relation between Arctic sea ice surface elevation and draft : A case study using coincident AUV sonar and airborne scanning laser. *Journal of Geophysical Research*, **116**, 1–12.

Doutt, J. A., Frisk, G. V., and Martell, H., 1998: Determination of Distance Between a Moving Ship and Drifting Buoys to Centimeter-Level Accuracy at Sea Using L1 Phase GPS Receivers and Differential Moving-Base Kinematic Processing. *Proceedings of the 11th International Technical Meeting of the Satellite Division of The Institute of Navigation (ION GPS 1998)*, Nashville, TN, 1301–1306.

Drinkwater, M. R., Francis, R., Ratier, G., and Wingham, D. J., 2004: The European Space Agency's Earth Explorer Mission CryoSat: Measuring variability in the cryosphere. *Annals of Glaciology*, **39(August)**, 313–320.

Eckerstorfer, M., Solbo, S. A., and Malnes, E., 2015: Using 'Structure-from-Motion' Photogrammetry in Mapping Snow Avalanche Debris. *Wiener Schriften zur Geographie und Kartographie.*, **21(August)**.

Farrell, S. L., Markus, T., Kwok, R., and Connor, L., 2011: Laser altimetry sampling strategies over sea ice. *Annals of Glaciology*, **52(57)**, 69–76.

Fonstad, M. A., Dietrich, J. T., Courville, B. C., Jensen, J. L., and Carbonneau, P. E., 2013: Topographic structure from motion: A new development in photogrammetric measurement. *Earth Surface Processes and Landforms*, **38(4)**, 421–430.

Forsberg, R., Keller, K., and Jacobsen, S. M., 2002: Airborne Lidar Measurements for Cryosat Validation. *Geoscience and Remote Sensing Symposium, 2002. IGARSS '02. 2002 IEEE International*, vol. 00, 1756–1758.

Forsberg, R., and Skourup, H., 2005: Arctic Ocean gravity, geoid and sea-ice freeboard heights from ICESat and GRACE. *Geophysical Research Letters*, **32(21)**, L21502.

Galin, N., Worby, A., Markus, T., Leuschen, C., and Gogineni, P., 2012: Validation of airborne FMCW radar measurements of snow thickness over sea ice in antarctica. *IEEE Transactions on Geoscience and Remote Sensing*, **50(1)**, 3–12.

Gao, Y., and Chen, K., 2004: Performance Analysis of Precise Point Positioning Using Rea-Time Orbit and Clock Products. *Journal of Global Positioning Systems*, **3(1)**, 95–100.

Geiger, C., Wadhams, P., Müller, H.-R., Richter-Menge, J., Samluk, J., Deliberty, T., and Corradina, V., 2015: On the uncertainty of sea-ice isostasy. *Annals of Glaciology*, **56(69)**, 341–352.

Geng, J., Teferle, F. N., Meng, X., and Dodson, a. H., 2010: Kinematic precise point positioning at remote marine platforms. *GPS Solutions*, **14(4)**, 343–350.

Giles, K. A., Laxon, S. W., and Worby, A. P., 2008: Antarctic sea ice elevation from satellite radar altimetry. *Geophysical Research Letters*, **35**, 1–5.

Glennie, C., 2007: Rigorous 3D error analysis of kinematic scanning LIDAR systems. *Journal of Applied Geodesy*, **1**, 147–157.

Glennie, C. L., Carter, W. E., Shrestha, R. L., and Dietrich, W. E., 2013: Geodetic imaging with airborne LiDAR: the Earth's surface revealed. *Reports on Progress in Physics*, **76(8)**.

Gloersen, P., Campbell, W. J., Cavalieri, D. J., Comiso, J. C., Parkinson, C. L., and Zwally, H. J., 1993: Satellite passive microwave observations and analysis of Arctic and Antarctic sea ice , 1978-1987. *Annals of Glaciology*.

Goosse, H., and Fichefet, T., 1999: Importance of ice-ocean interactions for the global ocean circulation: A model study. *Journal of Geophysical Research*, **104(C10)**, 23337.

Granberg, H. B., and Lepparanta, M., 1999: Observation of ice ridging in the Weddell Sea. *Journal of Geophysical Research*, **104(Cll)**, 25735–25745.

Haine, T. W. N., Watson, A. J., Liddicoat, M. I., and Dickson, R. R., 1998: The flow of Antarctic bottom water to the southwest Indian Ocean estimated using CFCs. *Journal of Geophysical Research*, **103**.

Hardesty, M., Conner, D., Smith, C., and Terrell, W., 2004: The use of GPS tracking and guidance systems for the chicken little joint project's "Acoustic Week" flight test program. *Annual Forum Proceedings - American Helicopter Society*, **2**, 1892–1909.

Heil, P., 2014: ASPeCt ship-based observations during the SIPEX II voyage of the Aurora Australis, 2012.

Heil, P., and Allison, I., 1999: The pattern of Antarctic sea-ice drift in the Indian Ocean and western Pacific sectors. *Journal of Geophysical Research*, **104(C7)**, 15789–15802.

Heil, P., Allison, I., and Lytle, V. I., 1996: Seasonal and interannual variations of the oceanic heat flux under a landfast Antarctic sea ice cover. *Journal of Geophysical Research*, **101(Cll)**, 25,741–25,752.

Heil, P., Massom, R., Stevens, R., Steer, A., and Hutchings, J., 2014: Ice-physics transect data obtained during the SIPEX II voyage of the Aurora Australis, 2012.

Herman, A., 2013: Shear-jamming in two-dimensional granular materials with power-law grain-size distribution. *Entropy*, **15(11)**, 4802–4821.

Herman, A., 2015: Discrete-Element bonded particle Sea Ice model DESIgn, version 1.3 model description and implementation. *Geoscientific Model Development Discussions*, **8(7)**, 5481–5533.

Hodgson, M. E., and Bresnahan, P., 2004: Accuracy of Airborne Lidar-Derived Elevation : Empirical Assessment and Error Budget. *Photogrammetric engineering and remote sensing*, **70(3)**, 331–339.

Hutchings, J. K., Heil, P., Lecomte, O., Stevens, R., Steer, A., and Lieser, J. L., 2015: Comparing methods of measuring sea-ice density in the East Antarctic. *Annals of Glaciology*, **56(69)**, 77–82.

Hutchings, J. K., Heil, P., Steer, A., and Iii, W. D. H., 2012: Subsynoptic scale spatial variability of sea ice deformation in the western Weddell Sea during early summer. *Journal of Geophysical Research*, **117(January 2011)**, 1–16.

Hvidegaard, S. M., and Forsberg, R., 2002: Sea-ice thickness from airborne laser altimetry over the Arctic Ocean north of Greenland. *Geophysical Research Letters*, **29(20)**, 1952.

Immerzeel, W. W., Kraaijenbrink, P. D. A., Shea, J. M., Shrestha, A. B., Pellicciotti, F., Bierkens, M. F. P., and Jong, S. M. D., 2014: High-resolution monitoring of Himalayan glacier dynamics using unmanned aerial vehicles. *Remote Sensing of Environment*, **150**, 93–103.

Jeffries, M. O., Morris, K., Maksym, T., and Kozlenko, N., 2001: Autumn sea ice thickness , ridging and heat flux variability in. *Journal of Geophysical Research*, **106**, 4437–4448.

Kalman, R. E., 1960: A New Approach to Linear Filtering and Prediction Problems 1. *Transactions of the ASME - Journal of Basic Engineering*, **82(Series D)**, 35–45.

Katlein, C., Arndt, S., Nicolaus, M., Perovich, D. K., Jakuba, M. V., Suman, S., Elliott, S., Whitcomb, L. L., McFarland, C. J., Gerdes, R., Boetius, A., and German, C. R., 2015: Influence of ice thickness and surface properties on light transmission through Arctic sea ice. *Journal of Geophysical Research: Oceans*, **120(9)**, 5932–5944.

Katlein, C., Nicolaus, M., and Petrich, C., 2014: The anisotropic scattering coefficient of sea ice. *Journal of Geophysical Research: Oceans*, **119(2)**, 842–855.

Kern, S., Khvorostovsky, K., Skourup, H., Rinne, E., Parsakhoo, Z. S., Djepa, V., Wadhams, P., and Sandven, S., 2015: The impact of snow depth, snow density and ice density on sea ice thickness retrieval from satellite radar altimetry: Results from the ESA-CCI Sea Ice ECV Project Round Robin Exercise. *Cryosphere*, **9(1)**, 37–52.

King, M., 2004: Rigorous GPS data-processing strategies for glaciological applications. *Journal of Glaciology*, **50(171)**, 601–607.

King, M. A., 2009: The GPS contribution to the error budget of surface elevations derived from airborne LIDAR. *IEEE Transactions on Geoscience and Remote Sensing*, **47(3)**, 874–883.

Kool, J., Huang, Z., and Nichol, S. L., 2015: Simulated larval connectivity among Australias southwest submarine canyons. *Marine Ecology Progress Series*, **539**, 77–91.

Kouba, J., and Héroux, P., 2000: Precise Point Positioning Using IGS Orbit and Clock Products. *GPS Solutions*, **5(2)**, 12–28.

Kovacs, A., Weeks, W. F., Ackley, S., and Iii, W. D. H., 1973: Structure of a Multi-Year Pressure Ridge. *Arctic*, 22–31.

Kurtz, N. T., Farrell, S. L., Studinger, M., Galin, N., and Harbeck, J. P., 2012: Sea ice thickness , freeboard , and snow depth products from Operation IceBridge airborne data. *The Cryosphere Discussions*, **6**, 4771–4827.

Kurtz, N. T., Farrell, S. L., Studinger, M., Galin, N., Harbeck, J. P., Lindsay, R., Onana, V. D., Panzer, B., and Sonntag, J. G., 2013: Sea ice thickness, freeboard, and snow depth products from Operation IceBridge airborne data. *The Cryosphere*, **7(4)**, 1035–1056.

Kwok, R., 2010: Satellite remote sensing of sea-ice thickness and kinematics: A review. *Journal of Glaciology*, **56(200)**, 1129–1140.

Kwok, R., and Cunningham, G. F., 2008: ICESat over Arctic sea ice : Estimation of snow depth and ice thickness. *Journal of Geophysical Research*, **113**, 1–17.

Kwok, R., Cunningham, G. F., Zwally, H. J., and Yi, D., 2007: Ice, Cloud, and land Elevation Satellite (ICESat) over Arctic sea ice: Retrieval of freeboard. *Journal of Geophysical Research: Oceans*, **112(12)**, 1–19.

Kwok, R., and Maksym, T., 2014: Snow depth of the Weddell and Bellingshausen sea ice covers from IceBridge surveys in 2010 and 2011: An examination. *Journal of Geophysical Research: Oceans*, 4638–4652.

Lachapelle, G., Sun, H., Cannon, M. E., and Lu, G., 1994: Precise Aircraft-to-Aircraft Positioning Using a Multiple Receiver Configuration. *National Technical Meeting, Institute of Navigation*, no. January, 24–26.

Laxon, S., Peacock, N., and Smith, D., 2003: High interannual variability of sea ice thickness in the Arctic region. *Nature*, 947–950.

Laxon, S. W., Giles, K. a., Ridout, A. L., Wingham, D. J., Willatt, R., Cullen, R., Kwok, R., Schweiger, A., Zhang, J., Haas, C., Hendricks, S., Krishfield, R., Kurtz, N., Farrell, S., and Davidson, M., 2013: CryoSat-2 estimates of Arctic sea ice thickness and volume. *Geophysical Research Letters*, **40(4)**, 732–737.

Lepparanta, M., Lensu, M., Kosloff, P., and Vietch, B., 1995: The life story of a first-year sea ice ridge. *Cold Regions Science and Technology*, **23**, 279–290.

Lichti, D., and Gordon, S., 2004: Error propagation in directly georeferenced terrestrial laser scanner point clouds for cultural heritage recording. *Proc. of FIG Working Week, Athens, Greece, May*, 1–16.

Lieser, J., Newbery, K., Jansen, P. W., Steer, A., Whiteside, S., Meiners, K., and Massom, R., 2014: RAPPLS Surveys (Radar, Aerial Photography, Pyrometer, and Laser Scanning system) made during the SIPEX II voyage of the Aurora Australis, 2012.

Lieser, J. L., 2008: Laser Scanning with AAD's LaDAR system by. Tech. Rep. August, Antarctic Climate and Ecosystes CRC.

Lieser, J. L., Jansen, P. W., Steer, A. D., Heil, P., Massom, R. A., and Williams, G. D., 2013: First results from a CryoSat-2 calibration experiment in the East Antarctic sea ice zone, SIPEX-2. *CryoSat-2 Third User Workshop*, 1–4.

Lytle, V. I., Worby, A. P., and Massom, R. A., 1998: Sea ice pressure ridges in East Antarctica. *Journal of Geophysical Research*, **27(August 1995)**, 449–454.

Markus, T., Massom, R., Worby, A., Lytle, V., Kurtz, N., and Maksym, T., 2011: Freeboard, snow depth and sea-ice roughness in East Antarctica from in situ and multiple satellite data. *Annals of Glaciology*, **52(57)**, 242–248.

Martin, T., Tsamados, M., Schroeder, D., and Feltham, D. L., 2016: The impact of variable sea ice roughness on changes in Arctic Ocean surface stress : A model study. *Journal of Geophysical Research: Oceans*, **121**, 1931–1952.

Massom, R. A., Harris, P. T., Michael, K. J., and Potter, M. J., 1998: The distribution and formative processes of latent-heat polynyas in East Antarctica. *Annals of Glaciology*, **27**, 420–426.

Massom, R. a., and Stammerjohn, S. E., 2010: Antarctic sea ice change and variability - Physical and ecological implications. *Polar Science*, **4(2)**, 149–186.

Massom, R. a., Worby, A., Lytle, V., Markus, T., Allison, I., Scambos, T., Enomoto, H., Tateyama, K., Haran, T., Comiso, J. C., Pfaffling, A., Tamura, T., Muto, A., Kanagaratnam, P., Giles, B., Young, N., Hyland, G., and Key, E., 2006: ARISE (Antarctic Remote Ice Sensing Experiment) in the East 2003: Validation of satellite-derived sea-ice data products. *Annals of Glaciology*, **44**, 288–296.

McPhee, M. G., 2002: Turbulent stress at the ice/ocean interface and bottom surface hydraulic roughness during the SHEBA drift. *Journal of Geophysical Research*, **107(C10)**, 1–15.

Meade, C., Lempert, R. J., Timson, F., and Kadtke, J., 2001: Assessing the Benefits and Costs of a Science Submarine. Tech. rep., RAND Science and Technology Policy Institute.

Meiners, K. M., Vancoppenolle, M., Thanassekos, S., Dieckmann, G. S., Thomas, D. N., Tison, J. L., Arrigo, K. R., Garrison, D. L., McMinn, a., Lannuzel, D., Van Der Merwe, P., Swadling, K. M., Smith, W. O., Melnikov, I., and Raymond, B., 2012: Chlorophyll a in Antarctic sea ice from historical ice core data. *Geophysical Research Letters*, **39(21)**, 1–5.

Morin, K. W. K., 2002: Calibration of Airborne Laser Scanners. *University of Calgary, Calgary, Canada*, **(20179)**, 134.

Morrissy, 2009: Results of vibration measurements 2008. Tech. Rep. 1.

Mostafa, M., Hutton, J. O. E., Reid, B., and Hill, R., 2001: GPS / IMU products the Applanix approach. *Photogrammetric Week '01*.

Mostafa, M. M. R., 2005: Precise Airborne GPS Positioning Alternatives for the Aerial Mapping Practice. *From Pharaohs to Geoinformatics: FIG Working Week 2005*, 1–9.

Nicol, S., Worby, A., and Leaper, R., 2008: Changes in the Antarctic sea ice ecosystem: Potential effects on krill and baleen whales. *Marine and Freshwater Research*, **59(5)**, 361–382.

Nolan, M., 2014: FODAR Measurements of the Cryosphere.

Nolan, M., Larsen, C., and Sturm, M., 2015: Mapping snow depth from manned aircraft on landscape scales at centimeter resolution using structure-from-motion photogrammetry. *The Cryosphere*, **9**, 1445–1463.

Novatel, 2005: Static Baseline Accuracies as a Function of Baseline Length , Observation Time and the Effect of using the Precise Ephemeris.

Ohshima, K. I., Fukamachi, Y., Williams, G. D., Nihashi, S., Roquet, F., Kitade, Y., Tamura, T., Hirano, D., Herraiz-Borreguero, L., Field, I., Hindell, M., Aoki, S., and Wakatsuchi, M., 2013: Antarctic Bottom Water production by intense sea-ice formation in the Cape Darnley polynya. *Nature Geoscience*, **6(3)**, 235–240.

Onana, V. D. P., Kurtz, N. T., Farrell, S. L., Koenig, L. S., Studinger, M., and Harbeck, J. P., 2013: A Sea-Ice Lead Detection Algorithm for Use With High-Resolution Airborne Visible Imagery. *IEEE Transactions on Geoscience and Remote Sensing*, **51(1)**, 38–56.

OXTS, 2008: RT Inertial and GPS measurement Systems User Manual. Tech. rep.

OXTS, 2011: RT Post-process User Manual. Tech. rep.

Ozsoy-Cicek, B., Ackley, S., Xie, H., Yi, D., and Zwally, J., 2013: Sea ice thickness retrieval algorithms based on in situ surface elevation and thickness values for application to altimetry. *Journal of Geophysical Research: Oceans*, **118(8)**, 3807–3822.

Ozsoy-Cicek, B., Kern, S., Ackley, S. F., Xie, H., and Tekeli, A. E., 2011: Intercomparisons of Antarctic sea ice types from visual ship, RADARSAT-1 SAR, Envisat ASAR, QuikSCAT, and AMSR-E satellite observations in the Bellingshausen Sea. *Deep-Sea Research Part II: Topical Studies in Oceanography*, **58(9-10)**, 1092–1111.

Petty, A. A., Tsamados, M. C., Kurtz, N. T., Farrell, S. L., Newman, T., Harbeck, J. P., Feltham, D. L., and Richter-Menge, J. A., 2015: Characterizing Arctic sea ice topography using high-resolution IceBridge data. *The Cryosphere Discussions*, **9(6)**, 6495–6543.

Price, D., Rack, W., Langhorne, P. J., Haas, C., Leonard, G., and Barnsdale, K., 2014: The sub-ice platelet layer and its influence on freeboard to thickness conversion of Antarctic sea ice. *Cryosphere*, **8(3)**, 1031–1039.

Reid, P., Stammerjohn, S., Massom, R., Scambos, T., and Lieser, J., 2015: The record 2013 Southern Hemisphere sea-ice extent maximum. *Annals of Glaciology*, **56(69)**, 99–106.

Ricker, R., Hendricks, S., and Beckers, J. F., 2016: The Impact of Geophysical Corrections on Sea-Ice Freeboard Retrieved from Satellite Altimetry. *Remote Sensing*, **8**.

Rinne, E., and Similä, M., 2016: Utilisation of CryoSat-2 SAR altimeter in operational ice charting. *The Cryosphere*, **10(1)**, 121–131.

Rost, H., and Grierson, H., 2008: High Precision Projects using LiDAR and Digital Imagery. *FIG working week 2008*, no. June 2008, 1–11.

Schaer, P., Skaloud, J., Landtwing, S., and Legat, K., 2007: Accuracy estimation for laser point cloud including scanning geometry. *Mobile Mapping Symposium 2007, Padova*.

Shrestha, R., Carter, W., Slatton, C., and Dietrich, W., 2007: Research-Quality Airborne Laser Swath Mapping : The Defining Factors. Tech. Rep. 510.

Skaloud, B. J., 2002: Direct Georeferencing Direct Georeferencing in Aerial Photogrammetric Mapping What is (not) Solved by the. *Photogrammetric Engineering & Remote Sensing*, **(March)**, 207–209.

Skaloud, J., 2007: Reliability of Direct Georeferencing - Beyond the Achilles' Heel of Modern Airborne Mapping. *Photogrammetric Week '07*, 227–241.

Skaloud, J., Schaer, P., Stebler, Y., and Tomé, P., 2010a: Real-time registration of airborne laser data with sub-decimeter accuracy. *ISPRS Journal of Photogrammetry and Remote Sensing*, **(1)**, 1–5.

Skaloud, J., Schaer, P., Stebler, Y., and Tomé, P., 2010b: Real-time registration of airborne laser data with sub-decimeter accuracy. *ISPRS Journal of Photogrammetry and Remote Sensing*, **65(2)**, 208–217.

Skyllingstad, E. D., Paulson, C. A., and Pegau, W. S., 2003: Effects of keels on ice bottom turbulence exchange. *Journal of Geophysical Research*, **108(C12)**, 1–16.

Slatton, K. C., Carter, W. E., Shrestha, R. L., and Dietrich, W., 2007: Airborne Laser Swath Mapping : Achieving the resolution and accuracy required for geosurficial research. *Geophysical Research Letters*, **34**, 1–5.

Smetacek, V., and Nicol, S., 2005: Polar ocean ecosystems in a changing world. *Nature*, **437**, 362.

Snavely, N., Seitz, S. M., and Szeliski, R., 2006: Photo Tourism : Exploring Photo Collections in 3D. *ACM Transactions on Graphics*.

Spreen, G., Kern, S., Stammer, D., Forsberg, R., and Haarpaintner, J., 2006: Satellite-based estimates of sea-ice volume flux through Fram Strait. *Annals of Glaciology*, **44**, 321–328.

Squire, V. A., Dugan, J. P., Wadhams, P., Rottier, P. J., and Liu, A. K., 1995: Of ocean waves and sea ice. *Annual Review of Fluid Mechanics*, **27(1)**, 115–168.

Stebler, Y., 2008: *GPS/INS Integrity in Airborne Mapping*. thesis, Ecole Polytechnique Federale de Lausanne, 100 pp.

Steer, A., 2013: Calibration report for APPLS 2010. Tech. rep., Australian Antarctic Division, Hobart.

Steer, A., 2014: Calibration report for APPLS 2012. Tech. Rep. March, Australian Antarctic Division, Hobart.

Steer, A., 2015: RT post-process cookbook. Tech. Rep. July.

Steer, A., Heil, P., Hutchings, J. K., Leonard, K., and Maksym, T., 2014: Ice floe surveying conducted during the SIPEX II voyage of the Aurora Australis, 2012.

Steer, A., Newbery, K., and Lieser, J. L., 2012: APPLS LiDAR lab test results. Tech. Rep. 1.

Steer, A., Worby, A., and Heil, P., 2008: Observed changes in sea-ice floe size distribution during early summer in the western Weddell Sea. *Deep-Sea Research Part II: Topical Studies in Oceanography*, **55(8-9)**, 933–942.

Steiner, N., Harder, M., and Lemke, P., 1999: Sea-ice roughness and drag coefficients in a dynamic-thermodynamic sea-ice model for the Arctic. *Tellus, Series A: Dynamic Meteorology and Oceanography*, **51(5)**, 964–978.

Stroeve, J. C., Markus, T., Maslanik, J. A., Cavalieri, D. J., Gasiewski, A. J., Heinrichs, J. F., Holmgren, J., Perovich, D. K., and Sturm, M., 2006: Impact of surface roughness on AMSR-E sea ice products. *IEEE Transactions on Geoscience and Remote Sensing*, **44(11)**, 3103–3116.

Studinger, M., Koenig, L., Martin, S., and Sonntag, J., 2010: Operation Icebridge: Using Instrumented Aircraft to Bridge the Observational Gap between Icesat and Icesat-2. *2010 Ieee International Geoscience and Remote Sensing Symposium*.

Tamura, T., and Ohshima, K. I., 2008: Mapping of sea ice production in the Arctic coastal polynyas. *Geophysical Research Letters*, **35**.

Timco, G. W., and Burden, R. P., 1997: An analysis of the shapes of sea ice ridges. *Cold Regions Science and Technology*, **25**, 65–77.

Timco, G. W., and Frederking, R. M. W., 1996: A review of sea ice density. *Cold Regions Science and Technology*, **24**.

Toyota, T., Massom, R., Lecomte, O., Nomura, D., Heil, P., Tamura, T., and Fraser, A. D., 2016: On the extraordinary snow on the sea ice off East Antarctica in late winter, 2012. *Deep-Sea Research Part II*, 1–15.

Toyota, T., Massom, R., Tateyama, K., Tamura, T., and Fraser, A., 2011: Properties of snow overlying the sea ice off East Antarctica in late winter, 2007. *Deep-Sea Research Part II: Topical Studies in Oceanography*, **58(9-10)**, 1137–1148.

Turner, D., Lucieer, A., and Watson, C., 2012: An automated technique for generating georectified mosaics from ultra-high resolution Unmanned Aerial Vehicle (UAV) imagery, based on Structure from Motion (SFM) point clouds. *Remote Sensing*, **4(5)**, 1392–1410.

Vander Jagt, B., Lucieer, A., Wallace, L., Turner, D., and Durand, M., 2015: Snow Depth Retrieval with UAS Using Photogrammetric Techniques. *Geosciences*, **5**, 264–285.

Wadhams, P., Tucker III, W. B., Krabill, W. B., Swift, R. N., Comiso, J. C., and Davis, N. R., 1992: Relationship between sea ice freeboard and draft in the Arctic Basin, and implications for ice thickness monitoring. *Journal of Geophysical Research*, **97(C12)**, 20325–20334.

Wallace, L., Lucieer, A., Turner, D., and Watson, C., 2011: Error assessment and mitigation for hyper-temporal UAV-borne LiDAR surveys of forest inventory . *SilviLaser*, **(2010)**, 1 – 9.

Wang, X., Xie, H., Ke, Y., Ackley, S. F., and Liu, L., 2013: A method to automatically determine sea level for referencing snow freeboards and computing sea ice thicknesses from NASA IceBridge airborne LIDAR. *Remote Sensing of Environment*, **131**, 160–172.

Weissling, B. P., Lewis, M. J., and Ackley, S. F., 2011: Sea-ice thickness and mass at Ice Station Belgica, Bellingshausen Sea, Antarctica. *Deep-Sea Research Part II: Topical Studies in Oceanography*, **58(9-10)**, 1112–1124.

Willatt, R. C., Giles, K. A., Laxon, S. W., Stone-Drake, L., and Worby, A. P., 2010: Field investigations of Ku-band radar penetration into snow cover on antarctic sea ice. *IEEE Transactions on Geoscience and Remote Sensing*, **48(1)**, 365–372.

Williams, G., Fraser, A., Lucieer, A., Turner, D., Cougnon, E., Kimball, P., Toyota, T., Maksym, T., Singh, H., Nitsche, F., and Paget, M., 2016: Drones in a Cold Climate. *Eos*, **97**.

Williams, G., Kunz, C., Kimball, P., Frost, R., and Alexander, P., 2014a: 3-D mapping of sea ice draft with an autonomous underwater vehicle.

Williams, G., Maksym, T., Wilkinson, J., Kunz, C., Murphy, C., Kimball, P., and Singh, H., 2014b: Thick and deformed Antarctic sea ice mapped with autonomous underwater vehicles. *Nature Geoscience*, **(November)**, 1–7.

Williams, G., Singh, H., Kunz, C., Kimball, P., and Maksym, T., 2014c: Floe-scale maps of sea ice draft from AUV multibeam on SIPEX-II.

Williams, G. D., Bindoff, N. L., Marsland, S. J., and Rintoul, S. R., 2008: Formation and export of dense shelf water from the Adelie depression, East Antarctica. *Journal of Geophysical Research: Oceans*, **113(4)**, 1–12.

Williams, G. D., Maksym, T., Kunz, C., Kimball, P., Singh, H., Wilkinson, J., Lachlan-Cope, T., Trujillo, E., Steer, A., Massom, R., Meiners, K., Heil, P., Lieser, J., Leonard, K., and Murphy, C., 2013: Beyond Point Measurements: Sea Ice Floes Characterized in 3-D. *Eos*, **91(38)**, 333–334.

Wolf, P., 1983: *Elements of Photogrammetry*. McGraw Hill, New York, 2nd edn.

Worby, A. P., and Allison, I., 1991: Ocean-atmosphere energy exchange over thin , variable concentration Antarctic pack ice. *Annals of Glaciology*, **15**, 184–190.

Worby, A. P., Geiger, C. A., Paget, M. J., Woert, M. L. V., Ackley, S. F., and Deliberty, T. L., 2008a: Thickness distribution of Antarctic sea ice. *Journal of Geophysical Research*, **113**, 1–14.

Worby, A. P., Markus, T., Steer, A. D., Lytle, V. I., and Massom, R. a., 2008b: Evaluation of AMSR-E snow depth product over East Antarctic sea ice using in situ measurements and aerial photography. *Journal of Geophysical Research*, **113(C5)**, C05S94.

Worby, A. P., Meiners, K. M., and Ackley, S. F., 2011: Antarctic sea-ice zone research during the International Polar Year, 2007-2009. *Deep-Sea Research Part II: Topical Studies in Oceanography*, **58(9-10)**, 993–998.

Xie, H., Ackley, S. F., Yi, D., Zwally, H. J., Wagner, P., Weissling, B., Lewis, M., and Ye, K., 2011: Sea-ice thickness distribution of the Bellingshausen Sea from surface measurements and ICESat altimetry. *Deep-Sea Research Part II: Topical Studies in Oceanography*, **58(9-10)**, 1039–1051.

Xie, H., Tekeli, A. E., Ackley, S. F., Yi, D., and Zwally, H. J., 2013: Sea ice thickness estimations from ICESat Altimetry over the Bellingshausen and Amundsen Seas, 2003-2009. *Journal of Geophysical Research: Oceans*, **118(5)**, 2438–2453.

Yang, C., Westbrook, J., Suh, C., Martin, D., Hoffmann, W., Lan, Y., Fritz, B., and Goolsby, J., 2014: An Airborne Multispectral Imaging System Based on Two Consumer-Grade Cameras for Agricultural Remote Sensing. *Remote Sensing*, **6(6)**, 5257–5278.

Yi, D., Zwally, H. J., and Robbins, J. W., 2011: ICESat observations of seasonal and interannual variations of sea-ice freeboard and estimated thickness in the Weddell Sea , Antarctica (2003 2009). *Annals of Glaciology*, **52(February 2003)**, 43–51.

Yi, Y., 2007: *On improving the accuracy and reliability of GPS/INS-based direct sensor georeferencing*. Ph.D. thesis, 258 pp.

Zwally, H. J., Comiso, J. C., Parkinson, C. L., Cavalieri, D. J., and Gloersen, P., 2002: Variability of Antarctic sea ice 1979-1998. *J. Geophys. Res.*, **107(C5)**, 3041–.

Zwally, H. J., Yi, D., Kwok, R., and Zhao, Y., 2008: ICESat measurements of sea ice freeboard and estimates of sea ice thickness in the Weddell Sea. *Journal of Geophysical Research*, **113(C2)**, C02S15.